Transport and Gas Sensing Properties of One Dimensional Metal Oxide Nanostructures and Graphene Oxide Based Composites

THESIS

Submitted in partial fulfillment

of the requirements for the degree of

DOCTOR OF PHILOSOPHY

by

A .Venkatesan

Under the Supervision of

Dr. E. S. Kannan

BIRLA INSTITUTE OF TECHNOLOGY & SCIENCE, PILANI

2017

BIRLA INSTITUTE OF TECHNOLOGY & SCIENCE, PILANI

CERTIFICATE

This is to certify that the thesis entitled "**Transport and Gas Sensing Properties of One Dimensional Metal Oxide Nanostructures and Graphene Oxide Based Composites**" is submitted by **A. Venkatesan** ID No. **2011PHXF009G** for the award of Ph.D of the institute embodies original work done by him under my supervision.

Signature of the Supervisor:

Name in capital block letters: **Dr. E. S. Kannan**

Designation: Assistant Professor

Date:

DECLARATION

I **A. Venkatesan** hereby declare that this thesis entitled "**Transport and Gas Sensing Properties of One Dimensional Metal Oxide Nanostructures and Graphene Oxide Based Composites**" submitted by me under the supervision of **Dr. E. S. Kannan** is a bonafide research work. I also declare that it has not been submitted previously in part or in full to this University or any other University or Institution for the award of any degree.

Signature of the Student:

Name: A Venkatesan

Reg. No.: 2011PHXF009G

Date:

DEDICATED TO MY PARENTS

Mr. S. Annadurai & Mrs. Jaya Annadurai

ACKNOWLEDGEMENTS

My special thanks are to Prof. Suresh Ramaswamy (Late) for his encouragement and support.

I would like to extend my special thanks to Birla Institute of Technology and Science for its financial support throughout my research work. Financial support (SR/FTP/PS-138/2012) from Science and Engineering Research Board (A Statutory Body under Department of Science and Technology), Government of India is also greatly acknowledged.

I owe my deepest thanks to Dr. Arun Karthik. He was more than a friend and someone who is there with me to share all of my ups and downs both personally and professionally. It was my pleasure to work with him during the past five years at BITS. Special thanks are due to Mrs. Jyothi Arunkarthick for her nice food, kind and sisterly words in difficult times.

I would like to express my special gratitude to our former group member Ms. Aswini Ramaswamy. It was my pleasure to work with her, who gave suggestions and extended support to my work without any reservation. I would also like to extend my special thanks to my junior Ms. Anu Roshini for her support.

A lot of gratitude should go to my M.Phill supervisor Dr. Mohan Kumar, Presidency College, Chennai for his continuous encouragement to take up research as my carrier without whom I might not be here today.

I would also like to thank Mr. J. Selvaganapathy and Mr. M. M. Bijeesh and other research scholars for being with me and sharing wonderful time all these years.

Finally, the most importantly, I thank my parents Mr. Annadurai and Mrs. Jaya Annadurai for their unconditional love, encouragement, support, understanding and their untold sacrifices. My gratitude also goes to my other family members Soban Babu, Gunasekaran, Kalaivani Gunasekaran, Rohith, and Harini for their unwavering support and love along the journey.

A. Venkatesan.

TABLE OF CONTENTS

LIST OF FIGURES

LIST OF TABLES

LIST OF SYMBOLS AND ABBREVIATIONS

1D	-	One Dimensional
SEM	-	Scanning Electron Microscope
TEM	-	Transmission Electron Microscope
AFM	-	Atomic Force Microscope
2D	-	Two Dimensional
0D	-	Zero Dimensional
1DEG	-	1D Electron Gas
2 DEG	-	2D Electron Gas
3 DEG	-	3D Electron Gas
ZnO	-	Zinc Oxide
NRs	-	Nanorods
Au	-	Gold
Pt	-	Platinum
DI	-	Deionised Water
ITO	-	Indium Tin Oxide
PMMA	-	Polymethyl Methacrylate
HMTA	-	Hexamethylenetetramine
LDA	-	Local Density Approximation
SIC-PP	-	Self Interaction Corrected Pseudo Potential
Cu_2O	-	Cuprous Oxide
MSM	-	Metal-Semiconductor-Metal
TFE	-	Thermionic and Field Emission Theory
TMDC	-	Transition Metal Dichalcogenides
MoS_2	-	Molybdenum Disulfide
VBM	-	Valence Band Maximum
GGA	-	Generalized Gradient Approximation
HFA	-	Hartree Fock Approximation
SnO_2	-	Tin Oxide
CVD	-	Chemical Vapor Deposition
AM1	-	Air Mass 1

VLS	-	Vapor-Liquid-Solid
AAO	-	Anodized Aluminum Oxide
CE	-	Counter Electrode
WE	-	Working Electrode
RE	-	Reference Electrode
NHE	-	Normal Hydrogen Electrode
SCE	-	Saturated Calomel Electrode
GO	-	Graphene Oxide
RGO	-	Reduced Graphene Oxide
NFs	-	Nano Flowers
XPS	-	X-Ray Photoelectron Spectroscopy
DOS	-	Density Of States
XRD	-	X-ray Diffraction
LSV	-	Linear Sweep Voltammetry
l_m	-	Mean Free Path
v_F	-	Fermi Velocity
τ_m	-	Momentum Relaxation Time
l_ϕ	-	Phase Relaxation Length
τ_ϕ	-	Phase Relaxation Time
D	-	Diffusion Constant
l_s	-	Sample Length
k_B	-	Boltzman Constant
T	-	Temperature
P	-	Pressure
d	-	Wire Diameter
eV	-	Electronvolt
meV	-	Milli Electronvolt
sq	-	Square
K	-	Kelvin
^{o}C	-	Degree Celcius
g	-	Gram

W	-	Watt
cm	-	Centimeter
s	-	Second
V	-	Volt
mol	-	Mole
Å	-	Angstrom
J	-	Joule
Ω	-	Ohm
C_p	-	Specific heat capacity
k	-	Thermal conductivity
α	-	Thermal diffusivity
I	-	Current
A	-	Area
ϕ_m	-	Metal Work Function
ϕ_S	-	Semiconductor Work Function
χ	-	Electro Affinity
V_{bi}	-	Built-in Potential
ϕ_B	-	Schottky Barrier
ρ	-	Density
t	-	Time
E	-	Equivalent Weight
F	-	Faraday Constant
z	-	Unitless Valence of the Deposited Atoms
A^*	-	Effective Mass of the Electron

ABSTRACT

One dimensional (1D) metal oxides nanostructures are considered to be a promising material for solar cells, biosensors, electrochemical detection, and photocathode applications, as they are economically cheaper and highly suitable for large scale production. Therefore it is imperative to study these nanostructures in detail so that a cost effective technology for various field effect and sensing application using metal oxides can be realized. This thesis is an attempt to contribute in the direction of establishing a highly reliable technique for synthesizing 1D metal oxide nanostructures and reduced graphene oxide based composites and study their electrical transport characteristics as well as gas sensing properties.

First, the effect of reduced graphene oxide (RGO) thin film on the transport characteristics of vertically aligned zinc oxide nanorods (ZnO NRs) grown on ITO substrate were studied. We showed that GO uniformly drop casted on ZnO NRs can be easily converted to RGO at 60^0C. Thermally excited electrons from Zn_i interstitial sites (~30 meV) of ZnO nanorods aided this low temperature reduction. From the current-voltage (I-V) measurements of RGO–ZnO NRs, we demonstrated that the RGO layer not only acts as a short circuiting inhibitor but also reduces the height of the potential barrier for electron tunneling. We further probed the presence of trap and defect states in ZnO nanorods by carrying out temperature dependent I-V characteristics. From the activation energies we found that there are different traps and defect states which are active in different temperature regimes. From the results we have concluded that Zn interstitial states can be a possible source of inherent n-type conductivity of ZnO.

The other important metal oxide we focused in this thesis was copper oxide (Cu_2O). Growth of free standing Cu_2O nanopillars (on gold substrate) were carried out by template (AAO) assisted electrodeposition technique. We optimized the experimental procedure for the removal of AAO template to obtain free standing Cu_2O nanopillars by conducting various experimental trials. The room and low temperature current-voltage (I-V) measurement of Cu_2O nanopillars were carried out in two terminal (Au-Cu_2O-Au) configurations. The transport characteristics of Cu_2O nanopillars were explained by considering thermionic field emission (TFE) theory in back to back schottky (metal-semiconductor-metal) model. Using this model, we derived the carrier concentration as well as activation energies of carrier traps and defect states present in Cu_2O nanopillars.

Low temperature hydrogen (H_2) sensor based on reduced graphene oxide (RGO) and tin oxide nanoflowers (SnO_2 NFs) based composite were fabricated. From the morphological study (FE-SEM), it was observed that the addition of SnO_2 NFs into RGO solution inhibits irreversible restacking and agglomeration of RGO and increases the active surface area for interaction with H_2. This RGO-SnO_2 NFs hybrid film sensor showed an excellent sensing response, response time and recovery time to H_2. We found that the highly improved H_2 sensing characteristics of RGO-SnO_2 NFs hybrid are due to (a) unique structural geometry that increased the surface area for H_2 adsorption, and (b) change in the width of depletion layer at the interface due to H_2 interaction.

Finally we report the hydrogen (H_2) sensors based on reduced graphene oxide (RGO)/Molybdenum disulfide (MoS_2) nano particles (NPs) based composites fabricated by facile drop casting method. The RGO/MoS_2 composite exhibited highly enhanced sensing response to H_2 at an operating temperature of $60^{o}C$. It was found that our RGO/ MoS_2 composite sample showed excellent selectivity to H_2 compared to ammonia (NH_3) and nitric oxide (NO) gases. The composite's response to H_2 is 2.9 times higher than that of NH_3 whereas for NO it is 3.5. We attribute this highly improved H_2 sensing response and selectivity of RGO/MoS_2 nanocomposites to the structural integration of MoS_2 nanoparticles in the nanochannels and pores present in the RGO.

OUTLINE OF THE THESIS

This thesis work has been split into six chapters. In **chapter 1**, a brief introduction of various topics, essential for the understanding of the main subjects of this research work, has been given. The topics discussed are basic aspects of nanoscience and nanotechnology, classification of nanomaterials into two dimensional (2D), one dimensional (1D) and zero dimensional (0D) system, importance of 1D nanostructures, their growth techniques and basics of electrical and gas sensing mechanism.

Chapter 2 discusses the hydrothermal growth of Zinc Oxide nanorods (ZnO NRs) on conductive Indium Tin Oxide (ITO) substrate. The challenge associated with the formation of electrical contacts on the ZnO NRs is illustrated. A technique involving *in-situ* reduction of graphene oxide on ZnO NRs to improve the reliability of contact for low temperature transport measurements is described.

Chapter 3 gives the detailed experimental procedure for realizing vertically aligned copper oxide (Cu_2O) nanopillars by AAO template assisted electrodeposition technique. A detailed analysis about the recipe for removing AAO template is discussed. A thorough investigation of the effect of etching on the surface morphology of nanopillars and its transport properties are discussed.

Chapter 4 presents the comprehensive information on the synthesis of graphene oxide (GO), tin oxide nanoflowers (SnO_2 NFs) and RGO/SnO_2 NFs composites. Structural and optical properties of the RGO-SnO_2 NFs based nanocomposites are discussed. The hydrogen sensing response of this composite is studied to explore the possibility of fabricating highly efficient room temperature H_2 gas sensor.

Chapter 5 discusses the synthesis of GO, molybdenum disulphide (MoS_2) and their composite (RGO/MoS_2). The structural, morphological and optical characterization of RGO/MoS_2 nanocomposites along with the H_2 sensing characteristics is provided.

Chapter 6 gives the conclusion and summary of this research work along with the possibility of future work in the same direction**.**

CHAPTER ONE

INTRODUCTION

In this chapter, the motivation and fundamental aspects of the research work presented in this thesis is given. To introduce the main subjects that will be presented and discussed in the rest of the thesis, the current chapter has been divided into four sections. The first section introduces some important aspects of nanoscience and nanotechnology, classification of nanomaterials, and importance of one dimensional (1D) metal oxide (ZnO, Cu_2O, and SnO_2) nanostructures. The second section describes the growth techniques involved in 1D nanostructure especially hydrothermal and electrodeposition technique. The third section discusses the theoretical aspects of metal-semiconductors junction which are important for understanding the electrical transport properties of 1D nanostructures and hydrogen sensing characteristics of metal oxide/graphene oxide composites. The last section provides brief information on tools used for the characterization of 1D metal oxide nanostructures along with the outline on the work to be presented in the following chapters.

1.1. BASIC ASPECTS OF NANOMATERIALS

In the last few decades, nanomaterials have been the focus of research to study new physics and investigate its potential to develop technologies for practical applications [1, 2]. Dimensionally, nanomaterials have at least one of its length scales in the order of few nanometers (~ 100 nm). At this small dimension, the number of atoms available at the surface is high, making the properties of nanostructures different from those of their bulk counterpart, despite the fact that they share the same chemical compositions [3-5]. Nanomaterials usually have (1) large fraction of surface atoms (2) high surface energy (3) quantized energy states and (4) reduced defects. The high surface to volume ratio coupled with quantum confinement of electrons and many body interaction leads to novel mechanical, electrical, optical, chemical, and biological applications [6-8].

In 1959, Richard Feynman in his famous talk titled "there's a plenty of room at the bottom" has invoked the idea of manipulating things at atomic level [9]. However, the real burst of nanotechnology occurred in the early 1990s, after the development of sophisticated

instruments such as scanning electron microscope (SEM), transmission electron microscope (TEM) and atomic force microscope (AFM) for characterization which enabled investigation of nanomaterials at the atomic level feasible [10-12]. These tools were then used to manipulate materials at nanoscale to achieve new physical properties such as variable band gap, enhanced phonon and electron conductivity, high tensile strength and tunable optical characteristics.
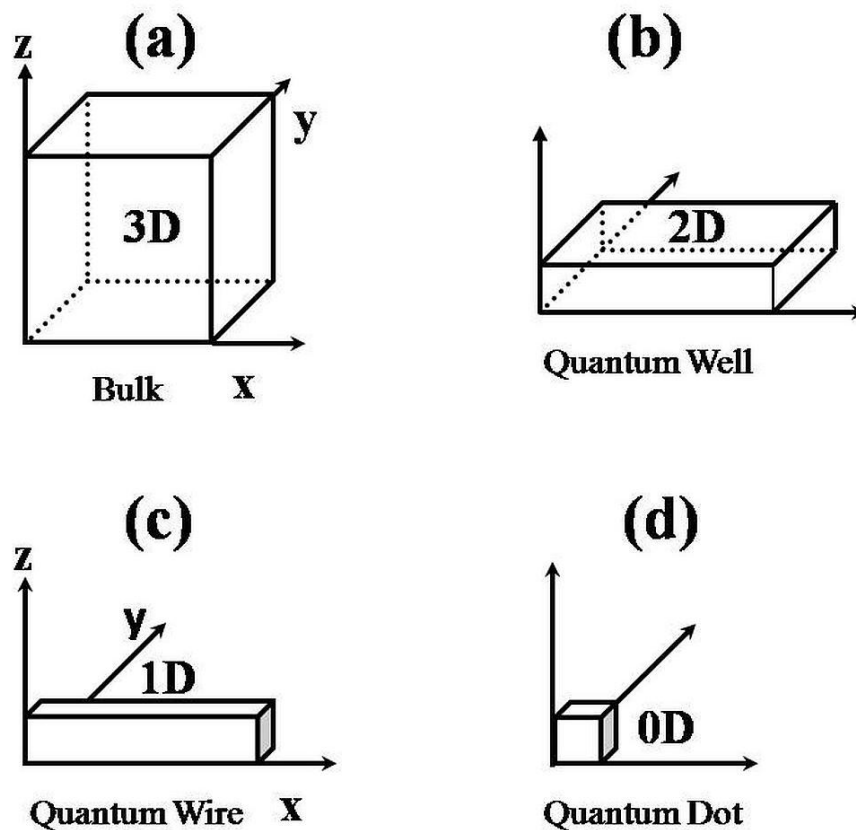
Figure 1.1: Schematic representation of quantum confinement in bulk, 2D, 1D and 0D nanomaterials.

Nanostructures can be classified into two dimensional (2D, nanofilm), one-dimensional (1D, nanorods or nanowires), and zero dimensional (0D, quantum dots or nanoparticles) nanomaterials depending upon the degree of freedom available for the electron (Figure 1.1a-1.1d) [8]. For instance in 2D materials electrons are constrained to move freely in plane and the

motion perpendicular to the plane is restricted to length scale less than 100 nm. Similarly in 1D materials, electrons are free to move in one direction and movement in other two directions are restricted. For 0D materials, electrons are confined in all three directions. The properties of these nanomaterials vary significantly from those of bulk counterpart [13-18]. For example, thin films of metals are chemically inert whereas, metallic nanoparticles are chemically very active and sensor made up of these materials was found to have highly enhanced sensitivity and selectivity [18-21].

1.1.1. Why 1D Nanomaterials?

In this thesis, we chose to work on 1D nanomaterials as they are easily scalable in comparison to 2D and 0D materials. 1D nanomaterials can be easily grown to large lengths of the order of millimeters while maintaining high crystalline order. Such large lengths are difficult to achieve in 2D materials. Highly crystalline graphene for instance are restricted to a flake size of few microns. 0D materials are practically very difficult to implement for any real time applications. The millimeter length scale allows the 1D nanostructures to contact the macroscopic world for many physical measurements which makes them an attractive structure of choice for fabricating nanoscale devices [22, 23].

Among the 1D nanomaterials, particularly, metal oxide based 1D semiconductors are one of the most sort after materials as they exhibit either hole type or electron type conductivity without any external doping. So in the metal oxide 1D nanorods, it is possible to have high mobility electrons or holes as the scattering due to impurities (dopants) are absent. It is also possible to fabricate p-n junction by growing heterostructures of two metal oxides which intrinsically exhibit electron and hole conductivity. Moreover, metal oxide nanomaterials can also be synthesized easily in different shapes such as nanorods, nanowires, nanotubes, and nanobelts. These different geometries can be exploited for various applications such as drug delivery, chemical and bio sensing, solar cells and field emission devices. Also these structures have different band gap which can be tuned by controlling their size [24-28].

1.1.2. Band Gap Engineering

In free space, electrons can have all possible energy states and hence their energy and momentum (E-k) relation is parabolic and continuous. Inside a solid, electrons move in the

periodic potential of the lattice and the interaction of electron wave function with the periodic potential gives rise to an energy gap whose value strongly depends on the atomic arrangement in the solid. It is possible to tailor the band gap according to our requirement by manipulating the size and shape of the solid. Band gap is very crucial in classifying solids as conductors, semiconductors and insulators. Band gap in general refers to an electrical band gap which indicates the energy difference between the top of the valence band and bottom of the conduction band. This band gap can be either direct or indirect depending upon the location of valence band maxima and conduction band minima. If they both have same momentum values then the band gap is direct or else it is indirect [29-32]. For most electrical and optical devices, direct band gap semiconductors are preferred as they dissipate less energy to the lattice. The other kind of band gap is the optical band gap. Optical band gap of semiconductor is defined as the energy required for creating an electron and hole and the electron-hole pair so produced are called as exciton. Exciton is a quasi particle comprising of electron and hole bound together by an attractive force. They exist as a single entity and for bulk semiconductor the dimension of the exciton can be theoretically calculated by Bohr radius [33],

$$a_B = \frac{\hbar \varepsilon}{\mu e^2} \tag{1.1}$$

where $\hbar$ is defined as Planck constant, ε is the dielectric constant and μ is the exciton reduced mass. However, if the radius of the semiconductor nanocrystal (quantum dot) is reduced to less than its exciton Bohr radius then the exciton will be strongly confined in this limited volume and the electronic structure of the three dimensionally confined electrons and holes will be drastically modified [34, 35].

1D nanostructures (Quantum wires) represent confinement of electrons or holes in two dimensions. Such confinement permits free electron (or hole) behavior in only one direction that is along the length of the wire (say the x direction). For this reason, the system of quantum wires are described as 1D electron gas (IDEG) when electrons are present in the conduction band [36, 37].

The total energy of an electron or hole in 1D material is the sum of allowed energies associated with the motion of these carriers along two quantized direction (say y, z direction) and

the kinetic energy due to free motion of carriers in the other direction (say *x* direction) [38, 39] is given by,

$$E_{Total} = \frac{\hbar^2}{2m}\left[\frac{n_z \pi}{a}\right]^2 + \frac{\hbar^2}{2m}\left[\frac{n_y \pi}{b}\right]^2 + \frac{\hbar^2}{2m}\left(k_x^{\,2}\right)$$

(1.2)

where n_y, n_z are integers and *a*, *b* are confined sizes of the materials along *z* and *y* directions. From the above formula, it is clear that it is possible to engineer the band gap in 1D material by varying geometry of the structure. The band gap can be increased or decreased by reducing or increasing the size of spatial confinement of electrons i.e. by changing the value of "*a*" and "*b*". One important point to note is that if the size of "*a*" or "*b*" is increased beyond a certain limit, then the crystal enters into a 2D regime, which not only alters the band gap but also the materials density of states. This will lead to a whole new set of physics as illustrated below (figure 1.2a - 1.2d).

1.1.3. Density of States

Density of states refers to the number of available electron states per unit volume in the crystal. When the density of states is multiplied by the energy interval *dE*, it gives the total concentration of available states in that energy range *dE*. Another important feature of the density of states is that it is not uniform across the energy band. In 3D crystals, the density of states is maximum at the top of the band and minimum at the bottom of the band. For 2D crystals, the density of states is constant across the band, whereas in 1D structure, density of state peaks at the band edges and decreases sharply as we move away from the edge. Density of states resembles dirac-delta like function for 0D materials. The importance of density of states can be understood from the fact that any electron excitation from the valence band to the conduction band depends upon the number of available energy states at the band edges. In 3D materials one needs to pump more energy to excite electrons from the valence band to the conduction band, as more energy is required to distribute electron across different energy states. In 1D materials, a comparatively less energy is required to populate the conduction band, as almost all the energy states are located at the band edges. That is why nanomaterials are very good candidates for optoelectronic applications. In bulk semiconductor the density of states is smooth and

continuous and is proportional to ($\frac{dN}{dE} = E^{1/2}$). However for nanomaterials, the density of states is sensitively dependent on the size (along the confined direction) of the nanomaterials. For 0D nanomaterials, the electrons are completely confined in all three dimensions and they behave analogous to atomic/molecular clusters with discrete states that are well separated in energy ($\frac{dN}{dE} = \delta(E)$). In 2D nanomaterials the density of states shows a quasi-continuous like increment with increasing energy due to the quantum confinement in one direction ($\frac{dN}{dE} = Constant$). In 1D nanomaterials, the density of states is quasi discrete with respect to increasing energy due to the confinement along two axis perpendicular to the length of the material ($\frac{dN}{dE} = E^{-1/2}$). Once electrons are populated at the conduction band edge, it motion across the crystal is determined by the transport properties of the material [40, 41].
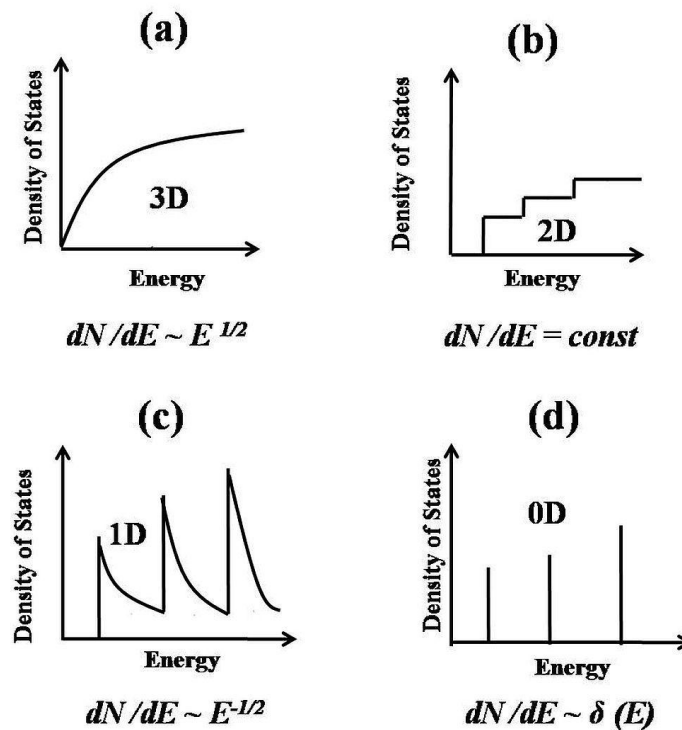
Figure 1.2: Schematic Illustration of Density of states as a function of energy in bulk, 2D, 1D and 0D nanomaterials.

1.2. ELECTRICAL TRANSPORT PROPERTIES

Electron transport refers to the manner in which electrons move across the crystal. The motion can be categorized as diffusive, quasi-ballistic and ballistic depending upon the nature of scattering that electron experiences during its journey. In the presence of strong scatterers such as impurities and defects, the motion is most likely to be diffusive. However for weak scattering such as electron-electron and electron-phonon interaction, the motion can be quasi ballistic or ballistic. To quantify the effect of scattering potentials on the electron motion, parameters such as Fermi wavelength, electron mean free path and phase relaxation length are being used.

To understand the effect of size reduction on various phenomena of one dimensional nanostructures, it is important to have a clear idea about certain characteristic lengths. These characteristic lengths determine the behavior of the systems as the effects start to appear when the size of the system is reduced. In the case of electrical transport in one dimensional nanostructures, there are few characteristic lengths which determine whether the transport is classical or quantum in nature. They are Fermi wavelength and electron mean free path.

1.2.1. Fermi Wavelength (λ_F)

The wavelength associated with the kinetic energy of the electrons is called the de Broglie wavelength. It defines the length scale on which quantum mechanical effects, i.e. the wave-like nature of electron becomes very important. At low temperatures, the current is mainly dominated by the electrons whose energy is very close to the Fermi energy and the contribution by the electrons far below it is negligible. Therefore, the Fermi wavelength is the relevant wavelength. The Fermi wavelength is given by,

$$\lambda_F = \frac{2\pi\hbar}{p} = \frac{2\pi}{k_F} = \sqrt{2\pi/n} \tag{1.3}$$

where k_F is the Fermi wave vector which is proportional to the square root of electron density n for 2 dimensional electron gas (2DEG). For 3 dimensional electron gas (3DEG), the corresponding relation is:

$$\lambda_F = \left(\frac{3n}{8\pi}\right)^{-1/3} \tag{1.4}$$

In general, $k_F \sim (n)^{1/d}$, where d represents the dimension of the system. At 300K, in a typical semiconductor, the de Broglie wavelength is of the order of 75 nm.

1.2.2. Mean Free Path (l_m)

The mean-free path is the average distance that an electron travels before it experiences inelastic scattering which changes its initial momentum. This momentum change is related to the scattering of electrons by static impurities, imperfections such as lattice defects and internal or external surface boundaries. In addition, lattice vibrations (phonons), other electrons present inside the lattice and magnons can also affect the mean free path. The mean free path of a conduction electron is given by,

$$l_m = v_F \tau \tag{1.5}$$

where v_F is the Fermi velocity and τ is the momentum relaxation time (during which the applied electric field acts on the electron).

1.2.3. Phase Relaxation Length (l_ϕ)

The phase relaxation length is defined as the length to which electrons travels before it experience the inelastic scattering which destroys its initial coherent state. Scattering events such as electron-electron collision and electron-phonon collisions changes the energy of the electrons and randomizes its quantum-mechanical phase. Scattering by impurities may also contribute to the phase-relaxation length. The phase relaxation length (l_ϕ) can be expressed as,

$$l_\phi = v_F \tau_\phi \tag{1.6}$$

This is often the case in high mobility semiconductors where phase relaxation time (τ_ϕ) is in the same order or smaller than the momentum relaxation time (τ_m). In low mobility semiconductor $\tau_m < \tau_\phi$, the transport is mostly diffusive. In the diffusive regime, the phase-relaxation time is given in terms of diffusion constant ($D = v_F^2 \tau_m / 2$) as,

$$l_\phi^2 = D\tau_\phi \qquad (1.7)$$

The three parameters described above have a detrimental effect on the electrical properties of the material. It is to be noted that all the three parameters have either direct or indirect dependence on geometric parameters of the materials. Therefore, by varying the geometry of the material, it is possible to engineer the value of mean free path relaxation time and Fermi wavelength. In the following section, we highlight some of the important aspect of electrotransport in 1D nanostructures.

1.2.4. Electrical Transport in 1D Nanostructures

In 1D nanostructures, electron are constrained to move in one direction and ideally their motion in this direction should be ballistic. For example if the characteristics length of the nanorod is around 1 micrometer, then for a ballistic transport, the electron mean free path should be equal to or greater than 1μm. One needs to ensure sufficient crystalline quality to achieve such high mean free paths or else the advantage of scaling down the material size offers no benefit.

In ballistic transport, electrons can travel across the *sample length* without undergoing any scattering inside the sample. Here the *sample length* (l_s) is defined as a length over which the transport property is measured. Ballistic transport occurs when $l_s << l_m$, so that the electron suffers no scattering when voltage is measured between the electrodes. This is the regime of classical Ballistic transport (figure 1.3a).

The Ballistic transport can also be quantum in nature. If the diameter of the wire is comparable to electron wavelength, the electronic energy levels becomes discrete and the electrical transport enters the quantum regime (figure 1.3b). In this regime, the thermal energy of the electron must be less than the energy difference between the discrete levels to suppress any scattering events. In such cases, the conductance is given by Laundauer formula:

$$G = G_0 \sum_{i,j=1}^{N} T_{ij} \ ; G_0 = \frac{2e^2}{h} \qquad (1.8)$$

where e is the electronic charge, h is the Planck's constant and T_{ij} is the transmission probability from i^{th} channel at one end of the wire to the jth mode at the other end. The summation is over all channels having a non-zero value of the transmission probability. In the ideal case with no backscattering at the contacts, $T_{ij} = 1$ for i=j and zero otherwise.

For nanowires with lengths larger than the carrier mean free path, the electrons undergo numerous scattering events while they travel along the wire. In this case, the electrical transport is in the diffusive regime and the conduction mechanism is dominated by the carrier scattering caused by phonons (lattice vibrations), boundary scattering, lattice and other structural defects, and impurity atoms. For wire diameters (d) comparable to or smaller than the carrier mean free path (l_m), i.e., $d < l_m$ or $d \sim l_m$, but still much larger than the Broglie wavelength of the electrons ($d \gg \lambda_F$), the transport in nanowires still falls in the classical regime, where the band structure of the nanowires are still similar to that of bulk, while the scattering events at the wire boundary greatly influence the transport behavior.
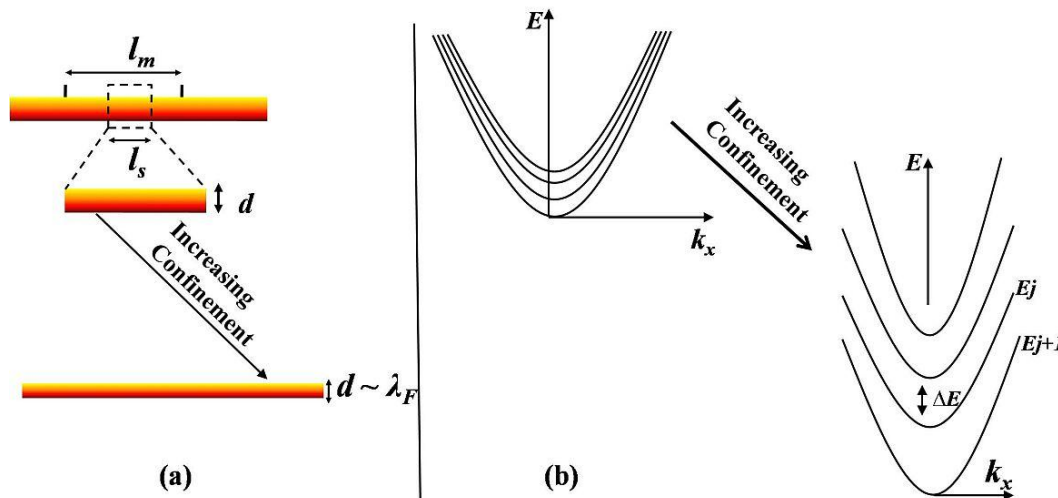
Figure 1.3: (a) Schematic representation of increasing confinement by size reduction. (b) Increasing confinement leads to increase in ΔE, the energy between the 1D subbands (when $\Delta E > k_{BT}$, transport occurs through individual subbands and can be considered as "one dimensional"). Reproduced with slight modification from "PhD thesis: Quantum transport in one-dimensional nanostructures".

The aspect ratio (length to width ratio) of 1D nanostructures determines the electron transport regime. Technologically, it is really challenging to synthesize nanorods arrays with identical electron transport properties. This is due to inhomogenity of the size distribution of nanorods. One can overcome this problem by carrying out transport measurement over a large area of nanorods and the average behavior can be modeled using any one of the transport theories explained earlier to a good approximation. This thesis is an attempt to synthesize and study the electrical transport and sensing characteristics of metal oxide based nanorods.

1.3. ONE DIMENSIONAL (1D) METAL OXIDE NANOSTRUCTURES

Metal oxides are generally represented by M_xO_x where M stands for metals such as Cu, Zn, Sn, Fe, Si, and Ti. Metal oxides are ionic compounds that are made up of positive metallic and negative oxygen ions. The electrostatic interactions between the positive metallic and negative oxygen ions result in firm and solid ionic bonds [42, 43]. The s-shells of metal oxides are completely filled, so that most of the metal oxides have good thermal and chemical stability. However, their d-shells may not be completely filled, giving them a variety of unique properties such wide band gaps, high dielectric constants, reactive electronic transitions, and good electrical, optical, and electrochromic characteristics [44-46]. Metal oxides can be grown by either physical or chemical techniques. Atomic layer deposition, chemical vapour deposition, sputtering, and thermal evaporation are the various physical techniques commonly used to grow metal oxides. Chemical techniques involve mixing of salts of metals with strong oxidizing agents in a chemical bath to produce metal oxides. Regardless of the growth technique employed, metal oxides shows new properties that originate from the more complex electronic properties and crystal structures compared to other class of materials. This unique physical properties are due to the existence of different oxidation states, coordination numbers, symmetry, density, and stoichiometry. When these metal oxides are grown in 1D geometry, they exhibit highly enhanced physical characteristics such as high optical absorption, ballistic conductance, improved magnetic susceptibility, and significantly strong surface plasmon resonance which are primarily useful for bio-sensing applications. Of the many metal oxides, ZnO, Cu_2O and SnO_2 are the materials with a great potential for fabricating gas sensors, field emission devices, solar cells, and field effect transistors. In the following sections, the structural, electrical and optical properties of ZnO, Cu_2O and SnO_2 are discussed [47-50].

1.3.1. Zinc Oxide (ZnO)

Zinc oxide is a group II-VI semiconductor, whose covalence is on the boundary between ionic and covalent semiconductors. Its large energy band gap (3.37 eV), high exciton binding energy (60 meV) and high thermal and mechanical stability at room temperature make it an attractive candidate for use in electronics, optoelectronics and laser technology [51]. Furthermore, it is an electrically transparent conducting oxide semiconductor and exhibits defects or impurity dominated n-type conductivity, even in its native state. The piezoelectric and pyroelectric properties of ZnO mean that it can be used as a sensor, energy generator and photocatalyst in hydrogen production. Because of its hardness, rigidity and piezoelectric properties it is an important material in the ceramics industry, while its low toxicity, biocompatibility and biodegradability make it a material of interest for biomedicine and in pro-ecological systems [52].
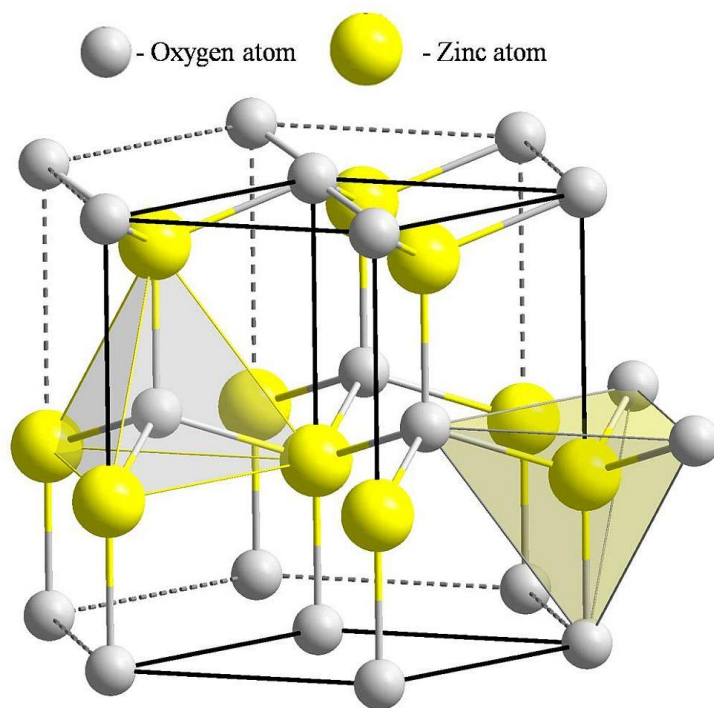
Figure 1.4: The wurtzite crystal structure of Zinc Oxide (ZnO) with Zn-O tetrahedral coordination highlighted. White balls represent oxygen atoms and the yellow ones represent zinc atom.

1.3.2. Crystal Structure of ZnO

ZnO typically occurs in three different crystal structures, wurtzite (hexagonal symmetry), zinc blende (cubic symmetry) and rock salt structure. At room temperature, it crystallizes into more common and stable form of wurtzite structure (figure 1.4) [53]. This hexagonal lattice belongs to P6$_3$*mc* space group with the lattice constant a = 3.2495 Å, which represents the basal plane, and c = 5.2069 Å, which is in the basal direction. The c/a ratio is 1.602, which is close to the 1.633 ratio of an ideal hexagonal closed packed structure [54]. This structure is characterized by two interconnecting sub lattices of Zn^{2+} and O^{2-} such that each Zn ion is surrounded by a tetrahedral O ion, and vice-versa. The two sets of sub lattices are separated by *u*=0.385 in fractional coordinates along the c-axis. The parameter *u* of ZnO crystal is derived from the ideal wurtzite structure (*u*=0.375), and is defined as the amount by which each atom is displaced with respect to the next along the c-axis. ZnO can be simply described as a number of alternating planes each consisted of tetrahedral coordinated O^{2-} and Zn^{2+} ions, stacked alternately along the c-axis and is characterized by two interconnecting sublattices of Zn^{2+} and O^{2-}. The tetrahedral coordination in ZnO leads to a non-central symmetric structure, which is one of the most important characteristics of wurtzite structural materials. The lack of central symmetry in wurtzite structure, combined with large electromechanical coupling, results in strong piezoelectric and pyroelectric properties. The other important structural characteristic of ZnO is the polar surfaces. The most common polar surface is the basal plane [55].

In ZnO, internal charges are created by positively charged Zn - (0001) and negatively charged O - (000$\bar{1}$) surfaces, resulting in the creation of dipole moment and spontaneous polarization along the c-axis as well as a divergence in surface energy. To maintain a stable structure, the polar surfaces generally have facets or exhibit massive surface reconstructions. However, ZnO - ± (0001) are exceptions: they are atomically flat, stable and without reconstruction [56]. The other two most commonly observed facets of ZnO are (11$\bar{2}$0) (a-axis) and (10$\bar{1}$0), which are non-polar surfaces and they have lower energy than the (0001) facets. The polar faces possess different chemical and physical properties, while the O-terminated face possess a slightly different electronic structure to the other three faces. Moreover, the polar surfaces and the (10$\bar{1}$0) surface are found to be stable; whereas, the (11$\bar{2}$0) face is less stable and generally has a higher level of surface roughness. The tetrahedral coordination of this compound

is also a common indicator of sp^3 covalent bonding. However, the Zn-O bond also possesses very strong ionic character, and thus ZnO lies on the borderline between being classified as a covalent or ionic compound, with an iconicity of $f_i = 0.616$ on the Phillips iconicity scale [57].

Table.1.1: Physical Parameters of ZnO

Physical Parameters	Values
Density (ρ)	5.606 g/cm^3
Stable Phase at 300 K	Wurtzite
Melting Point	1975^{0}C
Thermal conductivity (k)	0.6, 1–1.2 Wcm^{-1}K^{-1}
Linear expansion coefficient(/^{o}C)	a$_0$: 6.5 $\times 10^{-6}$ c$_0$: 3.0 $\times 10^{-6}$
Static dielectric constant	8.656
Refractive index	2.008, 2.029
Energy gap	3.37 eV, direct
Intrinsic carrier Concentration	<10^6 cm^{-3} (max n-type doping >10^{20} cm^{-3} electrons; max p-type doping <10^{17} cm^{-3} holes)
Exciton binding energy	60 meV
Electron effective mass	0.24
Electron Hall mobility (at 300 K for low n-type conductivity)	200 cm^2/V s
Hole effective mass	0.59
Hole Hall mobility (at 300 K for low p-type conductivity)	5–50 cm^2/V s

1.3.3. Electronic Structure of ZnO

The electronic band structure of ZnO has been calculated using the Local Density Approximation (LDA) and incorporating atomic self interaction corrected pseudo potentials

(SIC-PP). This theory predicts that the band structure exhibit high symmetry lines in the hexagonal Brillouin zone [60]. Both the valence band maxima and the lowest conduction band minima occur at the Γ point k=0 indicating that ZnO is a direct band gap semiconductor. The band gap of ZnO is 3.4 eV and the temperature dependence of the band gap up to 300 K is given by the following relationship [58-61],

$$E_g\ (T) = E_g\ (T=0)\frac{5.05 \times 10^{-4}T^2}{900-T} \tag{1.9}$$

Table 1.1 lists some of the fascinating electrical, optical and mechanical properties of ZnO [62, 63].

1.3.4. Cuprous Oxide (Cu₂O)
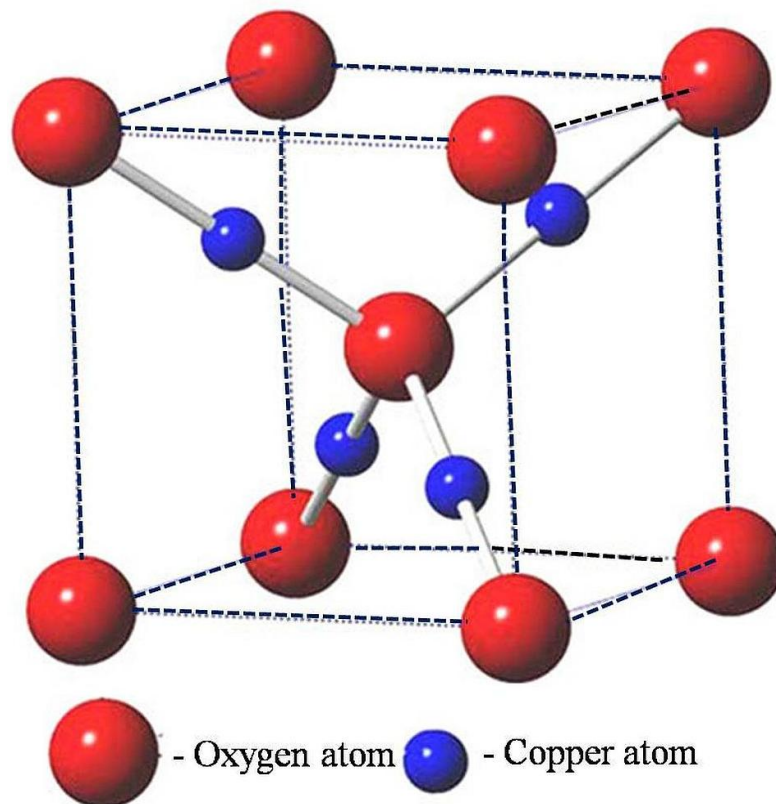
Figure 1.5: Crystal structure of Cu₂O (Cuprite structure). Red balls represent oxygen atom and the blue ones represent copper atom.

Cuprite structure is a three dimensional cubic structures with inversion symmetry (the space group O_h^4) with the unit cell parameter a = 4.27 Å (figure 1.5). In this structure, O atoms occupy the sites of body centered cubic lattice and each atom has four covalent bonds extending in the tetrahedral directions. The adjacent atoms are bridged with each other via a linearly coordinated Cu atom i.e. each Cu atom is coordinated by only two adjacent O atoms. This structure may be also viewed as consisting of two independent and inter-penetrating O-Cu-O zig-zag frameworks with each one equivalent to the cristobalite structure. Apart from cubic structure, it also crystallizes into hexagonal structure under certain experimental conditions [64, 65].

1.3.5. Band Structure

Several theoretical studies have been carried out on the band structure of Cu_2O which includes self-consistent technique based on Local Density Approximation (LDA), Generalized Gradient Approximation (GGA), and Hartree Fock Approximation (HFA) [66, 67]. It is to be noted that the LDA approximation underestimates the energy of the excited states (i.e. the conduction bands), whereas those based on HFA overestimates it. However, the shapes of the conduction bands are qualitatively correct and can be used to visualize the real conduction band by simply shifting them in energy. It is found that the semi-empirical model correctly estimates the band gap energy of Cu_2O compared to the self-consistent model [68].

It can be also shown that Cu_2O is a semiconductor with direct band gap (2.8 eV) at the centre of the Brillouin zone (Γ point). At intermediate and high temperature, the variations of the gap with temperature can be explained by the empirical formula proposed by Varshini [69],

$$E_g\,(T) = E_g\,(0)\,-\,\frac{\alpha T^2}{T+\beta} \tag{1.10}$$

Furthermore, it exhibits large excitonic binding energy of ~ 140 meV which allows the observation series of excitonic features in the absorption and photoluminescence spectrum [70]. The direct band gap of Cu_2O is particularly desirable for solar applications because the light absorption process involves an electron making a direct transition from the valence band to the conduction band without any change in momentum. Practically, this means that Cu_2O can

readily absorb photons and require much smaller thickness to absorb the same number of photons compared to indirect band gap semiconductors [71].

Table 1.2: Physical Properties of Cu$_2$O

Physical Parameters	Values
Density (ρ)	6.10 g/cm
Molecular Mass	143.092 g/mol
Melting point	1235 °C
Relative permittivity	7.5
Electron effective mass	0.98
Hole effective mass	0.58
Cu-O bond length	1.85 Å
O-O bond length	3.68 Å
Cu-Cu bond length	3.02 Å
Band gap energy at room temperature (E$_g$)	2.09 eV
Specific heat capacity (C$_p$)	70 J/(K mol)
Thermal conductivity (k)	4.5 W/(K m)
Thermal diffusivity (α)	0.015 cm^2/s

It is worth stating that, the photovoltaic ability of Cu$_2$O was highlighted by researchers during the mid-seventies due to its high optical absorption properties in the visible region of the electromagnetic spectrum. The material was identified as a possible low cost material for solar cell applications. Cuprite still remains an attractive alternative to silicon and other semiconductors for the fabrication of cheap solar cells for terrestrial applications. The advantage of the materials over others in the photovoltaic field include: (1) abundance, (2) easy preparation and (3) nontoxic nature. Cu$_2$O based solar cells are known to have a theoretical energy conversion efficiency of 22 % in AM1 (Air Mass 1, i.e. on the Earth surface at the equator) conditions [72]. On the basis of band gap energy, the theoretical maximum photocurrent under

AM 1.5 illumination for Cu_2O is 14.7 mA/cm^2, corresponding to a sunlight-to-hydrogen conversion efficiency of 18%. Its conduction and valence bands straddle the water redox potentials, satisfying the requirement for driving overall water splitting. Additionally, its conduction band rests at ~0.7 V negative of the water reduction potential, providing a strong over potential to drive hydrogen evolution. Table 1.2 shows the some important physical properties of Cu_2O [73, 74].

1.3.6. Tin Oxide (SnO_2)
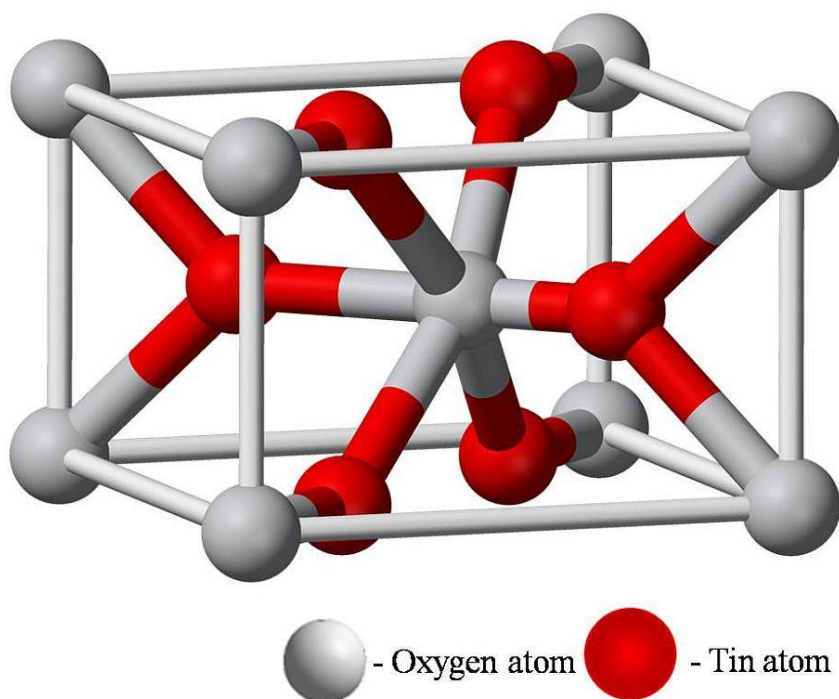
Figure 1.6: Crystal structure of tin oxide (rutile structure). White balls represents oxygen atom and red ones represents tin atom.

SnO_2 is an anisotropic polar crystal, which crystallizes into tetragonal rutile structure of space group $P4_2/mnm$ with the lattice parameters being a = 4.73820 Å and c = 3.18710 Å (figure 1.6). The unit cell contains two tin cations and four oxygen anions. The Sn^{4+} cations are coordinated by six O^{2-} anions, forming slightly distorted octahedra, whereas the oxygens are surrounded by three tin ions, forming an almost regular triangle. The SnO_6 octahedra are connected by common vertices in the ab - plane and by common edges in the [001] direction.

18

Like other metal oxide in SnO_2 also phase transition has been observed, the transition of rutile to pyrite structure, which is analogous to the structure of silica, occurs above the pressure of 21 GPa [75-77].

Table1. 3: Physical Properties of Tin Oxide

Physical Parameters	Values
Density	$6.95g/cm^3$
Stable phase at 300 K	Rutile
Melting point	1630^oC
Thermal conductivity (k)	$0.4 \ Wcm^{-1} \ K^{-1}$
Thermal expansion coefficient	11.7×10^{-6}
Dielectric constant	4.17
Refractive index	2.006
Energy gap	3.57 eV
Electron effective mass	0.35
Hole effective mass	0.69
O-O distance	4.6646 Å
O-Sn distance	3.7662 Å

1.3.7. Band Structure

The band structure of SnO_2 was calculated by the plane wave pseudo potential method, using the generalized gradient approximation (GGA) of the local density formalism (LDF). These LDF and GGA method underestimate the band gap. This error has been corrected in the band structure by introducing the "scissors operator," a rigid upward shift of the conduction bands. The band gap of SnO_2 calculated by LDF and GGA method with the correction by employing scissors operator is 3.6 eV.

Further, the ease of making it n-type, its highly dispersive conduction band (small effective mass), and the large energy difference between the conduction band minimum and the next higher conduction band at Γ contribute to SnO_2 supporting high carrier concentrations while still maintaining a high degree of optical transparency [78, 79]. It is an attractive material not only for the gas sensors but also as a catalyst of the organic compounds oxidation, a key component in Li ion batteries, master element in optoelectronic devices, antistatic coatings, special coatings for energy-conserving windows, dye-sensitized solar cells, and photo catalysts and so on [80-82]. Table 1.3 shows the some important physical properties of SnO_2 [83-86].

1.4. SYNTHESIS METHODS OF ONE DIMENSIONAL (1D) NANOSTRUCTURES

Vertically aligned 1D metal oxide nanorods are of great interest because these structures can be easily made into various functional devices for energy storage, solar cells, and sensing applications.

Various efficient routes have been developed to synthesize well defined 1D nanostructures with controlled sizes and shapes. Roughly, the synthesis routes can be divided into "Top-down" and "Bottom-up" approaches (figure 1.7). Generally, the "Top-down" approach, a solid phase method involves breaking down of a bulk material to generate nanosized structures with high purity. It usually requires high temperature, complex procedure, sophisticated equipment and rigid experimental conditions, such as chemical vapor deposition (CVD), vapor-liquid-solid (VLS) methods, and thermal evaporation [87-89]. In contrast to conditions involved in vapor-phase methods "Bottom-up" approach, a solution phase method involves formation of nanostructures by assembling of atoms/molecules, suitable for large scale and reproducible fabrications of 1D nanostructure due to its simple, fast, convenient and less expensive features. Additionally, the solution phase approach presents a powerful tool not only for providing the control over the size, shape and composition of nanomaterials but also for growing on various conductive substrates [90]. The solution phase chemical route can be roughly grouped into template assisted and template free processes [91-93].
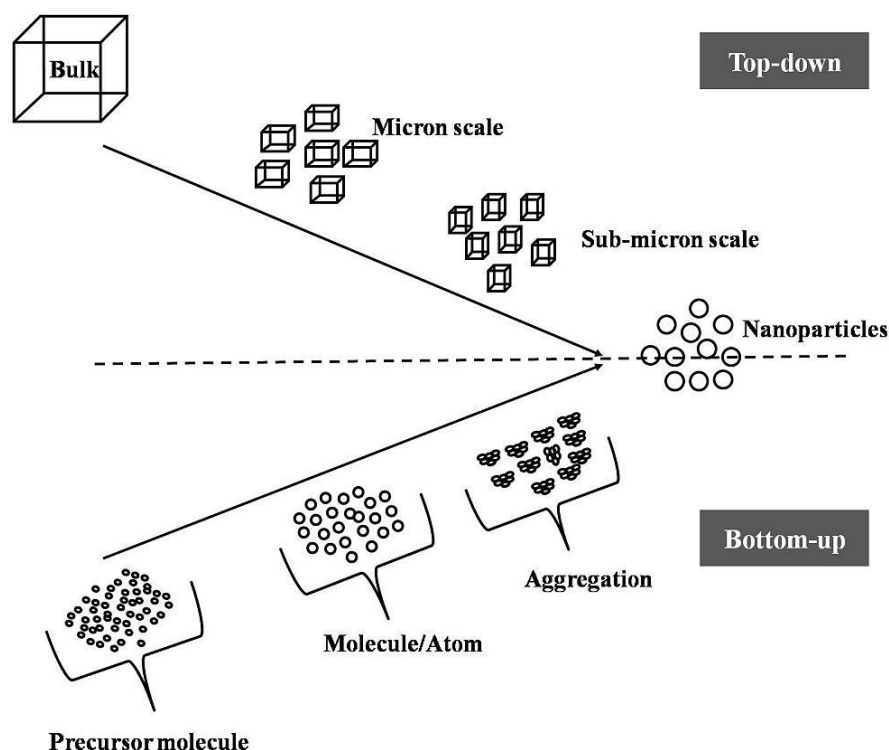
Figure 1.7: Schematic illustration of bottom up and top down approach for the synthesis of nanomaterials.

1.4.1. Template Assisted Method

Template assisted synthesis represents a convenient and versatile method for generating 1D nanostructures. The templates used are divided into two types: the soft templates (surfactant based) and the hard templates. In the soft template technique, the template (surfactant) serves as a scaffold where other materials with similar morphologies are synthesized. The surfactant promoted anisotropic 1D crystal growth has been considered as a convenient way to synthesize metal oxides nanostructures [94]. A classic microemulsion system, such as surfactant phase and aqueous phase, is involved in this anisotropic growth. In the emulsion system, these surfactants serve as micro reactors to confine the crystal growth. The surfactant molecules selectively adsorb and bind onto certain surfaces of the nanocrystals and thus reduce the surface energy and lead to the growth of 1D nanostructures [95].

Porous alumina, carbon nanotubes, polycarbonate membranes and mesoporous materials with nanochannels have been considered as the hard templates for generating 1D nanomaterials. Normally, the nanochannels can be filled with desired material by using solution, sol-gel or electrochemical method [96-98]. The nanowires so formed are obtained by the host matrix removal. The most widely used hard template is anodized aluminum oxide (AAO) membranes, which contain hexagonally packed 2D array of cylindrical pores with a uniform size. Through the electrodeposition and sol-gel deposition methods, 1D nanostructures can be achieved by filling the pores of AAO template. As the diameter sizes of these nanochannels and the interchannel distance are easily controlled, it provides a convenient way to manipulate the aspect ratio and the density of 1D nanostructures [99]. It is also possible to grow 1D nanomaterials without using templates.

The template free method requires in depth understanding of intrinsic structural properties of materials to be synthesized and the ability to activate or deactivate a crystal plane in synthetic 1D nanostructures. For example, OH^- or H^+ concentration in the reaction system could be the key factor controlling the growth rate of different crystal faces and leading to the formation of a rod like morphology. This method often leads to structures with poor reproducibility and hence used for only very special cases. In this thesis, we have used both soft and hard template assisted methods for the growth of 1D ZnO and Cu_2O nanostructures. The more details on the growth techniques we have used and the procedure followed are explained in the respective chapters.

1.5. ELECTRICAL TRANSPORT PROPERTIES OF METAL OXIDE SEMICONDUCTOR

First we will give some background information regarding the electrical contacts on metal oxide and electrical transport, then in the proceeding chapter more detailed information regarding the electrical transport studies that we carried out on 1D ZnO and Cu_2O nanopillars, nanorods will be given.

1.5.1. Ohmic and Schottky Contacts

Any metal-semiconductor based electrical devices have two types of contacts at the junction. An ohmic contact, exhibiting linear I-V characteristics and the rectifying contact

exhibiting non-linear I-V characteristics due to the existence of potential barrier at the junction. The nature of contacts (ohmic or rectifying) primarily depends on the difference in work function between the metal and semiconductor. Work function (ϕ_m) in metal is the energy needed to take an electron at the Fermi level (E_{FS}) and place it outside the metal at rest (E_{vac}). Similarly semiconductor is characterized by its work function (ϕ_s) and electron affinity (χ_s). Here, the electron affinity (χ_s) is defined as the energy difference between the vacuum level and the bottom of the conduction band edge (E_c) [100].
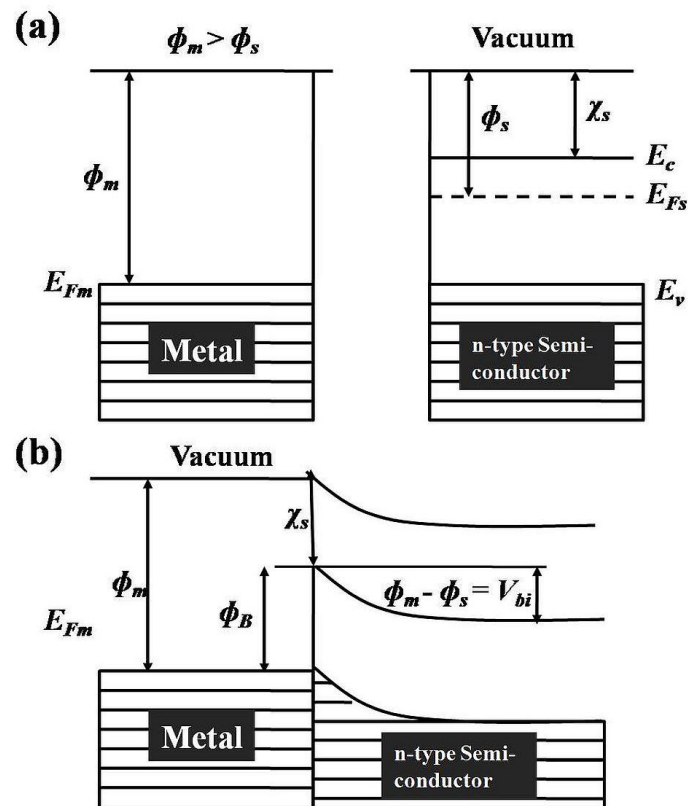
Figure 1.8: Energy band diagram of formation of a metal - n type semiconductor (M-S) contact. (a) before contact (b) after the contact at equilibrium; formation of schottky junction for the case of $\phi_m > \phi_s$.

Figure 1.8a and 1.8b display the energy band diagram of metal and n-type semiconductor with and without contact. The two materials are chosen such that $\phi_m > \phi_s$. When the two materials are brought together in equilibrium, their bands line up and band bending occurs such that E_F is constant and the vacuum level has no step discontinuities. In the band diagram, it is evident that there are two potential barriers V_{bi} (built-in potential) and ϕ_B that prevents the charge

carriers from flowing across the metal-semiconductor interface. A depletion region will form in the semiconductor adjacent to the interface resulting in band bending. The band bending creates a potential difference across the metal-semiconductor interface and any charge carrier had to overcome this potential in order to flow through the device. Therefore the current-voltage characteristics of device with such contacts exhibit rectifying behavior and the potential barrier is called Schottky barrier (ϕ_B). The schottky barrier height in terms of the work function of the metal (ϕ_B) and the electron affinity of the semiconductor (χ_s) is given by,

$$\phi_B = \phi_m - \chi_s \tag{1.11}$$

When the work function of the metal is less than that of semiconductor, the electrons from the semiconductors flows into the metal until the Fermi level reaches equilibrium across the junction. In this situation, I-V curves of the device appear linear and the contact is termed as ohmic contact. The potential barrier is either non-existent or small enough to be overcome by a small voltage. Such a contact is sometimes termed a negative Schottky barrier, while rectifying junctions are deemed positive Schottky barriers.

It is to be noted that, the other intrinsic factors such as the presence of surface states (charge states present at a semiconductor surface) in the semiconductor's band gap often causes the pinning of the Fermi level to lie inside the semiconductor band gap, regardless of the choice of metal for the junction. This pinning effect thereby creates a Schottky barrier whose magnitude is independent of the work function of the metal. [101-103].

1.5.2. Effect of External Bias on Barrier Potential

It is very crucial to see the band diagram of the metal - semiconductor junction under an applied voltage (figure. 1.9). A positive voltage can reduce the barrier, and a negative voltage will increase it depending upon the nature of barrier formed at the junction. Following are the various mechanisms by which electron transport across the barrier can takes place. [103].

1. Thermionic emission over the top of the barrier.

2. Thermally assisted tunneling through the barrier.

3. Direct tunneling through the barrier.
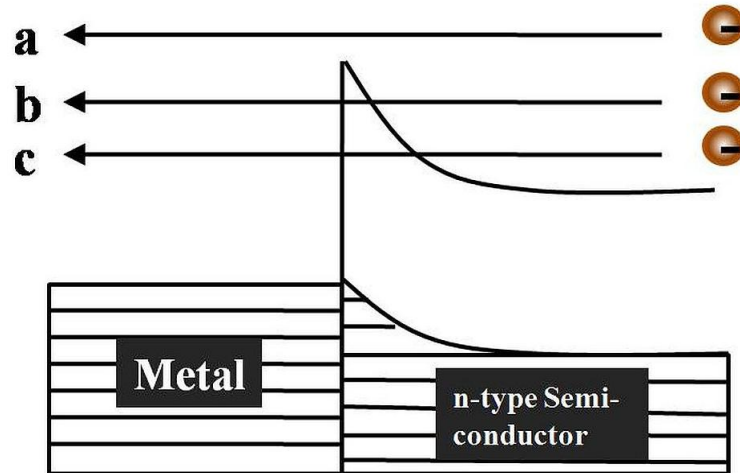
Figure 1.9: Electrical transport in a forward biased schottky junction. (a) Thermionic emission over the barrier (b) Thermally assisted tunneling through the barrier and (c) Direct tunneling from the bottom of the conduction band.

1.5.3. Thermionic Emission

Thermionic carrier injection is the phenomenon by which carriers thermal energy is sufficient to overcome the potential across the interface (i.e. $kT > \phi_B$). In metal-semiconductor junction with small barrier potential, this carrier injection results in Ohmic contact. However at low temperatures the effect of potential barrier shows up and the contact becomes Schottky. This is one of the reasons for many devices to become highly resistive at low temperature. Since thermally excited carriers (represented by (a) in figure 1.9) can flow both ways, an expression for the total current due to thermionic emission is determined by subtracting the current which flows from the metal to the semiconductor $I_{M \to S}$ from the current flowing from the semiconductor to the metal $I_{S \to M}$.

By subtracting the current which flows from the metal to the semiconductor $I_{M \to S}$ from the current flowing from the semiconductor to the metal $I_{S \to M}$, the following expression for the total current I is obtained [116].

$$I = A^* A T^2 \exp\left(-\frac{q\phi_B}{k_B T}\right)\left[\exp\left(\frac{qV}{nk_B T}\right) - 1\right] \quad (1.12)$$

where q is the charge of the electron, k_B the Boltzman constant, T the temperature, A^* the Richardson constant, ϕ_B the barrier height and n the ideality factor (unity for purely thermionic emission dominated transport), and A^* is given by [104],

$$A^* = \frac{4\pi e m_e^* k_B^2}{h^3} \tag{1.13}$$

where m_e is the effective mass of the electron.

1.5.4. Electron Transport by Tunneling (Thermally Assisted Tunneling and Direct Tunneling)

Tunneling is a quantum mechanical phenomenon in which electrons penetrate a potential barrier even though their energy is less than the height of the barrier. This phenomenon is dominant at low temperature regime where the thermal energy has little or no effect. At very low temperatures electrons tunnel directly through the barrier (direct tunneling, represented by (c) in figure 1.9) and at intermediate temperatures electrons first get thermally excited before tunneling across the high potential (thermally assisted tunneling, represented by (b) in figure 1.9). In the direct tunneling regime the current is given by:

$$I = I_S \left[\exp\left(\frac{qV}{E_{00}}\right) - 1 \right] \tag{1.14}$$

where E_{00} is given by,

$$E_{00} = \frac{\hbar}{2} \sqrt{\frac{N_d}{m^* \varepsilon_s}} \tag{1.15}$$

The saturation current density I_s depends weakly on temperature as $cT = sin\ (cT)$, where c is a constant. In the thermally assisted tunneling regime, the current density is given by [173]

$$I = I_S \left[\exp\left(\frac{qV}{E_0}\right) - 1 \right] \tag{1.16}$$

and

$$E_0 = E_{00} \coth\left[\frac{qE_{00}}{kT}\right] \qquad (1.17)$$

where, E_{00} is a tunneling parameter (also called as characteristic energy). E_{00} ($T = 0$ K) is 1, (Eqn.1.15) hence E_0 ($T = 0$ K) equals E_{00}. It also implies that for this case Eqn. 1.16 approaches to Eqn. 1.14 at very low temperatures.

1.6. GAS SENSORS

Gas sensing is extremely important to detect toxic gases in environment, monitor ambient air quality, checking gas leakage in pipelines and for safe transport of dangerous gases such as Hydrogen. Among many different gases, the rapid detection of hydrogen is technologically essential because it is colorless, odorless, and highly explosive [105]. Various kinds of gas sensors have been extensively explored and developed, including solid electrolyte gas sensors, metal oxide gas sensors and electrochemical gas sensors. Of all these, metal oxides represent an appealing class of materials owing to their high sensitivity to most gases, low cost, and simple fabrication techniques [106, 107].

The recent advent of nanotechnology led to the development of metal oxide-based gas sensors, in the form of nanowires, nanoflakes or nanoparticles. The larger surface-to-volume ratio in these nanostructures greatly improved the sensor response. But still there are some unresolved issues for these metal oxide nanostructure based gas sensors such as the relatively high operating temperatures (usually over 200 °C) as well as the long response and recovery times. The high operating temperatures would impose a substantial safety risk during the gas detection and consume considerable amount of energy for their operation. The requirement for high operating temperature is due to the presence of large energy barrier at the surface of the active material [108]. To overcome this difficulty, one needs to develop a composite in which the host material which encapsulates the active material (metal oxide nanostructures) acts as a catalyst for electron transfer across the energy barrier.

One of the promising candidates for host material is two dimensional reduced graphene oxide (RGO). It is a chemically modified graphene with high surface area (2630 m^2/g) containing small amount of oxygen functional groups such as alcohols, carboxylic acids and epoxides [109-111]. It can be easily synthesized in large scale using inexpensive facile chemical

approaches and can be easily processed into continuous paper like structures [112-115]. Since the properties such as conductivity and tensile strength of RGO mainly depend on the amount of functional groups present, they can be easily fine tuned by adjusting the reduction conditions. Furthermore, the functional groups present in the RGO allow it to functionalize (chemical modification), with different nanomaterials such as nanoparticles and nanorods/nanowires, which potentially makes RGO a versatile material for the gas sensing applications [116-118].

The incorporation of RGO into metal oxide nanostructures or vice versa results in the following advantages over the individual component. First, the large 2D flexible area of reduced graphene oxide can accommodate nanomaterials (nanoparticles/nanorods) without forming aggregates. The high electrical conductivity of RGO could facilitate fast electron transport in catalytic (sensing) reaction. Thirdly, the structural defects (functional groups) present in the RGO will provide more room for the functionalization of more nanomaterials. On the basis of this advantages the metal oxide nanostructures anchored/coated RGO based composites have emerged as one of the promising candidate for the development of next generation gas sensors. By considering all the advantages of nanocomposites, in this research work we have synthesized RGO/SnO$_2$ NFs and RGO/MoS$_2$ NPs composites for hydrogen sensors. A detailed study on the preparation of composites and their sensing measurement studies will be discussed in chapters 4 and 5 respectively.

1.7. CHARACTERIZATION TOOLS

After the synthesis of nanomaterials, to understand the structural, morphology, and compositional characteristics different characterization techniques were used. In the proceeding section a brief description of the techniques used and their working principle will be given.

1.7.1. X-Ray Photoelectron Spectroscopy (XPS)

The modern technique of X-ray photoelectron spectroscopy (XPS) was founded by K. M. Siegbahn, earning him the Nobel Prize for Physics in 1981. It is working on the principle of photoelectric effect. When a sample is placed within a beam of X-ray, photoelectrons are ejected from the atoms within the material. X-rays have enough energy to eject electrons from the core orbitals of all atoms as shown in figure 1.10. By dispersing the ejected electrons according to energy, a spectrum of binding energies is obtained.
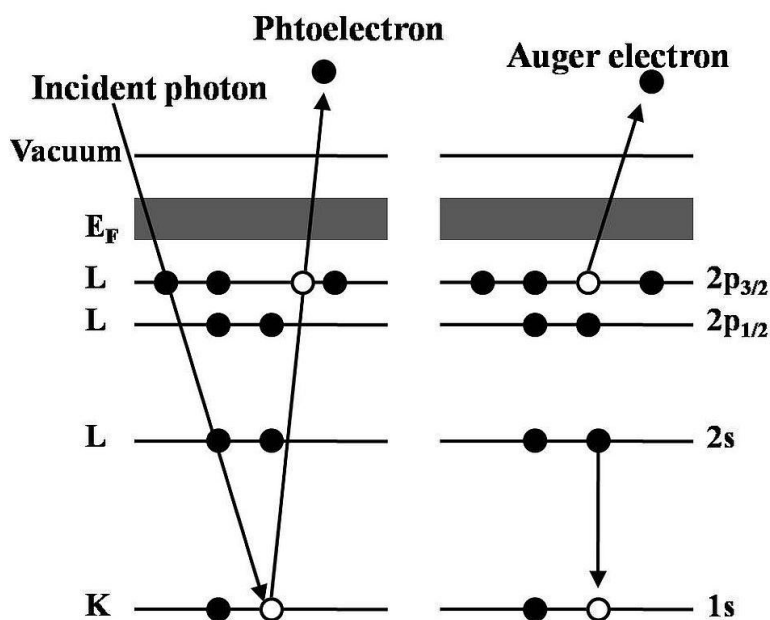
Figure 1.10: X-ray photoemission and Auger electron emission

The locations of peaks in the XPS spectrum indicate both the presence of specific elements and their respective oxidation states. Furthermore, the binding energy of core electrons is very sensitive to the chemical environment of the corresponding element. When the same atom is bonded to a different chemical species, this leads to a change in the binding energy of its core electrons. The variation of binding energy results in a shift of the corresponding XPS peak. This effect is termed as chemical shift, which can be applied to study the chemical status of all elements in the surface. Therefore, XPS is also known as electron spectroscopy for chemical analysis (ESCA). The intensity of photoelectron peak varies with the surface concentration of the corresponding element, allowing quantitative determination of the composition of the surface. This paved the way for photoemission to become one of the most successful techniques for the study of the chemical and electronic properties of materials, by allowing direct access to the density of states (DOS) at the surface [119, 120].

Figure 1.11 shows the basic elements of an XPS instrument consisting a light source, an electron energy analyzer and an electron detector.
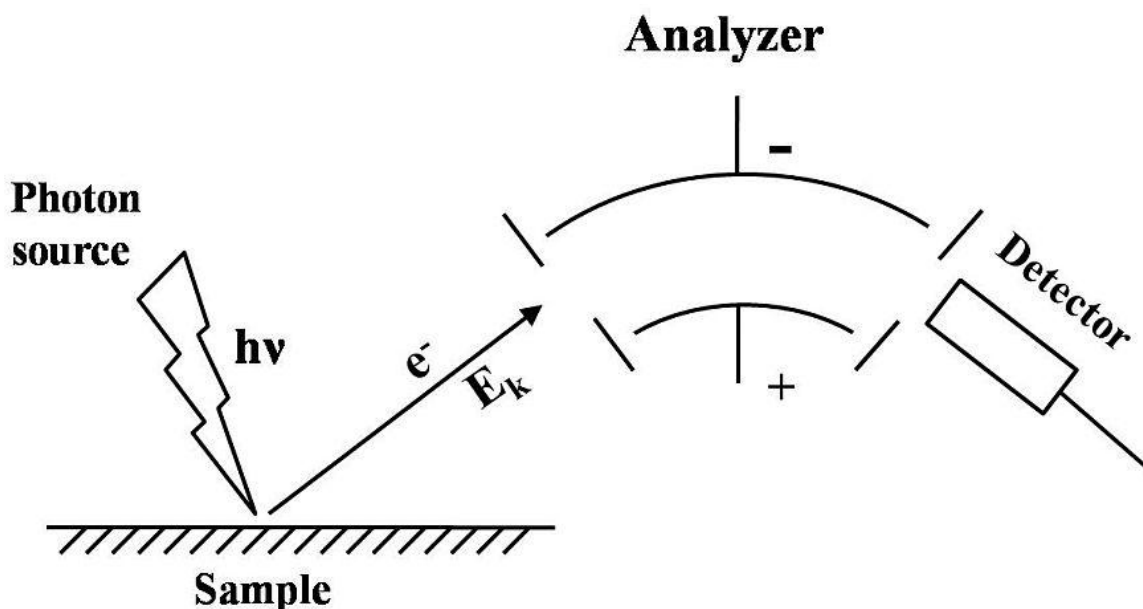
Figure 1.11: Basic elements of XPS experiment

1.7.2. X-ray Diffraction (XRD)

X-ray diffraction (XRD) is a crystallographic technique employed for identification and quantification of various crystalline phases in solid materials and powders [121, 122]. The crystal structure and grains size can be determined via the XRD. In this technique, a beam of X-rays are directed at a sample and proportions of them are diffracted to produce a pattern. By comparison of those diffracted pattern with the reference patterns, the crystal phases of the sample can be identified.

Figure 1.12 presents the diffraction of X-rays by parallel planes (illustrated as horizontal lines) in a crystal in the XRD technique. A monochromatic X-rays beam with wavelength λ is directed onto the crystalline material with inter planar spacing d, at an angle θ and then diffracted when leaving the various planes. The diffracted wave pattern can be in or out of phase to produce either destructive or constructive interference. Each diffracted X-ray signal corresponds to a coherent reflection is called Bragg reflection. The constructive interference patterns only occur when incident angles satisfy the Bragg's law:

$$n\lambda = 2d \sin \theta \tag{1.18}$$

where $n = 1, 2, 3, \ldots$ is the order of diffraction, λ is the X-rays wavelength, d is the spacing between atomics planes in the crystalline phase and θ is the Bragg angle. In a XRD pattern, the intensity of the diffracted X-rays is plotted with the detector angle 2θ. The intensity and angle of a set of peaks is unique to the crystal structure of the examined material.
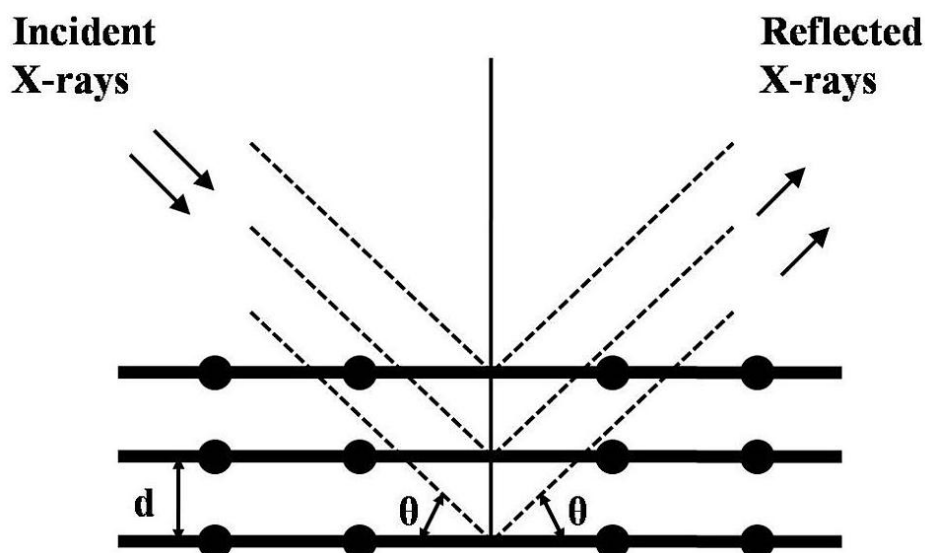
Figure 1.12: Diffraction of X-rays by lattice planes in a crystal using XRD technique.

1.7.3. Scanning Electron Microscopy (SEM)

Scanning electron microscopy (SEM) technique is a powerful tool for studying the morphological and structural features of the nanomaterials [119]. It produces images of the sample by scanning it in a raster pattern on the specimen surface with a focused beam of electrons. The interaction between the electron beam and the specimen surface produces various types of energetic emissions, including back scattered electrons, secondary electrons, Auger electrons, continuous X-rays and characteristics X-rays. The electrons interact with atoms in the sample, producing various signals, containing information about the samples surface topography and composition, which can be detected using specialized detectors.

The schematic image of SEM is illustrated in figure 1.13. The SEM uses electrons instead of light (compared to optical microscope) to form an image. A beam of electrons is produced at the top of the microscope by heating of a metallic filament. The electron beam

follows a vertical path through the column of the microscope. It makes its way through electromagnetic lenses which focus towards the sample. Once it hits the sample, some are backscattered and others produce a secondary electron by knocking out electrons from the sample. Detectors collect the secondary or backscattered electrons, and convert them into a signal that is sent to a viewing screen producing an image [123].
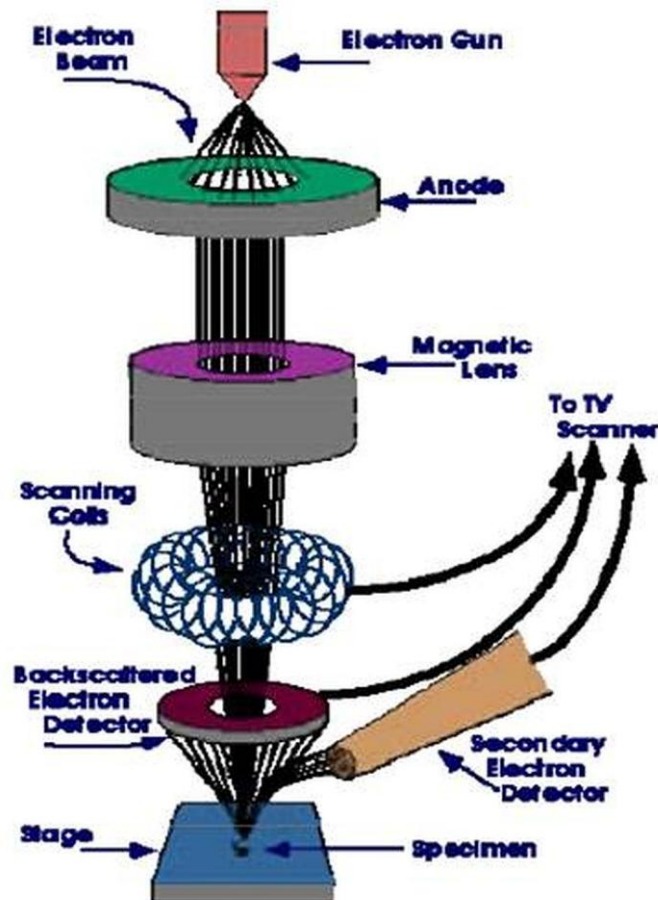
Figure 1.13: Schematic illustration of scanning electron microscope (SEM)

1.7.4. Atomic Force Microscope (AFM)

The atomic force microscope (AFM) is a very high resolution type of scanning probe microscope, with demonstrated resolution of fractions of a nanometer, more than 1000 times better than the optical diffraction limit. Binnig, Quate and Gerber invented the first AFM in 1986 [124]. The AFM is one of the foremost tools for imaging, measuring and manipulating

matter at the nanoscale. Figure 1.14 illustrates the block diagram of AFM. The AFM consists of a microscale cantilever with a sharp tip (probe) at its end that is used to scan the specimen surface. The cantilever is typically silicon or silicon nitride tip with radius of curvature in the order of nanometers. The AFM works by scanning a tip over a surface, when the tip is brought into proximity of a sample surface, Van der Waals forces between the tip and the sample lead to a deflection of the cantilever. The magnitude of the deflection is captured by a laser that reflects at an oblique angle from the very end of the cantilever. A plot of the laser deflection versus tip position on the sample surface provides the topography of the surface [125].
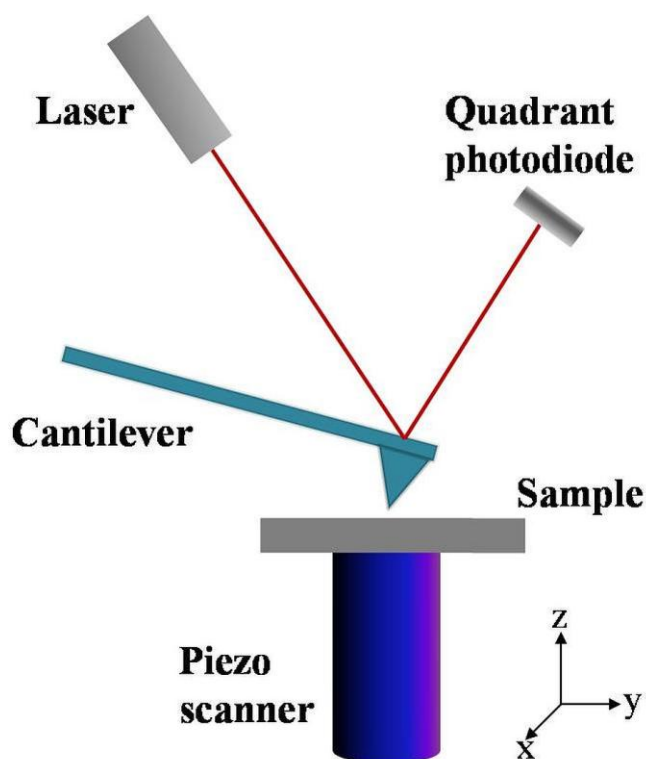
Figure 1.14: Schematic Diagram of Atomic Force Microscope (AFM).

1.7.5. Raman Spectroscopy

Raman scattering is a powerful light scattering technique used to determine the composition of the materials qualitatively and quantitatively. In a light scattering experiment, light of a known frequency and polarization is scattered from a sample. The scattered light is then analyzed for frequency and polarization. Raman scattered light is frequency shifted with

respect to the excitation frequency, but the magnitude of the shift is independent of the excitation frequency. This "Raman shift" is therefore an intrinsic property of the sample [126].
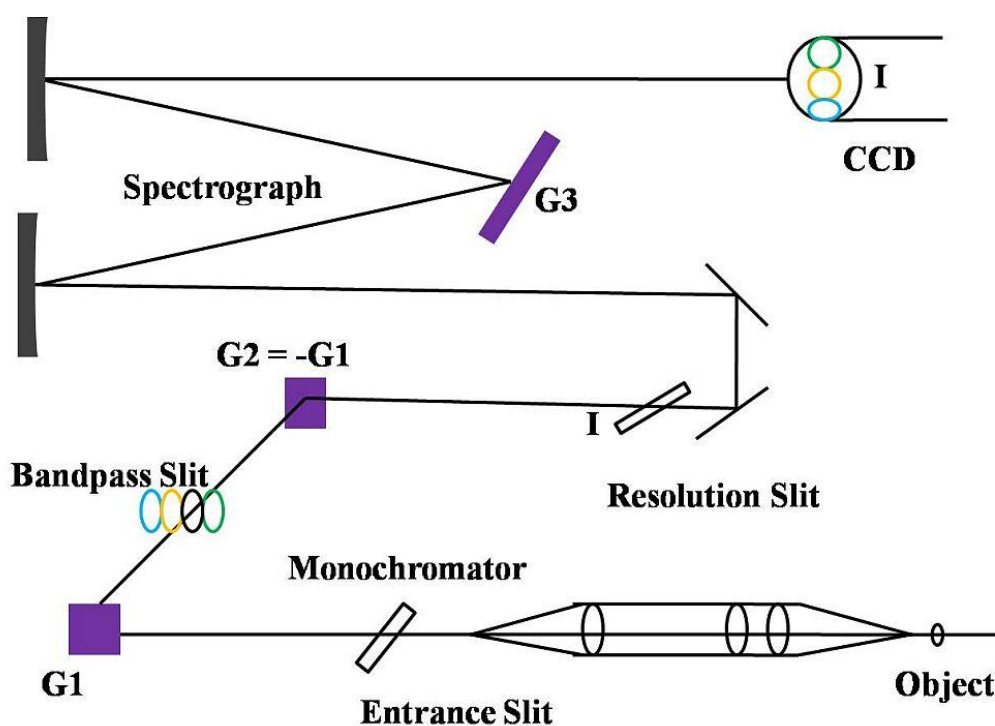
Figure 1.15: Schematic representation of Raman spectrometer

Raman spectroscopy usually consists of three parts: Laser, spectrometer and charge coupled device array (CCD) detector. The spectrometer itself is a commercial "triple-grating" system. Physically, it is separated into two stages, i.e. monochromator and spectrograph, which are shown schematically in figure 1.15. The laser beam from the laser is filtered for monochromatic and directed by a system of mirrors to a focusing/collecting lens. The beam is focused onto the sample; the scattered light which passes back through the same lens is then passed through a second lens into the monochromator of the spectrometer. Finally the light is refocused and sent out to the spectrograph of the spectrometer to focus the filtered light on the final grating. The dispersed light is now analyzed as a function of position, which corresponds to wavelength. The signal as a function of position is read by the system detector. The wavelength/intensity information is then read to a computer and converted in software to frequency/intensity [127, 128].

1.9. OBJECTIVE

Free standing 1D metal oxide (ZnO and Cu_2O) nanostructures in the form of nanowires and nanopillars have the potential to become central component in the electronics and sensing applications. To make use of these nanostructures for practical applications, it is essential to understand their electrical transport characteristics. Similarly reduced graphene oxide (RGO) and its nanocomposites are considered to be the suitable candidates for next generation gas sensing devices. However, devices made up of this materials still lacks the qualities (high temperature, high response time and recovery time) for commercial applications. For good hydrogen sensing characteristics, it is very important to find new materials combinations to overcome the obstacle put forth by the current materials. Based on these problems, the objective of this thesis work has been divided into

➢ Optimizing the growth process for realizing n-type vertically aligned ZnO oxide nanorods with high aspect ratio, good crystalline structure and uniform morphology and study of its temperature (10 K – 298 K) dependent transport characteristics.

➢ Growing of vertically aligned p-type Cu_2O oxide nanopillars with high aspect ratio and characterizing them with temperature (180 K - 300 K) dependent I-V techniques.

➢ Synthesis of reduced graphene oxide (RGO) and RGO-SnO_2 nanoflower based nanocomposites for highly selective, responsive and low temperature hydrogen sensing application.

➢ Synthesis of reduced graphene oxide and RGO/MoS_2 nanoparticles based nanocomposites for highly selective, responsive and low temperature hydrogen sensing application.

CHAPTER TWO

IN-SITU REDUCED GRAPHENE OXIDE INTERLAYER FOR IMPROVING ELECTRODE PERFORMANCE IN ZnO NANORODS

2.1. INTRODUCTION

For any practical applications and electrical transport measurements, ZnO NRs have to be grown on various conductive substrates such as Indium Tin Oxide (ITO) and silicon (Si) so that it can be easily integrated with the existing technology. In this work, we have chosen hydrothermal technique for the growth of ZnO NRs on ITO substrates. However, the problem associated with hydrothermal technique is that though it yields highly crystalline materials, there exist physical gap between the nanorods and also the length of grown nanorods is limited to the order of few tens of nanometers [129-135]. This makes it difficult to fabricate reliable electrical contacts, which are essential for optoelectronic device application and undertaking vertical transport measurement without using expensive space fillers such as polymethyl methacrylate (PMMA) as a short circuiting inhibiter [136-138]. The presence of polymer over ZnO nanostructures will definitely affect its inherent physical and chemical properties [139, 140]. In cases where metals such as gold (Au) and platinum (Pt) were successfully deposited directly on ZnO NRs, it usually resulted in Schottky contact with high potential barrier. Post deposition surface treatments and high temperature annealing procedure were carried out to reduce the contact resistance which had a negative impact on the performance, reliability and life cycle of the devices [141, 142].

It is therefore necessary to find a new technique to realize good ohmic contacts which is cost effective, easy to process and suitable for various device applications. Reduced graphene oxide (RGO) can be a suitable candidate for electrode material on ZnO NRs [143-145]. RGO is electrically very conducing, optically very transparent, non-permeable to any organic or inorganic species and can be made extremely thin [146, 147]. It also has large number of dangling bonds which allows it to make a strong bond with any material over which it is drop casted.

In this work, we have devised a simple technique for the formation good quality ohmic contacts on vertically aligned ZnO nanorods grown on ITO, which do not require any expensive

space fillers such as PMMA, time consuming surface cleaning procedures, sophisticated high vacuum technique for metal deposition and high temperature annealing process. In this technique, chemically processed graphene oxide (GO) was reduced on vertically aligned ZnO NRs at temperature as low as $60^{\circ}C$ which is much lesser than the temperature used for conventional reduction process. The in-situ reduced graphene oxide (RGO) not only acts as a short circuit inhibitor but also facilitates the formation of good ohmic contact on vertically aligned ZnO nanorods. By using RGO as an interlayer between metal and ZnO, we were able to study the electrical properties of ZnO at temperatures as low as 10 K. From the temperature dependent current voltage (I-V) curves, we were able to measure the activation energy of shallow donor sites in ZnO nanorods.

2.2. MATERIALS AND EXPERIMENTAL METHODS

All materials used (Sigma Aldrich, India and SD Fine chemicals, India) in this experiments were of analytical reagent grade and used without any further purification. All the aqueous solutions were prepared using Deionized (DI) water.

2.2.1. ZnO Nanorods Growth

Vertically aligned ZnO NRs were grown using hydrothermal method. In the following section, first we will give general information on the hydrothermal technique followed by detailed experimental procedure used for the growth of ZnO NRs.

2.2.2. Hydrothermal/Solvothermal Method

The term hydrothermal is of purely geological origin and it was first coined by the British Geologist Sir Roderick Murchision (1792-1871), to describe the action of water under elevated pressure and temperature in bringing changes in the earth's crust, leading to the formation of various rocks and minerals [148-149].

Hydrothermal usually refers to any heterogeneous reaction in the presence of aqueous solvents or mineralizers under high temperature and pressure conditions which dissolve and recrystallizes into materials that are relatively insoluble under ordinary conditions. Based on the previous research works K. Byrappa and M. Yoshimura had proposed to define a hydrothermal reaction as "any heterogeneous chemical reaction in the presence of a solvent (whether aqueous

or non aqueous) above room temperature and at pressure greater than 1 atm in a closed system [150]."
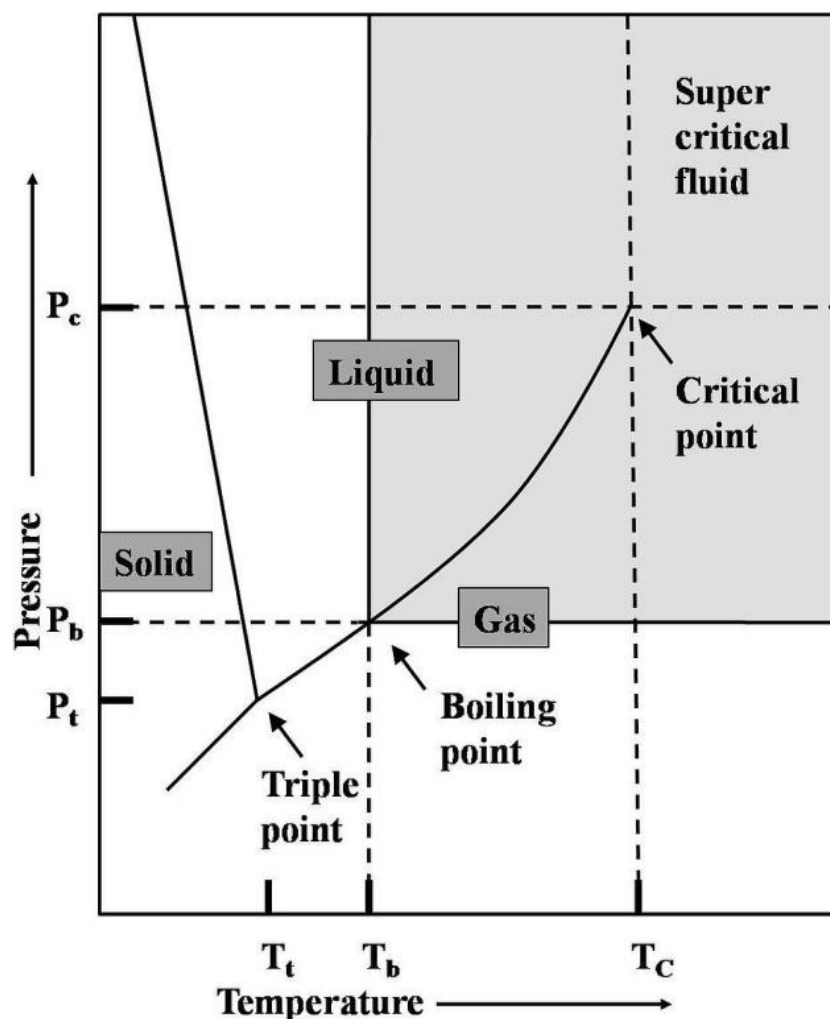
Figure 2.1: Schematic phase diagram of water showing the important zones for hydrothermal processing. P_t, T_t and P_b, T_b indicates the triple point and boiling point respectively, while P_c, T_c are the pressure and temperature of the critical point (374°C and 221 bar). The curve indicates the condition for autogeneous water pressure, while high pressure hydrothermal synthesis is conducted in the whole temperature range of fluid existence above the P_c.

Hydrothermal processing is a non-conventional method to obtain nanocrystalline inorganic materials. As implied by the name, water at elevated temperature plays an essential role in the transformation of the precursor material. In a typical reaction, a precursor and a

reagent which is capable of regulating the crystal growth are added into water with appropriate ratios. This mixture is placed in an autoclave to allow the reaction to proceed at elevated temperature and pressures. The reaction time ranges from a few hours to a few days. The major advantage of this approach is that most of the inorganic materials can be made soluble in water at elevated temperatures and pressures. As such, it is suitable for use with any solid material. Figure 2.1 shows the schematic phase diagram of water showing the important zone for hydrothermal processing. It indicates the presence of two different hydrothermal pressure ranges namely the autogenous and high pressure range.
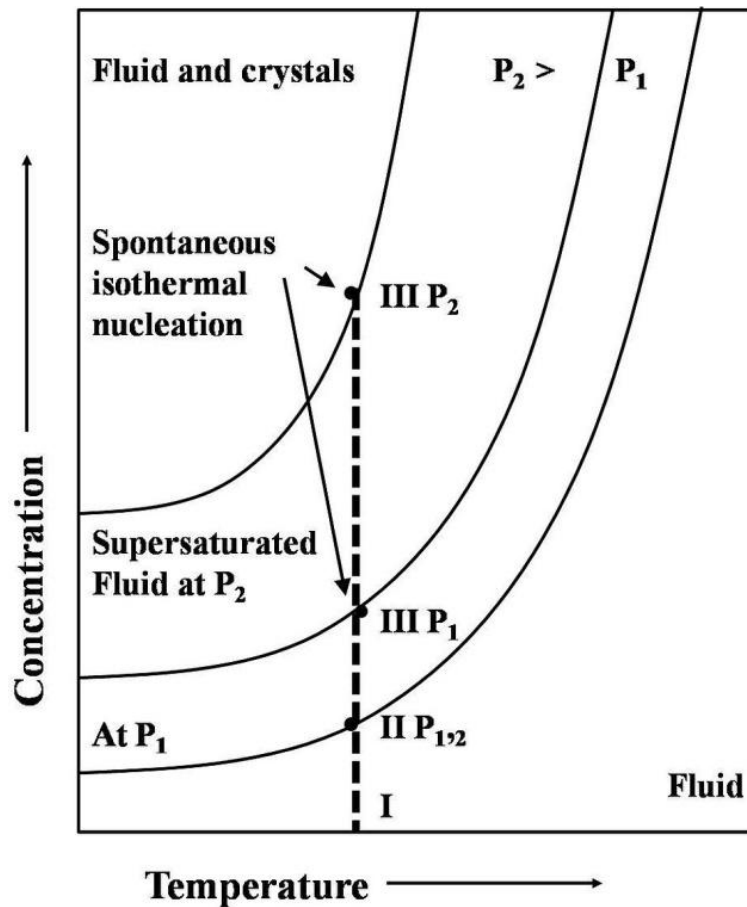
Figure 2.2: Isothermal-isobar hydrothermal processing: (I) only water and precursor materials are present. (I) and (III): time dependent precursor material dissolution. Nucleation occurs spontaneously if point (III) is achieved and subsequent crystal growth in the saturated solution.

There are many parameters which greatly increases the complexity of the reaction in hydrothermal process. For example, it is known that temperature plays significant role in kinetics of product formation as well as the thermodynamic stability of the product and the pressure controls the supersaturation range directing the product phase (e.g. crystallization of a denser phase will occur at high synthesis pressure). Time is also an important parameter because time allows kinetically stable phase to manifest in due course [151].

The principle of the hydrothermal process of dissolution–supersaturation and subsequent crystallization is shown in figure 2.2. Standard hydrothermal experiments are conducted under isothermal and isobar conditions without agitation. At the beginning of the experiment, the hydrothermal fluid consists only of water with solid precursor materials (point I); it gets more and more concentrated with time. Near the solubility limit of the product phase (point II, supersaturation), the precursor can still be dissolved. At a certain level of supersaturation (point III), spontaneous crystallization will finally occur, leading to a decrease of the concentration in the hydrothermal fluid.

As explained above, the growth of 1D metal oxide materials during the hydrothermal process occurs due to dissolution-reprecipitation method, which includes dissolution of precursor, diffusion of precursor species, and precipitation. However, the growth along one specific direction can be achieved only if the material possesses anisotropic crystallographic structure. The use of surfactant (additives to the precursor) also plays a significant role in determining the 1D growth of metal oxides.

2.2.3. ZnO Nanorods by Hydrothermal Growth Method

ZnO nanorods were grown on conductive ITO, with the surface resistivity of $\sim 70 \ \Omega/\text{sq}$, substrate and p-type silicon substrate with SiO_2 layer of 100 nm by surfactant (soft) assisted hydrothermal growth.

Before growing nanorods, all the substrates were subjected to standard cleaning procedure which consists of sonication in acetone and ethanol for 20 min followed by washing with DI water and drying in convection air oven until the water dries. The nanorods growth procedure consisted of two steps namely (1) Seed layer preparation and (2) Hydrothermal growth of ZnO NRs, which are given below in detail.

Seed Layer Solution Preparation:

1) 0.0219 g of Zinc Acetate Dihydrate was measured

2) Then it was added to 20 ml of absolute ethanol in 100 ml beaker

3) Followed by magnetic stirring for 2hr on hot plate maintaining at 60°C.

4) After 2 hrs magnetic stirring, the solution was taken off from the hot plate and was cool down to room temperature naturally.

5) 2µl of as prepared seed (above) solution was drop cast on ITO substrate and heated to 60°C until all the ethanol evaporated.

6) The same procedure was repeated for 10 times as given in point 5.

7) After drop casting procedure was over, all the substrates were washed with copious amount of ethanol to remove the residues on the substrates.

8) Finally, the drop cast ITO substrate was annealed in tube furnace at 325^0C for 15 min with the following settings (table 2.1).

Table: 2.1: Annealing Parameters of seeded ITO substrate

Parameters	Set values
Temperature	*325^0C
Time to attain set value	5 min
Holding time (at 325^0C)	10 min
Room temperature	Natural cooling

*± 5 degree was observed in the temperature set values

Preparation of ZnO Nanorod Growth Solution

1. 0.594 g of Zinc nitrate was added to 40 ml of DI water followed by magnetic stirring for 30 min.

2. 0.280 g of hexamethylenetetramine (HMTA) was added to the above solution followed by magnetic stirring for 30 min.

3. After 30 min of stirring, the as prepared growth solution was transferred to custom made Teflon coated autoclave along with seeded ITO substrate (fixed inverted in the teflon holder).

4. For the growth of ZnO NRs on seeded ITO substrate, the autoclave was placed inside the

oil bath at 93°C ± 1 for 4 hr.

5. Finally the substrate was taken out from the autoclave and cleaned with copious amount o f DI water followed by drying in convection air oven at 60°C for 24 hr. Figure 2.3 shows the hydrothermal setup (Teflon lined autoclave (50 ml) and teflon made nut and bolt whic h was used as the seeded substrate holder for the experiment) used in this research work.
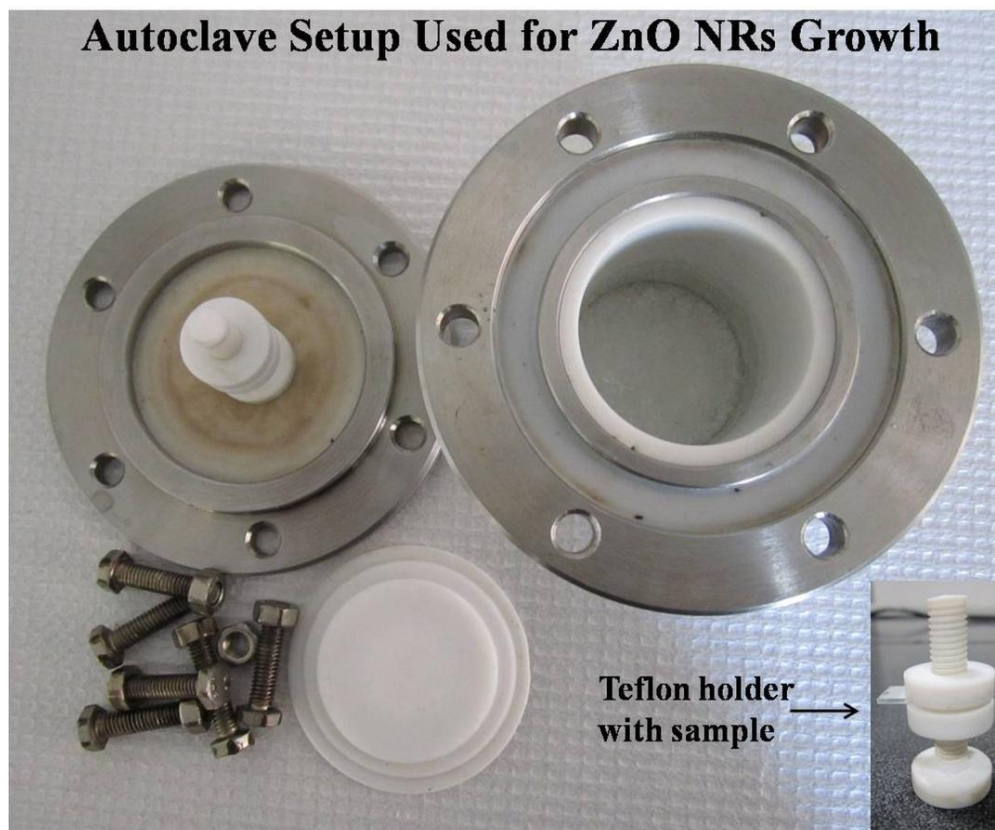
Figure 2.3: Experimental setup used for the hydrothermal growth of ZnO NRs on ITO substrate

2.2.4. Synthesis of Graphene Oxide (GO)

The thin film GO was synthesized from graphite flakes by Hummers method. 0.5 grams of natural graphite is mixed with 0.35 gms of NaNO$_3$ (99% purity). About 30.7 gms of conc. Sulphuric acid (96% purity) was slowly added to the mixture with continuous stirring in ice water bath. 1.95 gms of potassium permanganate was gradually added and the resultant mixture was cooled for 1 hour. The mixture was stirred continuously for 5 days at 20° C. The mixture is

then diluted with 50 ml of aqueous solution of 5% weight Sulphuric acid and 1.5 gms of 30% weight H_2O_2 is added to remove ions of oxidant origin. Further purification process is performed by repeated rinsing with de-ionized water to get highly purified GO thin films [152] (figure 2.4d). 2.5 ml of as prepared solution was added to 7.5 ml of DI water and it was ultrasonicated for one hour followed by centrifugation at 15000 rpm for 10 minutes. Finally, the supernatant solution (GO) was collected in a centrifuge tube and stored at room temperature for further use.

2.2.5. Formation of Top Electrical Contact on Vertically Aligned ZnO NRs
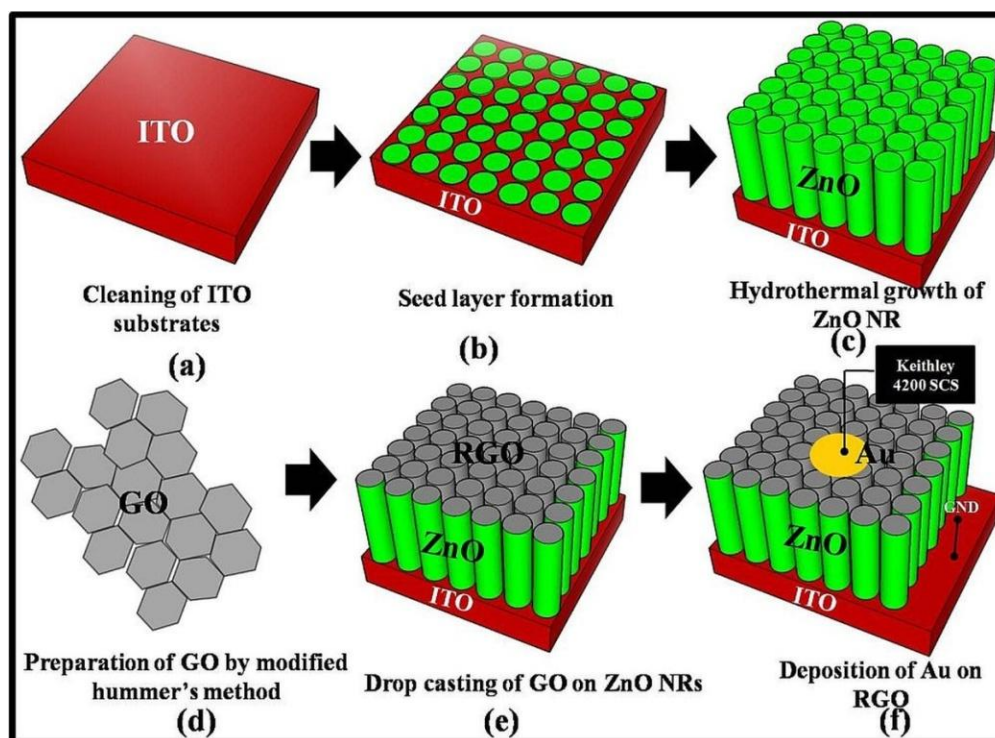
Figure 2.4: Schematic Illustration of fabrication process of RGO-ZnO NRs heterostrcutres (a) cleaning of ITO substrate. (b) Formation of seed layer at $350^{o}C$. (c) Hydrothermal growth of ZnO NRs at $90^{o}C$. (d) Synthesis of GO by modified Hummer's method. (e) Reduction of GO into RGO at $60^{o}C$ on top ZnO NRs. (f) e-beam evaporation of Au on RGO for electrical measurements.

For the formation of electrical contacts, 120 µl of as synthesized GO solution was drop casted on the ZnO nanorods while simultaneously heating at $60^{0}C$ to convert them into partially reduced RGO (figure 2.4e). 300 nm layer of gold was deposited as a top metal electrode for the

RGO/ZnO nanorod heterostructure. The deposition was performed under a pressure of 10^{-6} mbar at the rate of 15 nm/min. Current-Voltage (I-V) measurements were performed at different temperatures in two terminal configuration by using ITO substrate as a bottom electrode. Low temperature measurement was performed by loading the sample in a closed cycle cryostat. Prior to loading the sample, the top and bottom electrodes are electrically connected to the contact pads of the chip carrier by aluminum wire using silver paste as an adhesive.

To verify the reproducibility of our method four devices were fabricated using the same experimental conditions. All the devices exhibited similar electrical characteristics with little more or less resistance values confirming the reproducibility of this method.

2.2.6. Electrical Measurement

The electrical transport properties of vertically aligned ZnO NRs were carried out in two terminals (top and bottom) configuration. During the measurement, voltage V is forced on the top contact of the ZnO NRs and the current I is measured across the ZnO NRs.

At Room Temperature

After the formation of electrical contacts, the quality of each device was verified by performing room temperature I-V measurement. To avoid driving high current to the devices, the voltage range for the measurement was identified by trial and error method (By varying the sweeping voltage ranges). All the room temperature I-V measurement was carried out in dark by contacting the device using signatone micropositioners fixed with tungsten probe tips (SE-T) holders (figure 2.5).

At Low Temperature

Once the quality of the device was verified at room temperature, it was loaded into the closed cycle cryostat (Janis, USA) for investigating the temperature (10 K to 298 K) dependent electrical transport properties. The electrical connections from the sample were drawn using 8-pin feedthroughs. Then the samples were connected to 4200 SCS (Keithley, USA) by custom made radiation shield box made up of aluminum using BNC cables. Prior to low temperature measurement, the cryostat was evacuated to the pressure of 5×10^{-6} mbar with the help of pumping unit comprising of diffusion pump and rotary pump. For measuring at different

temperatures, a PID controller unit was used to stabilize the temperature at the desired values (figure 2.6).
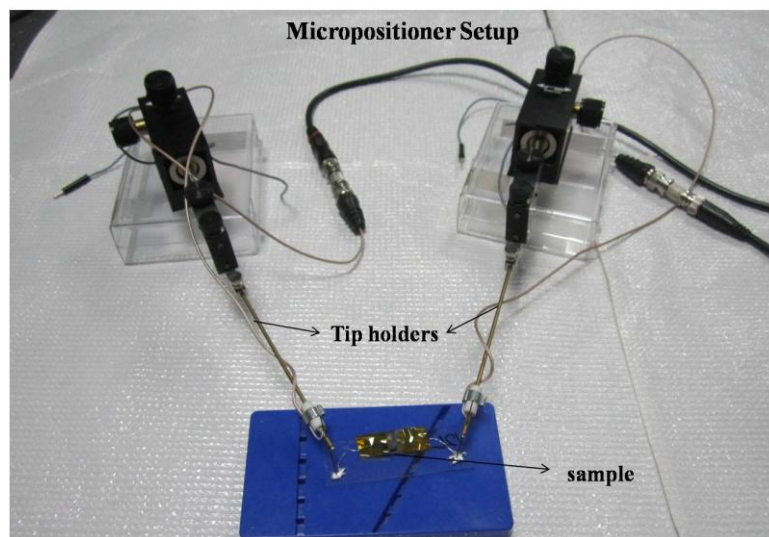
Figure 2.5: Experimental setup used for Room temperature I-V characterization of ZnO NRs grown on ITO substrate.

Figure 2.6: Experiment setup used for low temperature electrical transport measurement of ZnO NRs grown on ITO substrates

2.3. RESULTS AND DISCUSSION
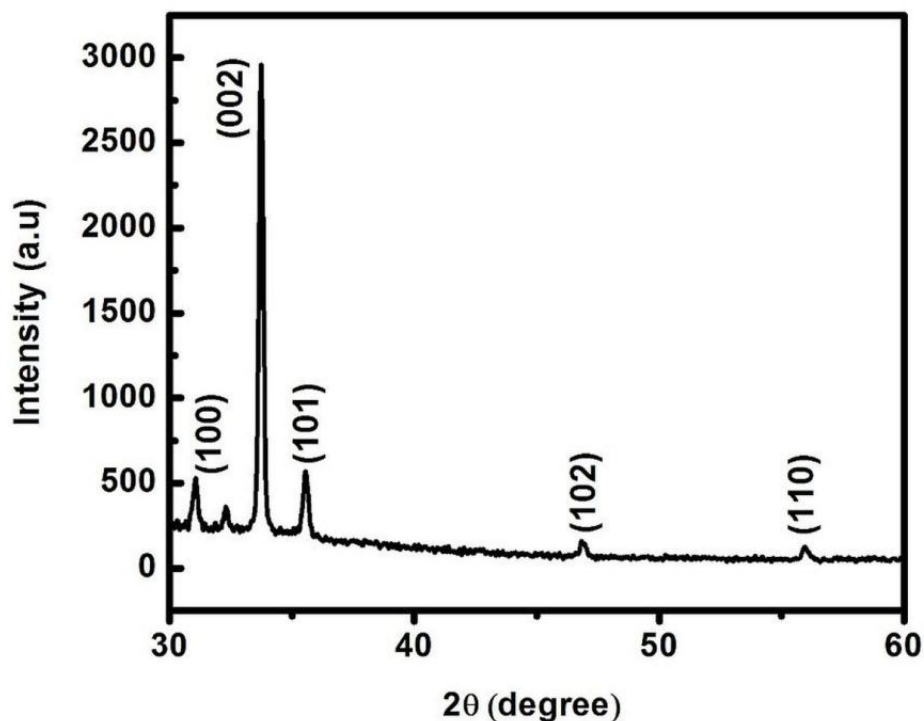
Figure 2.7: XRD pattern of vertically aligned ZnO NRs grown on ITO substrate

Figure 2.7 shows the XRD pattern of ZnO nanorods grown on seeded ITO substrates. Four prominent peaks corresponding to planes: (100), (002), (101), (102) and (110) appear at 2θ = 31.0°, 33.7°, 35.5°, 46.8° and 55.9° respectively. The strong diffraction peak for (002) indicates that the ZnO nanorods are highly oriented along the c-axis which confirms that our sample is highly crystallized hexagonal wurtzite type.

Our results (figure 2.8a and 2,8b) clearly indicate that ZnO seed layers are very essential to grow vertically aligned nanorods. This ZnO seed layers acts as a nucleation sites for the formation of nanorods. The orientation of the ZnO NRs array strongly depends on the orientation of ZnO nanoparticles in the seed layered substrate. When the zinc acetate film coated ITO substrates were annealed, large number of ZnO seeds or particles will be formed with (0001) plane parallel to the substrate. Therefore, ZnO NRs are formed during the growth process from these seeds along the direction of c-axis.
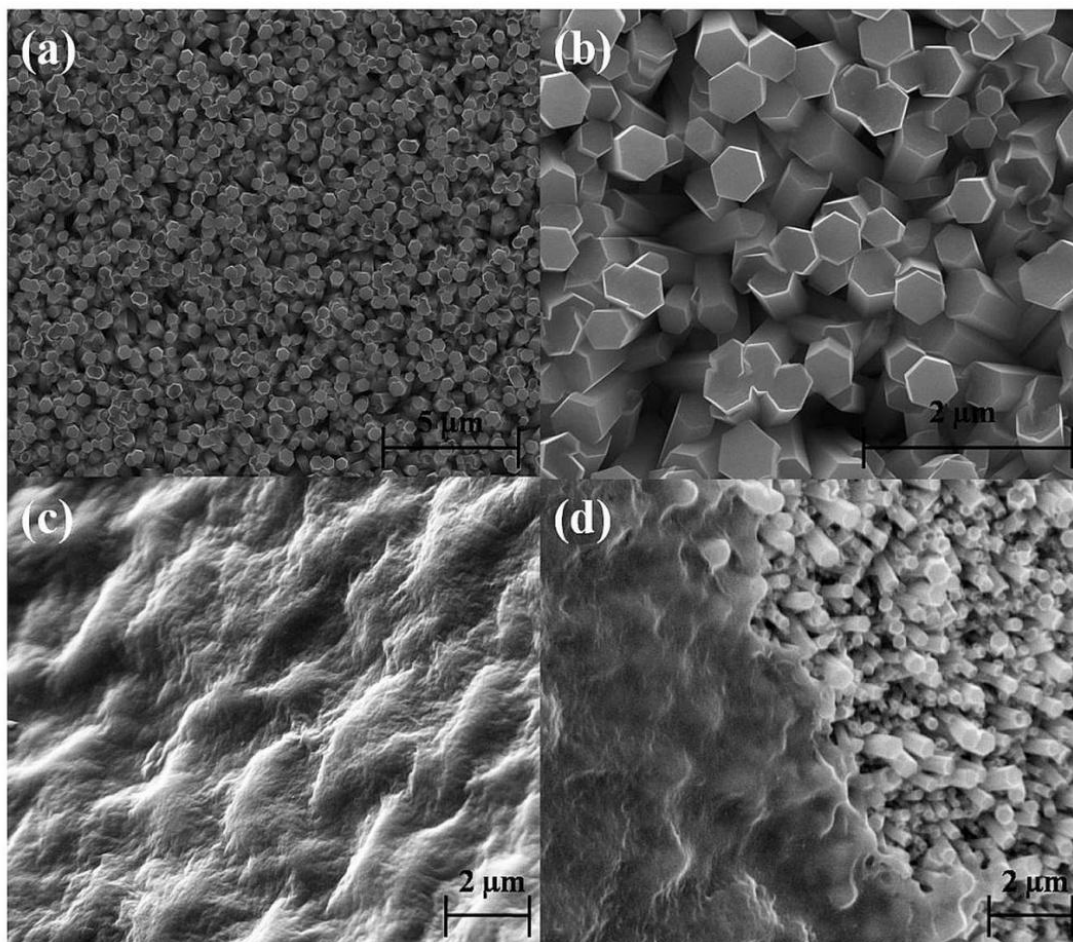
Figure 2.8: (a) and (b) Top view SEM images of as prepared ZnO NRs grown on ITO substrate. (c) Top view SEM images of RGO thin film drop casted on ZnO NRs. (d) SEM images of RGO-ZnO NRs heterostructure at a tilt angle of 50°.

$Zn(OH)_2$ has been proposed as likely precursor species in the hydrothermal growth of ZnO crystals. During the growth process, the following chemical reaction is considered to be responsible for the formation of ZnO NRs,

Decomposition reaction:

$$(CH_2)_6 N_4 + 6\,H_2O \rightarrow 6HCHO + 4NH_3 \qquad (2.1)$$

Hydroxyl supply reaction:

$$NH_3 + H_2O \Leftrightarrow NH_4^+ + OH^- \qquad (2.2)$$

Super saturation reaction:

$$2OH^- + Zn^{+2} \rightarrow Zn\,(OH)_2 \qquad\qquad (2.3)$$
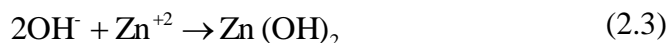
ZnO Nanowires growth reactions:

$$Zn\,(OH)_2 \rightarrow ZnO + H_2O \qquad\qquad (2.4)$$

Generally, ZnO crystal exhibits different growth behavior, depending on the relative growth rates of various crystal facets under hydrothermal conditions. The growth velocities of the ZnO crystal are different along different plane $[0001] > [01\bar{1}\bar{1}] > [01\bar{1}0] > [01\underline{1}1] > [000\bar{1}]$ directions. Furthermore, ZnO has positively charged Zn [0001] surface, which is chemically active, and negatively terminated and chemically inert O [0001] surface which are playing significant role in the growth of ZnO NRs during the hydrothermal process. It is suggested that, during the hydrothermal process, along with inherent crystal properties of ZnO, HMTA (surfactant) play important role in producing nanorods structure. The HMTA, being a non-polar chelating agent would preferentially attach to the non-polar facets of the nanorods, thereby exposing only the (002) plane for the epitaxial growth. Thus preferential growth along the [0001] direction occurs.

To confirm the successful reduction of drop casted GO over ZnO NRs, we have performed Raman measurement on the GO film. GO drop casted on Si substrate was taken as a control sample. Both the samples were thermally annealed at 60° C before taking the Raman spectra. The GO deposited over ZnO nanorods shows higher disorder (D) band intensity (I_D=358 3.03) at 1351 cm^{-1} than the Graphitic (G) band (I_G=3290.80) at 1596 cm^{-1}. The ratio between the intensities (I_D=1750)/I_G=1753.31) was found to be 1.08. In GO deposited over Silicon I_D/I_G was around 0.99 (figure 2.9). The higher value of I_D/I_G in GO on top of ZnO NRs indicates successful conversion of GO to RGO as the newly formed graphitic domains and defects during the reduction process increases the intensity of the D band [153]. From the SEM image (figure 2.8c), it can be observed that the drop casted GO thin films makes a wavy like structure on the top surface of ZnO nanorods without any visible holes and defects in it. From the image (figure 2.8d), it is clear that GO solution due to its planar structure did not percolate between the nanorods and forms a blanket like structure over the nanorods.
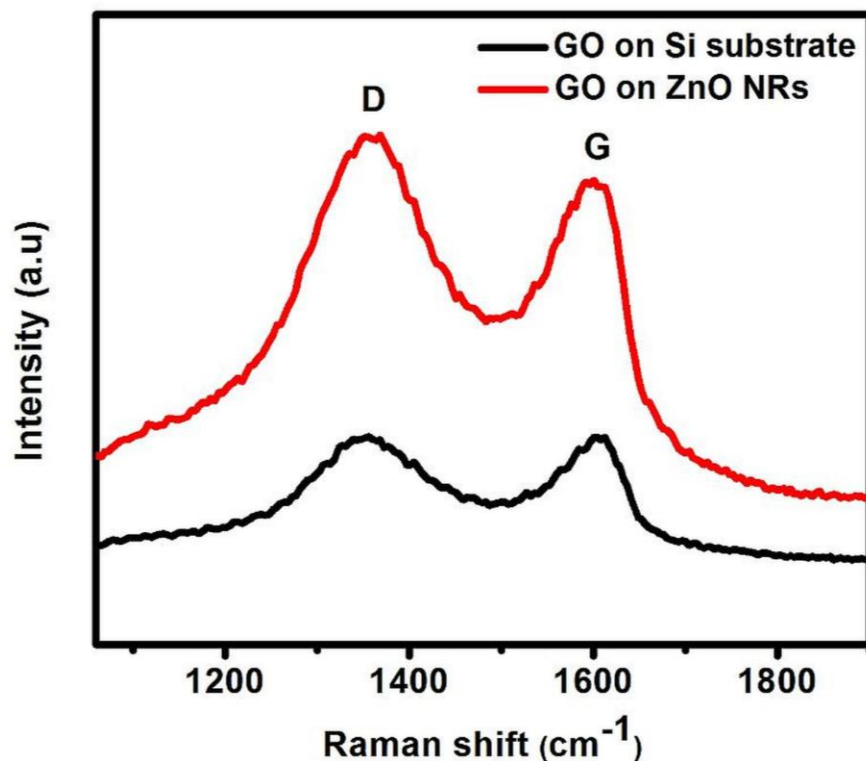
Figure 2.9: Raman spectra of GO drop casted on ZnO NRs and Si substrate followed by annealing at 60°C.

Figure 2.10a and 2.10b shows the I-V characteristics of ZnO NRs with and without RGO deposition. From the figure it is clear that there is almost two orders of magnitude change in resistance for devices with [~1 Kilo ohms] and without RGO [~50 ohms]. The extremely low resistance in samples without RGO layer indicates that there is a direct conducting path (short circuiting) between metal electrode and bottom ITO substrate. With RGO, this short circuiting is inhibited which allow us to probe the electrical characteristics of ZnO nanorods. Moreover, the observed resistivity ($\sim 10^{-5}$ohm cm) is consistent with the resistivity of ZnO considering the diameter and length of the ZnO NRs is ~300 nm and 2 μm respectively.

Generally, GO requires higher heating temperature to transform into partially reduced RGO which are many folds greater than the temperature used in this study [154]. By extending the knowledge of optically induced electron reduction, it is possible that the reduction of GO occurs by thermally generated electrons activated from the zinc related interstitial sites (Zn_I) which is usually prevalent at (0001) face of as grown ZnO nanorods [155-159]. The sample

49

temperature of 60°C which is comparable to activation energy of Zn_I, falls in the range of ~ 30 meV, is sufficient enough to activate enough electrons from the traps to convert GO into RGO which act as a facilitator for improved electrical contacts [160, 161]. Figure 2.11 represents the schematic diagram for in-situ reduction of GO into RGO over the (0001) face ZnO NRs.
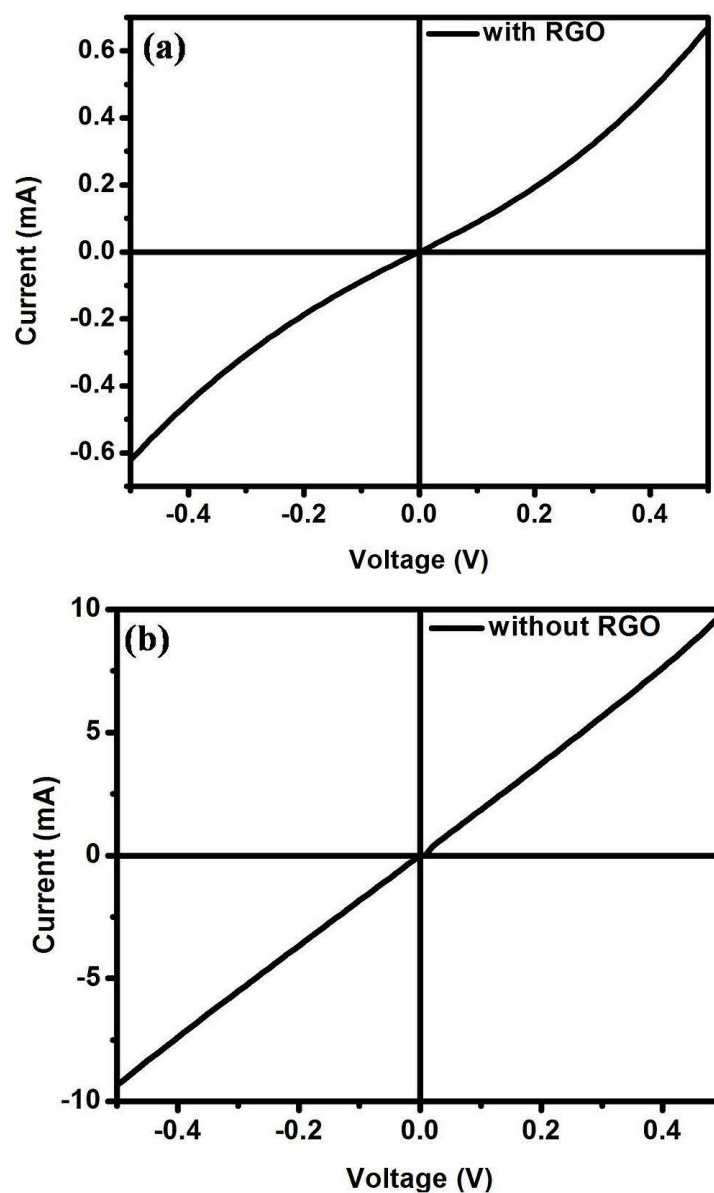
Figure 2.10: Room temperature I-V characteristics of ZnO NRs (a) with RGO and (b) without RGO.
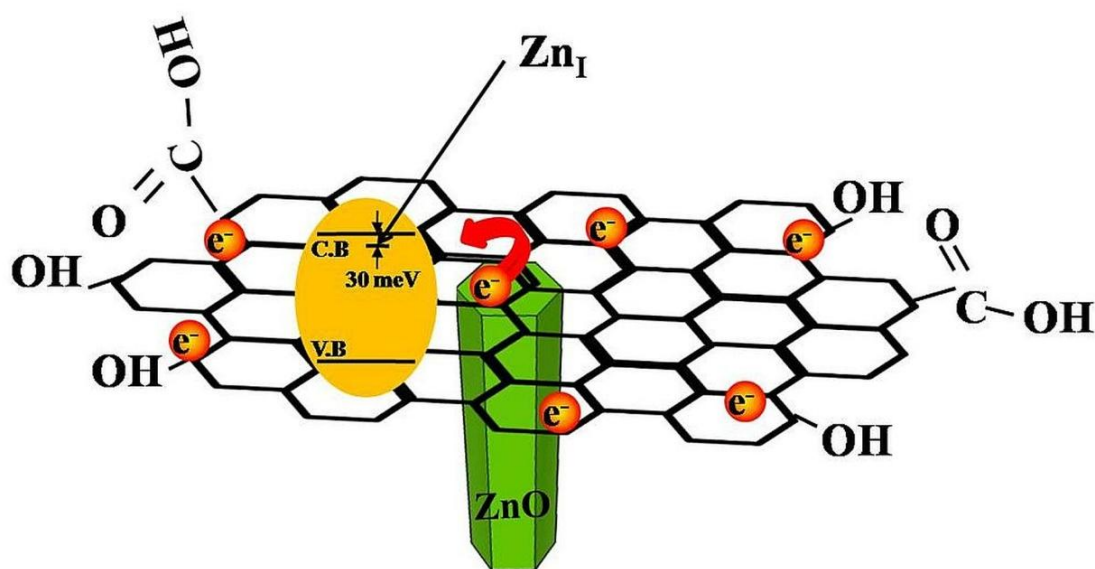
Figure 2.11: Schematic diagram of thermal reduction of GO into RGO on top surface of ZnO NRs at 60°C.
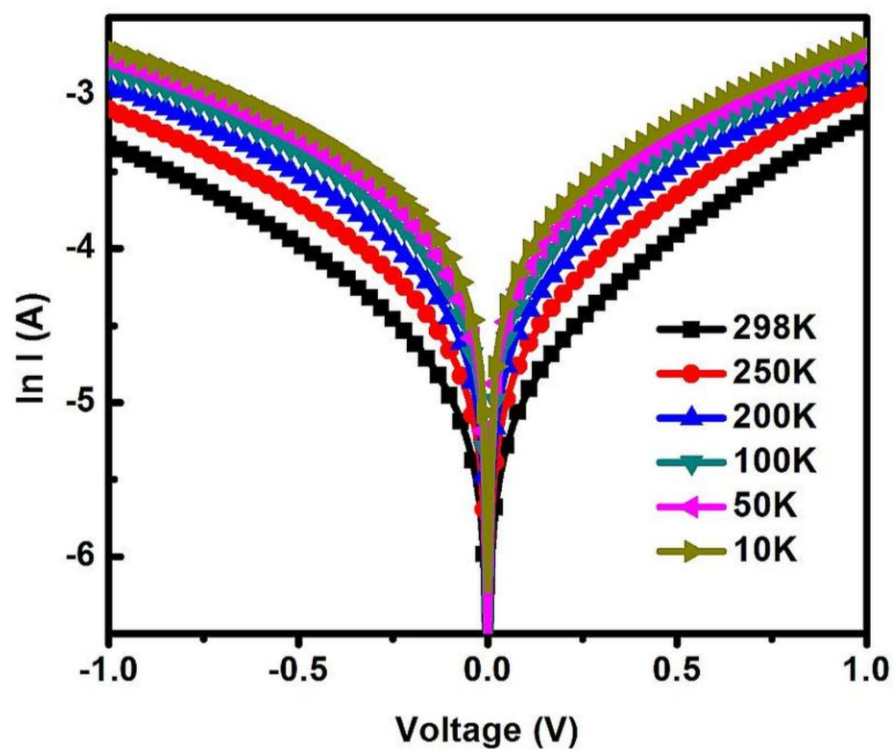
Figure 2.12: Temperature dependent (10 K – 298 K) semilog I-V characteristics of RGO-ZnO NRs heterostructure.

Figure 2.12 depicts the I-V (log (I) vs V) characteristics of RGO-ZnO NRs heterostructure at various temperatures ranging from 10 K to 298 K. The voltage-current plot of as prepared sample indicates that Au/RGO-ZnO heterostructure follows ohmic like behavior. The observed electrical characteristics can be interpreted by considering the carrier transport at the RGO-ZnO NRs interface. At the junction, carrier injection occur either (1) by the thermal activation of electrons over the schottky barrier (SB) or (2) as a result of quantum mechanical tunneling of carriers across the barrier. Generally, these transport mechanisms have different degree of sensitivity to temperature [162]. As discussed in chapter 1, in the high temperature region, phonon assisted injection is more dominant and at low temperatures, carriers are injected across the barrier by either direct or Fowler-Nordheim (F-N) tunneling.

Here, we use direct and F-N tunneling equations (2.5) and (2.7) and mathematically test the linearity of our experimental data using the equations (2.6) and (2.8) for easy comparison [163-165].

2.3.1. Direct Tunneling

$$ \text{I} \, \alpha \, \exp\left[-\frac{4\pi d \sqrt{2m^* \phi_{\text{B}}}}{h} \right] \tag{2.5} $$

$$ \ln\left(\frac{\text{I}}{\text{V}^2} \right) \alpha \ln\left(\frac{\text{I}}{\text{V}} \right) - \frac{4\pi d \sqrt{2m^* \phi_B}}{h} \tag{2.6} $$

2.3.2. Fowler-Nordheim Tunneling

$$ \text{I} \, \alpha \, \text{V}^2 \, \exp\left[-\frac{8\pi d \sqrt{2m^* \phi_B{}^3}}{3hq\text{V}} \right] \tag{2.7} $$

$$ \ln\left(\frac{\text{I}}{\text{V}^2} \right) \alpha - \frac{1}{\text{V}} \left(\frac{8\pi d \sqrt{2m^* \phi_B{}^3}}{2hq} \right) \tag{2.8} $$
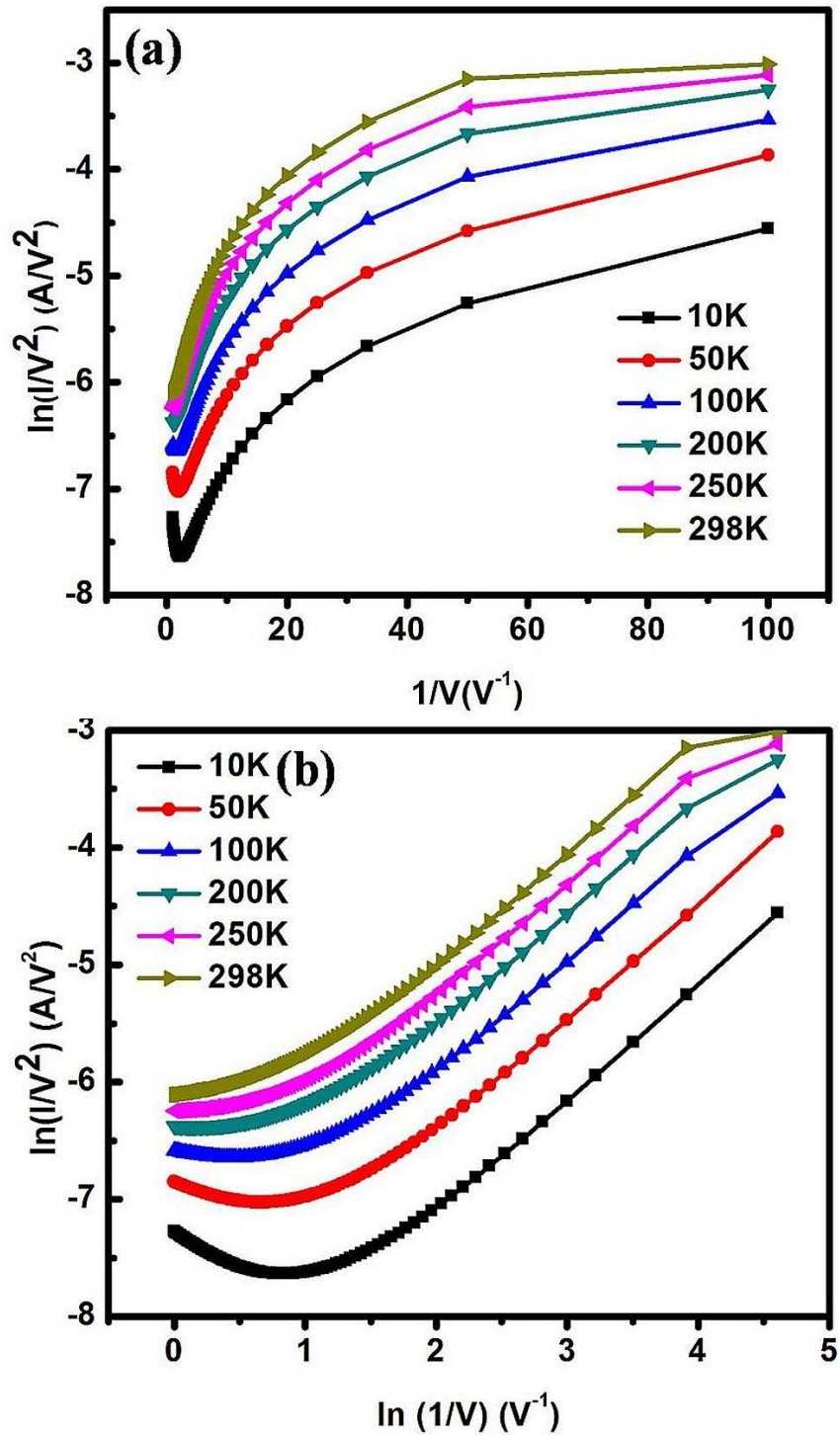
Figure 2.13: (a) ln (I/V^2) plotted vs. the inverse of bias voltage $(1/V)$. (b) ln (I/V^2) plotted vs. logarithmic of inverse of applied voltage ln $(1/V)$.

Here ϕ_B is the barrier height, m^* is the effective mass of the electrons in ZnO, q is the electron charge, h is plank's constant and d is width of the barrier. Equation (2.6) and (2.8) imply that direct and F-N tunneling differ in terms of I-V dependency. Therefore, if the plot for ln $(1/V^2)$ vs $1/V$ shows linearity, then F-N tunneling is expected to occur, whereas for direct tunneling the slope has a quadratic dependence. In figure 2.13a one can observe a clear crossover from F-N (linear regime) to direct tunneling at temperatures below 100 K on decreasing the applied voltage. The crossover is not observable at T > 100 K due to phonon assisted carrier injection (figure 2.13b). This observation is consistent with the theory that F-N tunneling current is dominant mainly in the low temperature regime [166]. The direct tunneling and the F-N tunneling are determined by nature of the interfacial barrier. The former occurs when the barrier is trapezoidal (wide) and the later occurs when the barrier is triangular (thin). The shape, width and height of the schottky barrier at the RGO-ZnO NRs interface are mainly modulated by the applied bias, affecting the carrier injection behavior. At low bias, the most probable mechanism of carrier transport is direct tunneling as the carriers have to overcome wide barrier whereas at high bias carriers experience a very thin triangular barrier that favors F-N tunneling (figure 2.14a and 2.14b). At 10 K, this cross over occurs at ~ 0.47 V (2.12 V^{-1}), and it is worth noting that as the temperature decreases from 100 K to 10 K, the signature of F-N tunneling (crossover point) becomes more visible, clearly demarcating the two different tunneling regimes.
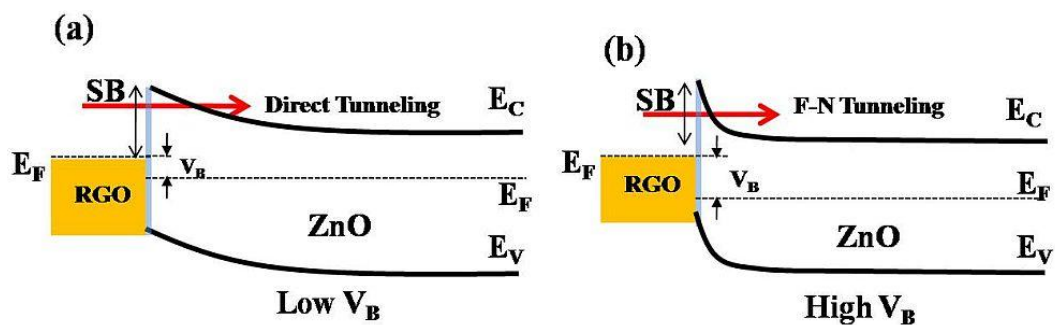
Figure 2.14: Schematic diagram of band alignment at RGO-ZnO NRs heterostrcutre interface at low temperature (T < 100 K) under (a) Low bias (b) High bias.

The improved contact performance at low temperature can be attributed to the reduction

in the density of surface states by the RGO layer as it prevents direct chemical bonding between the metal and ZnO. This will unpin the Fermi level and promotes dynamic changes in barrier height with the externally applied bias. Therefore, when RGO is drop casted on the ZnO NRs a better ohmicity is expected which explains the observed linear electrical behavior.

The inset of figure 2.15 shows the variation of resistance as a function of temperature for Au/RGO-ZnO heterojunction. The resistance changes only by a factor of 6, when the temperature was decreased from 298 K to 10 K. This clearly indicates that there exist shallow traps in ZnO from which electrons are still getting activated even at low temperature. The evaluation of temperature dependent I-V characteristics allows an analysis of the thermal activation energy of free charge carriers. First, we will introduce the equation for finding the activation energies and then we will use it to further analyze the I-V characteristics of ZnO NRs.

The probability of energy state E occupied by an electron as a function of temperature T is given by Fermi distribution function $f_0(E)$,

$$f_0(E) = \frac{1}{\exp\left(\dfrac{E - E_F}{k_B T}\right) + 1} \tag{2.9}$$

where E_F is the Fermi energy and k_B is the Boltzman constant. The density of electrons (n) available between the energy range E and $E + dE$ can be given by.

$$n = \int_{E_C}^{\infty} f_0(E)\, g(E)\, dE \tag{2.10}$$

where $g(E)\, dE$ is density of states available between the energy range E and $E + dE$ and $g(E)$ is given as

$$g(E) = \frac{4\pi(2m^*)^{\frac{3}{2}}}{h^3} \sqrt{E - E_C} \tag{2.11}$$

Here, m^* is the effective mass of the carrier charge and h is Planck's constant.

Using 2.11 in equation 2.10 the density of electrons (n) can be written as,

$$n = \frac{4\pi (2m^*)^{\frac{3}{2}}}{h^3} \int_0^\infty f_0(E) \times \sqrt{E - E_0} \, dE \qquad (2.12)$$

By using Fermi integral $F_{1/2}$ the above equation can be rewritten as,

$$n = 2 \left(\frac{2\pi n^* k_B T}{h^2} \right)^{\frac{3}{2}} \frac{2}{\sqrt{\pi}} F_{1/2} \left(\frac{E_F - E_C}{k_B T} \right) \qquad (2.13)$$

$$F_{1/2}(x_f) = \int_0^\infty \frac{x^{\frac{1}{2}} dx}{1 + \exp(x - x_f)} \qquad (2.14)$$

Using Boltzman approximation i.e. $E_V < E_F < E_C$ and $E_C\text{-}E_F > 3k_BT$,

$$n = 2 \left(\frac{2\pi n^* k_B T}{h^2} \right)^{\frac{3}{2}} \exp \left(-\frac{E_C - E_F}{k_B T} \right) \qquad (2.15)$$

According to the above equation the density of free carriers depends on the temperature and the activation energy E_A which is defined as the difference between the energy of conduction band minimum E_C and Fermi energy E_F. The resulting resistance can be written as:

$$R(T) \, \alpha \exp \left(-\frac{E_C - E_F}{k_B T} \right) \alpha \exp \left(-\frac{E_a}{k_B T} \right) \qquad (2.16)$$

$$R(T) = R_0 \exp \left(-\frac{E_a}{k_B T} \right) \qquad (2.17)$$

Therefore, the activation energy E_A can be obtained by plotting a $\ln \left(\frac{R}{R_0} \right)$ vs T^{-1}. The slope of a linear fit to the values directly reveals the activation energy E_A over k_B. Using the equation 2.17, we have calculated the activation energies of the shallow traps. The calculated activation energies of traps in the low temperature regime [region III] is $E_3 = 0.060 \pm 0.007$ meV which is comparable with previously reported values [166-169]. The calculated activation energies are attributed to shallow donor state of "Zn" interstitials which plays significant role in

the intrinsic n-type electrical conductivity of ZnO nanorods. In the high temperature regime [regime I ≥ 120 K], the resistance falls very rapidly as electrons are activated not only from shallow traps but also from deep levels. The activation energy for region I was found to be around $\Delta E_1 = 14 \pm 1$ meV. In the intermediate temperature regime (120 K ≤ regime II ≥ 50 K) the resistance drops linearly with temperature and the activation energy is around $\Delta E_2 = 4.4 \pm 0.1$ meV. In all the three regimes (figure 2.15), the ln (R) versus T^{-1} was best fit to a straight line which emphasizes temperature dependent transport [170-171]. This confirms that there are defect levels in ZnO NRs with different activation energies which are contributing to the observed electrical property of ZnO NRs.
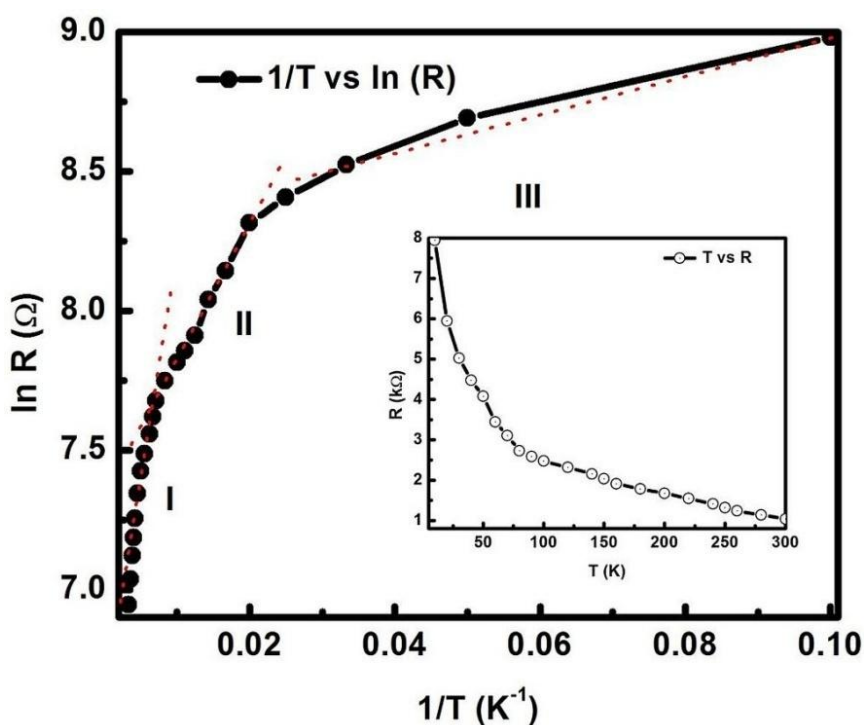
Figure 2.15: ln (R) plotted vs 1/T. Inset shows change in resistance of ZnO NRs at various temperatures.

In summary, ZnO NRs growth conditions were optimized. The effect of reduced graphene oxide (RGO) thin film on the transport characteristics of ZnO NRs was studied. The observed electrical transport characteristics were explained using appropriate conduction mechanism.

CHAPTER THREE

HIGHLY ORDERED COPPER OXIDE (Cu₂O) NANOPILLAR ARRAYS USING TEMPLATE ASSISTED ELECTRODEPOSITION TECHNIQUE AND THEIR TEMPERATURE DEPENDENT ELECTRICAL CHARACTERISTICS

3.1. INTRODUCTION

One dimensional (1D) Cu_2O nanostructures have attracted immense attention in various optoelectronics and sensing device applications due to its unique physical and chemical properties. However, for any practical device applications, it is necessary to grow vertically aligned free standing Cu_2O nanopillars on electrically conductive platforms [172-177]. In this research work, we have grown Cu_2O nanopillars using AAO template assisted electrodeposition technique.

However, the main challenge in obtaining free standing Cu_2O nanopillars using AAO assisted electrodeposition is the removal of template after deposition [178-183]. The usual procedure to remove AAO membrane is by treating it with alkaline solution such as sodium hydroxide (NaOH) [195]. Depending on the material that is deposited inside the AAO pores, the etching rate of the template for a given concentration of NaOH will be different. If suitable etching recipe (etchant concentration and etching time) is not used then it will lead to either under etching or over etching of the membrane. Under etching leaves template debris on the nanostructure and over etching creates localized surface damages which results in either aggregation or total collapse of the 1D nanostructure [196]. This will also adversely affect the electron transport properties of nanopillars which limit their use in optoelectronic, gas and bio-molecule sensing applications [186, 187]. Therefore the etching recipe should be customized according to the deposited material. Though, in the recent past, there are few studies in obtaining vertically aligned 1D Cu_2O nanostructures by removing the AAO template, there is no detailed procedure or protocol describing how the etching parameters are chosen to obtain template free vertically aligned Cu_2O nanopillars. In this work, we have demonstrated a step by step procedure for the removal of AAO template by NaOH solution and identified the most

reliable recipe for obtaining free standing Cu_2O nanopillars. On the whole, this work provides the general approach towards the realization of complete removal of AAO template to obtain free standing Cu_2O nanopillars which can also be extended to other 1D materials. In addition, we also probed the quality of the nanopillars obtained using this technique by investigating their electronic defect states by carrying out temperature dependent current-voltage measurements.

3.2. MATERIALS AND METHODS

3.2.1. Preparation of Electrolyte Solution

The electrolyte solution used for the deposition was prepared by mixing 1.498 g $CuSO_4.5H_2O$ in 15 ml of DI water followed by magnetic stirring for 15 min. After stirring, the above solution was added to 15 ml of lactic acid aqueous solution. The pH value of the resultant solution was adjusted to 9 by adding 4 M NaOH solution. 50 ml of the as prepared electrolyte solution was used for the deposition of Cu_2O [188].

3.2.2. Electrodeposition of Cu_2O Nanopillars

Copper oxide (Cu_2O) nanopillars were fabricated by template directed electrodeposition technique. First, basic information related to electrodeposition technique is provided followed by detailed procedure used for the growth of Cu_2O.

3.2.3. Electrodeposition

Electrodeposition (better called as an "art") is as old as the electricity. Electrochemical deposition is also known as electrodeposition which involves oriented diffusion of charged reactive species through a solution in the presence of external electric field and reduction of the charged growth species at the desired template (which also acts as an electrode). The very success of electrodeposition lies in the fact that it can be scaled up for industrial applications ranging from electronics, micro-macro, and optoelectronics to automobile industry. The first quantitative formulation of electrodeposition was done by Michael Faraday, popularly known as Faraday's laws of electrodeposition which gives an estimate of the amount of material *(W)* deposited in terms of the product of electrochemical equivalent $\left(\dfrac{E}{F}\right)$ and the charge passing through the electrolyte [189, 190],

$$W = \left(\frac{E}{F}\right)It \qquad (3.1)$$

where E is equivalent weight and I and t are current and time respectively with F = 96485 Coulomb/mol. Here this formulation assumes the complete reduction of ions by the charged passed between the electrodes. Practically the efficiency of the process is much less than the theoretically expected value due to factors like joule heating and material deposition at the electrode. Generally, this method is only applicable to electrically conductive materials such as metals, alloys, semiconductors, and conductive polymers. After the initial deposition, the electrode is separated from the depositing solution by the electrodeposited material and so the as deposited material must conduct in order for the deposition process to continue. Naturally, the electrodeposits follow the shape of the electrode used. The feature that the electrodeposits can take shapes of objects (electrode) in a controlled way makes electrodeposition a unique technique for synthesis of materials at nanoscale. When the deposition is confined to the nano pores of template membranes, nanowires/nanotubes arrays are produced.

Electrochemical deposition can be carried out in two different ways according to the number of electrodes used in the electrochemical cells. The simplest form of an electrochemical cell is 2-electrode system, consisting of a cathode and an anode (figure 3.1a). In the 2-electrode system, the voltage is measured between these two electrodes, and the current is measured anywhere in the circuit. This system works very well under equilibrium conditions.
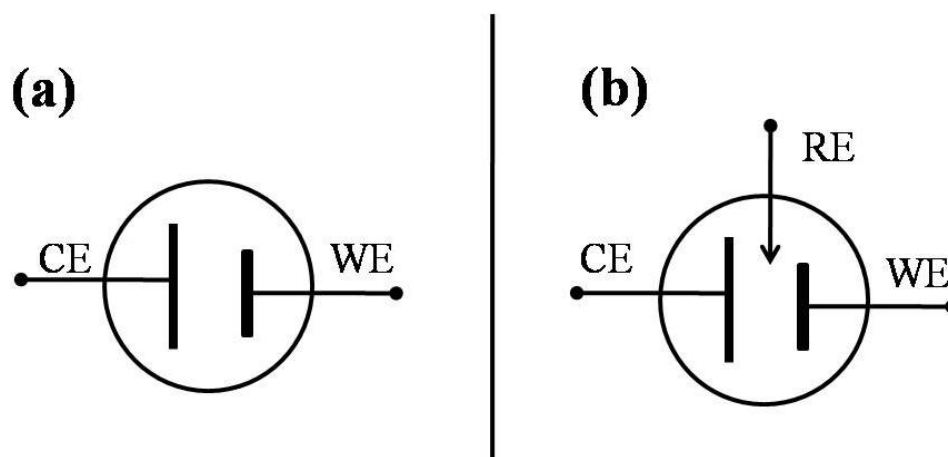
Figure 3.1: Schematic view of the (a) two electrode setup (b) and three electrode setup.

However, if the electrochemical reactions taking place are not in equilibrium, the voltage measurement will be inaccurate due to redox potentials and over potential. To counter this problem a third electrode is introduced for measuring the voltage on the working electrode versus a known stable reference potential (figure 3.1b). This electrode is called a reference electrode. This three electrode electrochemical technique is the widely used technique for growing nanomaterials [191, 192].
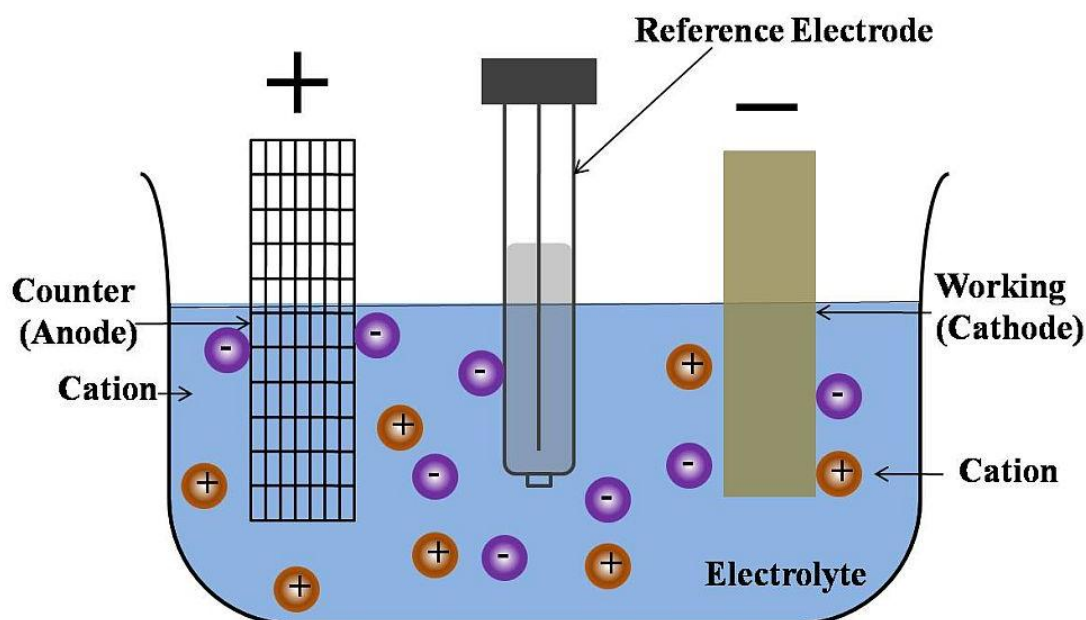
Figure 3.2: Schematic illustration of three electrode based electrochemical cell.

Figure 3.2 shows the schematic representation of electrochemical cell with three electrode configuration, a working electrode (WE), a counter electrode (CE) and a reference electrode (RE) are placed in an electrolyte containing the ions of interest [193, 194].

The substrate over which materials had to be deposited is used as a working electrode. For this purpose the substrate must be always electrically conductive and should not get chemically reacted with the electrolyte solution.

The counter electrode (also known as auxiliary electrode) is an electrode which is used to close the circuit current in the electrochemical cell. It is usually made up of inert materials such as Pt, glassy carbon and Au and do not generally involve in any chemical reactions.

A reference (standard) electrode is an electrode whose electrode potential remains always constant because of the constant activity of the ions. Often used reference electrodes are normal hydrogen electrode (NHE), saturated calomel electrode (SCE) and Ag/AgCl. Compared to using NHE and SCE the AgCl electrode has the advantage of being both environmentally friendly and easy to make [195, 196].

There are two types of electrodeposition techniques which are predominantly used for the deposition of materials namely galvanostatic and potentiostatic deposition.

3.2.4. Galvanostatic Electrodeposition

In the galvanostatic mode, a constant current is maintained between working electrode (WE) and counter electrode (CE) and the potential difference between the WE and RE is measured (*V-t* curve). The most important advantage of using the galvanostatic mode is that the reaction rate can be optimized, since the amount of deposited material is directly related to the current via Faraday's law [197]:

$$W = \frac{ItM}{zF} \tag{3.2}$$

where W is the weight of the deposited material, I is the measured current, t is the passed time, z is the unit-less valence of the deposited atoms, and M is the molecular weight.

3.2.5. Potentiostatic Electrodeposition (Chronoamperometry)

In potentiostatic mode (chronoamperometry), the current is measured versus time as a response to potential pulse applied to the WE. At the beginning of the experiment the potential of the working electrode is held at initial value E_i. At t = 0, the potential is instantaneously changed to a final value E_F, and corresponding current-time (I-t) response is recorded as shown in figure 3.3a and 3.3b. The current at any time due to the step potential can be given by Cortell equation [198],

$$i = \frac{n F A C_0 D_0^{1/2}}{\pi^{1/2} t^{1/2}} \tag{3.3}$$

Where n = the stoichiometric number of electrons involved in the reaction; F = is Faraday's constant (96485 C/equivalent), A = electrode area (cm^2), C_0 = concentration of electro active species, and D_0 = diffusion constant for electro active species.
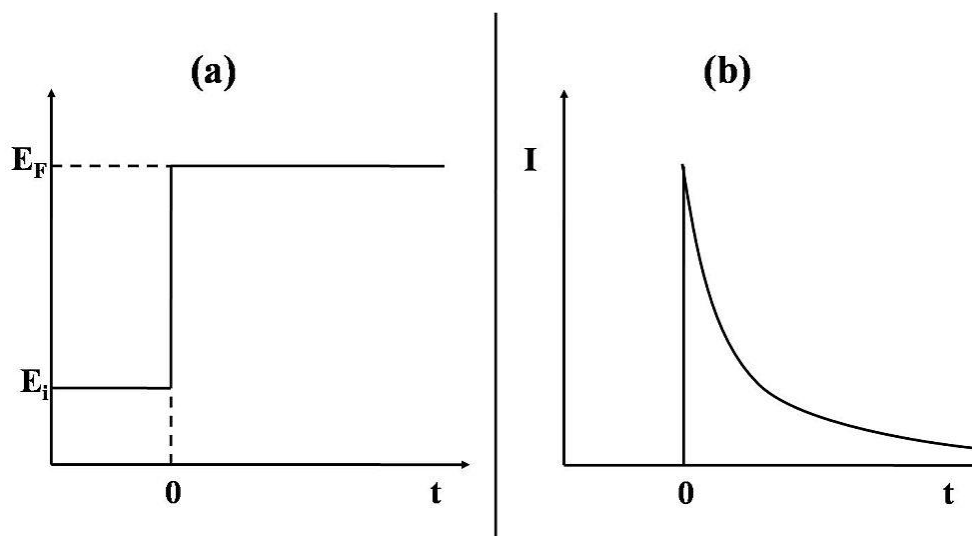
Figure 3.3: The chronoamperometric experiment. (a) Potential-time profile, E_i is the initial value and E_F (final value) is the potential of interest for the deposition of materials. (b) The corresponding current response as a function of time.

The most important advantage of using the potentiostatic mode is that, one can aim for a specific reaction or product because the type of chemical reaction and stoichiometry is strongly dependent on the applied potential. By varying the potential it is possible to control the quality and geometry of deposits such as nanowires or nanotubes. Since the quality of electrodeposits mainly depends upon electrodeposition conditions, it becomes important to determine a particular potential where the rate of deposition is optimum. Any small deviation in the applied potential with respect to the ideal deposition potential will have detrimental effect on the quality of the material. In the preceding section we will discuss about general information regarding the procedure for finding correct electrodeposition potential for growing nanopillars.

3.2.6. Linear Sweep Voltammetry (LSV)

Generally, the electrodeposition potential required for the synthesis of materials is unknown. In this case, linear sweep voltammetry (LSV) measurement technique is employed to identify oxidation or reduction potential. In LSV the current at the working electrode is

measured and the voltage between WE and RE is varied linearly within a fixed range (V_1 and V_2). The oxidation and reduction is registered as a peak or trough in the current signal indicating the potential at which the species begins to reduce or oxidize (figure 3.4a and 3.4b). From this LSV curve the electrodeposition potential is deduced which is then used as the deposition potential for growing nanorods using chronoamperometric technique [199].
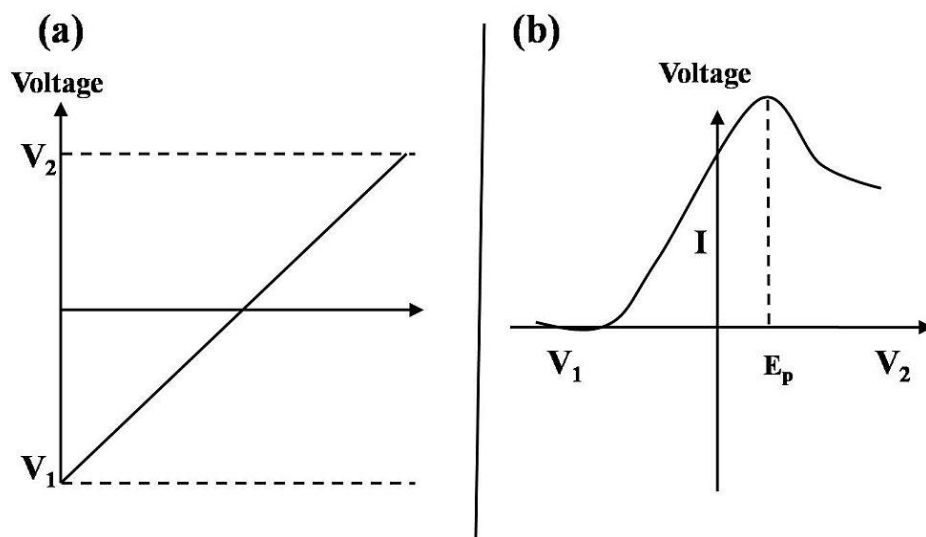
Figure 3.4: Linear sweep voltammetry experiment. (a) Plot of voltage applied between WE and RE (between V_1 and V_2) (b) Current-voltage response of the electrolyte and the dotted line indicate the potential at which reduction occurs.

3.2.7. Electronic Block Diagram of the Potentiostat

It uses an electrical feedback loop to control the potential of the working electrode (the electrode at which the reaction of interest occurs) with respect to a reference electrode, even in the presence of ohmic drop. A third electrode, the auxiliary/counter electrode is used to supply the current to the working electrode. Since third electrode eliminates current flow through the reference electrode, the three electrode technique provides more control over the applied potential. A simplified diagram of a potentiostatic circuit is given in figure 3.5.

Most modern electrochemical equipment employs versatile high-input impedance differential amplifiers known as operational amplifiers (OAs) as circuit elements. In the

potentiostat circuit, OA1 provides the auxiliary electrode with the required voltage and current to maintain the desired potential difference between the reference and working electrodes. OA2 is a buffer amplifier (voltage follower) that prevents significant current draw through the reference electrode and creates low input impedance at the reference electrode potential. In operation, the amplifier OA1 adjusts the current and voltage at the auxiliary electrode to whatever is necessary to minimize the voltage difference at the inputs. The negative feedback loop that exists between the output and input of OA1 includes OA2, the reference and auxiliary electrode, and the solution resistance between reference and auxiliary.
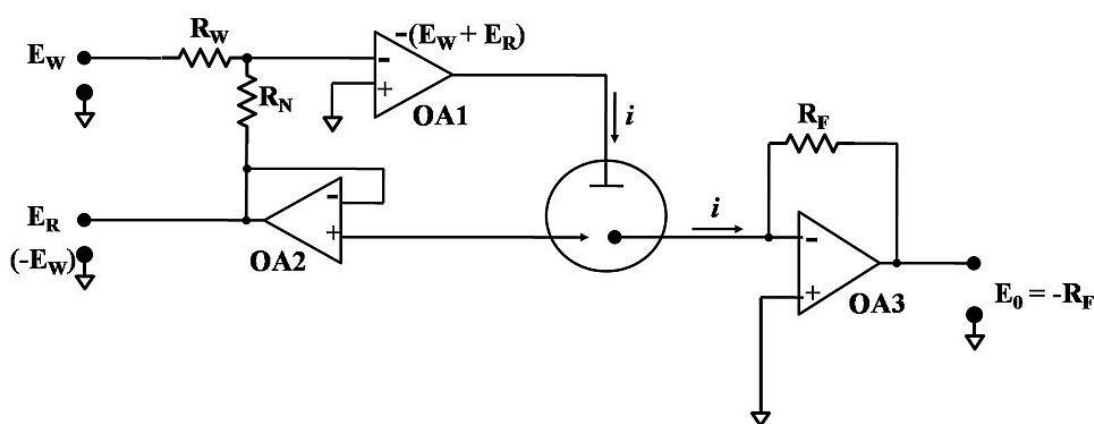
Figure 3.5: Electronic circuit illustration of potentiostat

Thus, the voltage at the auxiliary electrode will be the inverted sum of the reference electrode voltage (E_R), any externally applied voltage (E_W), and the ohmic voltage arising from current flow through the solution resistance. This means that, if the reference electrode is close to the working electrode, the effect of the ohmic drop is minimized and the potential difference between the working electrode and reference electrode is maintained or ''clamped'' close to E_W. Clamping the voltage at E_W is the basis for the name ''voltage clamp''; a term used outside the electrochemical literature as a more descriptive name for the potentiostat circuit. The working electrode is maintained at the circuit common potential in the potentiostat circuit. The current-transducer amplifier, OA3, maintains the electrode potential at common potential and provides a voltage output proportional to the current input. As before, the amplifier uses negative feedback to minimize the potential difference between the inputs by adjusting the output. In the process, the inverting input (-) is set to be virtually the same as the potential of the non-inverting input

(+), and thus the inverting input is at ''virtual ground.'' Note that the output voltage across the feedback resistor, RF, produces a current to oppose the current flowing into the input and changing RF changes the signal gain. Although the above circuit could be used in voltammetric experiments, most potentiostat circuits are considerably more sophisticated. Additional circuitry is added to provide damage protection from excessive signal inputs or outputs, additional current or voltage range (i.e., compliance) at the auxiliary electrode, and for variable gain and filtering of the input current.

As described above, in a typical template assisted potentiostatic electrodeposition, metal coated commercially available porous templates such as AAO and Poly carbonate membranes are used as a working electrode. By finding the suitable deposition potential, nanowires/nanorods are grown inside the pores. Subsequently the free standing 1D metal oxide nanostructures are obtained by removing the template in appropriate etchant (base solution). In this research work using this potentiostatic electrodeposition technique (chronoamperometry) we had grown Cu_2O nanopillars inside the AAO template.

3.2.8. Electrodeposition of Cu_2O Nanopillars
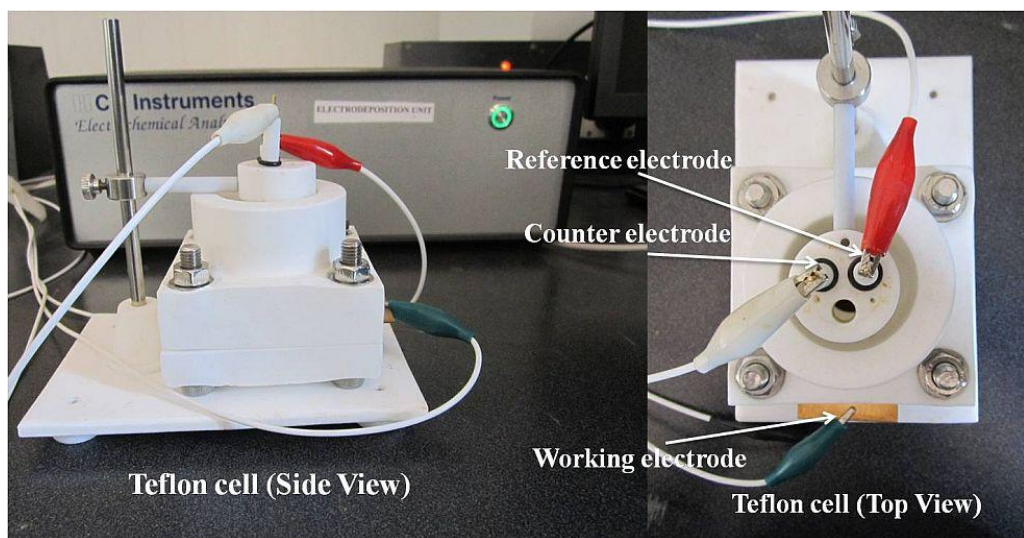
Figure 3.6: Electrodeposition set up used for the growth of Cu_2O nanopillars (a) Side view of Teflon cell (with AAO template) connected to electrochemical analyzer for the deposition (b) top view of the Teflon cell.

Copper oxide (Cu_2O) nanopillars were fabricated by template directed electrodeposition technique using the electrodeposition set up shown in figure 3.6. Commercially available anodized alumina membrane (Whatman) with pore size of 100 nm was used as a template in this study. Firstly, the membrane was thoroughly cleaned in acetone and ethanol by ultrasonication for 10 min followed by washing with copious amount of DI water. Prior to electrodeposition, 500 nm gold thin film was e-beam evaporated on backside of the AAO membrane to create electrically conductive surface. Custom made Teflon cell was used to carry out the entire electrodeposition process. The electrical contact to the working electrode (gold coated AAO template) was made by placing the copper foil underneath it and tightening them together with the help of O ring. The total area exposed to the electrolyte solution was 0.1 cm^2. Figure 3.7 shows the schematic representation of teflon cell and how electrical contacts to AAO template are made for the electrodeposition of Cu_2O nanopillars.
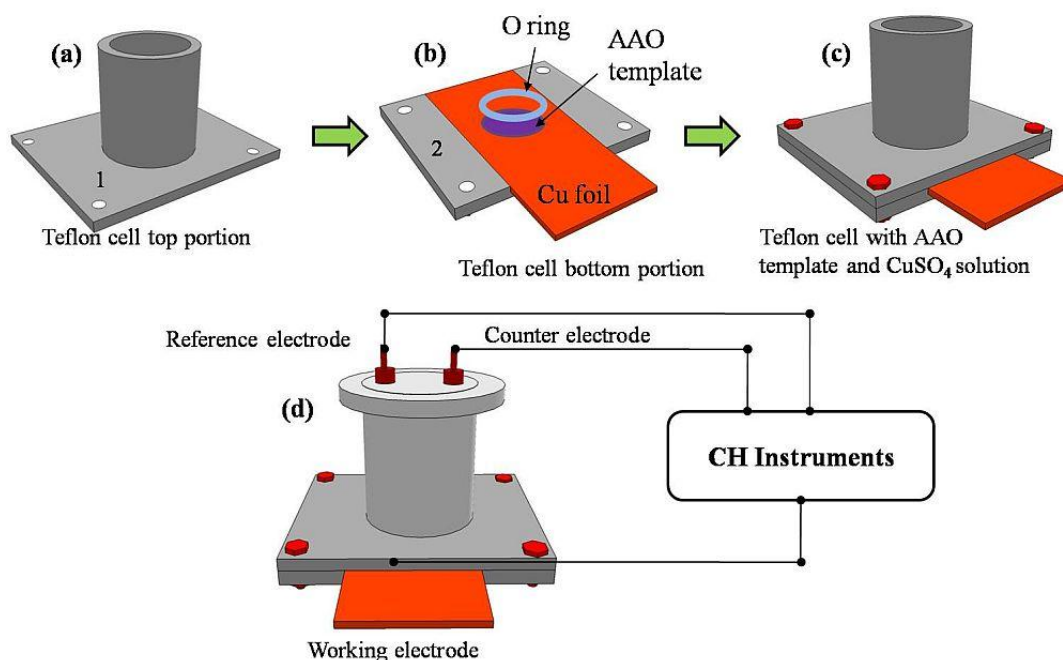
Figure 3.7: Electrodeposition set up used for the growth of Cu_2O nanopillars (a) Top part (solution container) of the teflon cell (b) bottom portion of the teflon cell inserted with copper foil to form a electrical contact with Au coated AAO template (c) Teflon cell fixed with AAO template along with electrolyte solution for electrodeposition (d) Teflon cell with AAO template connected to CH instruments during the electrodeposition process.

3.2.9. Potentiostatic Deposition of Cu_2O Nanopillars
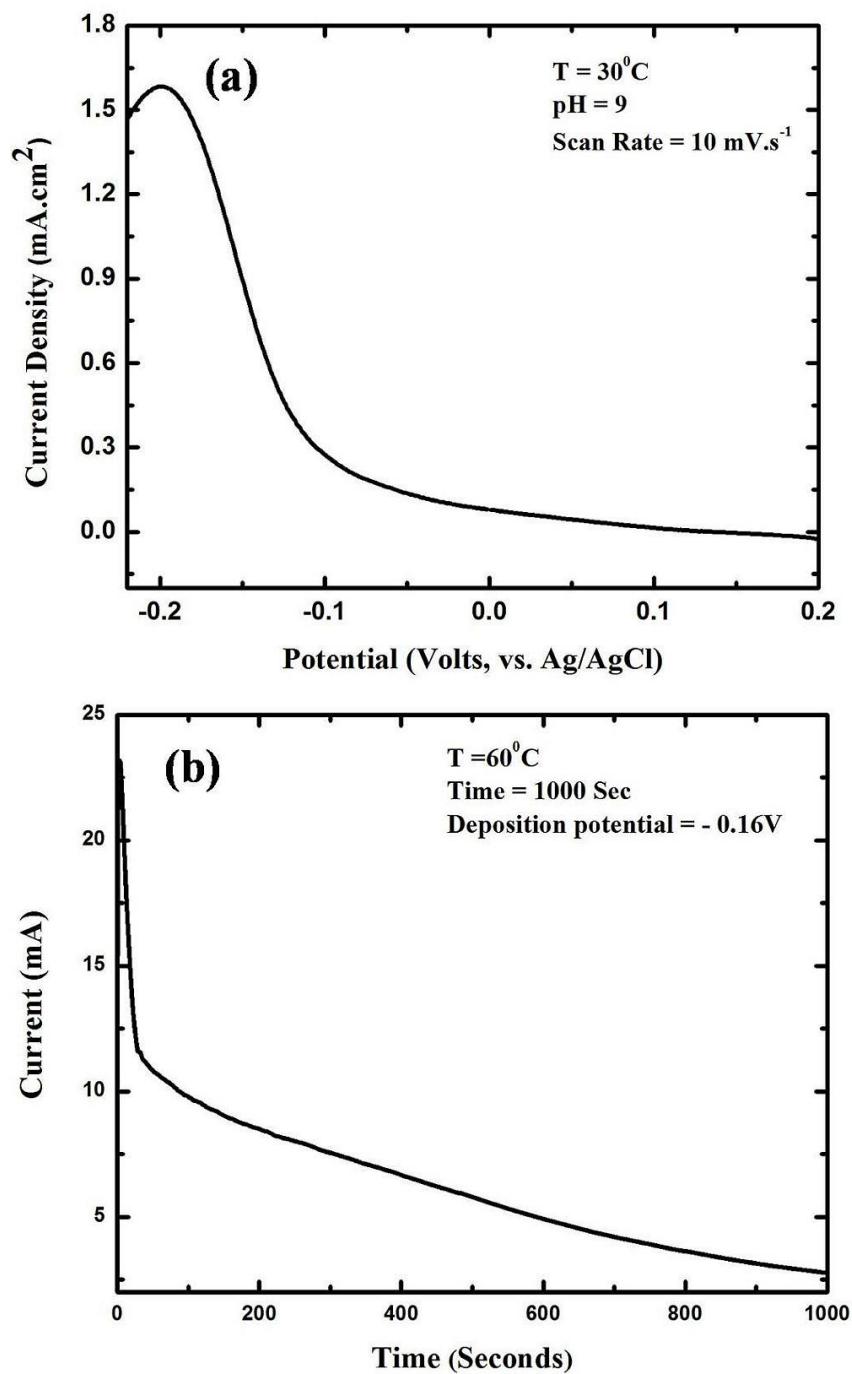
Figure 3.8: Electrodeposition of Cu_2O nanopillars. (a) Linear sweep voltammogram of an aqueous solution of $CuSO_4.5H_2O$. (b) Chronoamperogram (I-t) of Cu_2O nanopillars electrodeposition inside the AAO template at -0.16 V vs. Ag/AgCl reference electrode at 60^0C.

The electrodeposition potential required for the Cu_2O synthesis was determined by LSV technique. Figure 3.8 (a) shows the typical cathodic scan performed between -200 mV to 200 mV at a scan rate of 10 mV.s^{-1}. The peak at -0.199 mV corresponds to the reduction of Cu^{2+} to Cu^+ and the subsequent formation of Cu_2O. Cu_2O nanopillars were deposited inside the AAO membrane at fixed potential of -0.16 V (versus 1M Ag/AgCl reference electrode) for 1000 second using chronoamperometry technique (CH instruments, USA) at 60°C figure 3.8b. After the electrodeposition, free standing vertically aligned Cu_2O nanopillars were obtained by removing the AAO membrane in NaOH solution. It is to be noted that we chose -0.16 V vs. Ag/AgCl as the deposition potential over the higher values to avoid the over reduction which would generally results in damages of nanopillars.

The mechanism for the electrodeposition of Cu_2O inside the AAO template from the alkaline solution of copper lactate (pH~9) maintained at 60^{0}C can be given by [200],

$$2Cu^{2+} + 2e^- \rightarrow 2Cu^+ \tag{3.4}$$

$$2Cu^+ + 2OH^- \rightarrow 2Cu\,(OH) \tag{3.5}$$

$$2Cu\,(OH) \rightarrow Cu_2O + H_2O \tag{3.6}$$

At first, cuprous ions (Cu^+) are formed through the reduction of cupric ion (Cu^{2+}) as given in the equation (3.4). The as formed Cu^+ ions further transforms into copper hydroxide (eq.3.5) which subsequently undergoes dehydration process (eq.3.6) resulting in the deposition of Cu_2O.

3.2.10. Formation of Electrical Contacts on Cu_2O Nanopillars

250 nm gold thin film was e-beam evaporated as a top metal electrode on vertically aligned Cu_2O nanopillars. The e-beam deposition was carried out under a pressure of 3×10^{-6} mbar. Temperature dependent electrical characteristics (180 K -300 K) were carried out in two terminal configurations (figure 3.9d) using closed cycle refrigerator (Janis, USA) and Semiconductor characterization system (Keithley 4200, USA). Figure 3.9(a, b and c) shows the schematic representation of electrodeposition of Cu_2O nanopillars inside the AAO template and device configuration used for the electrical measurements.
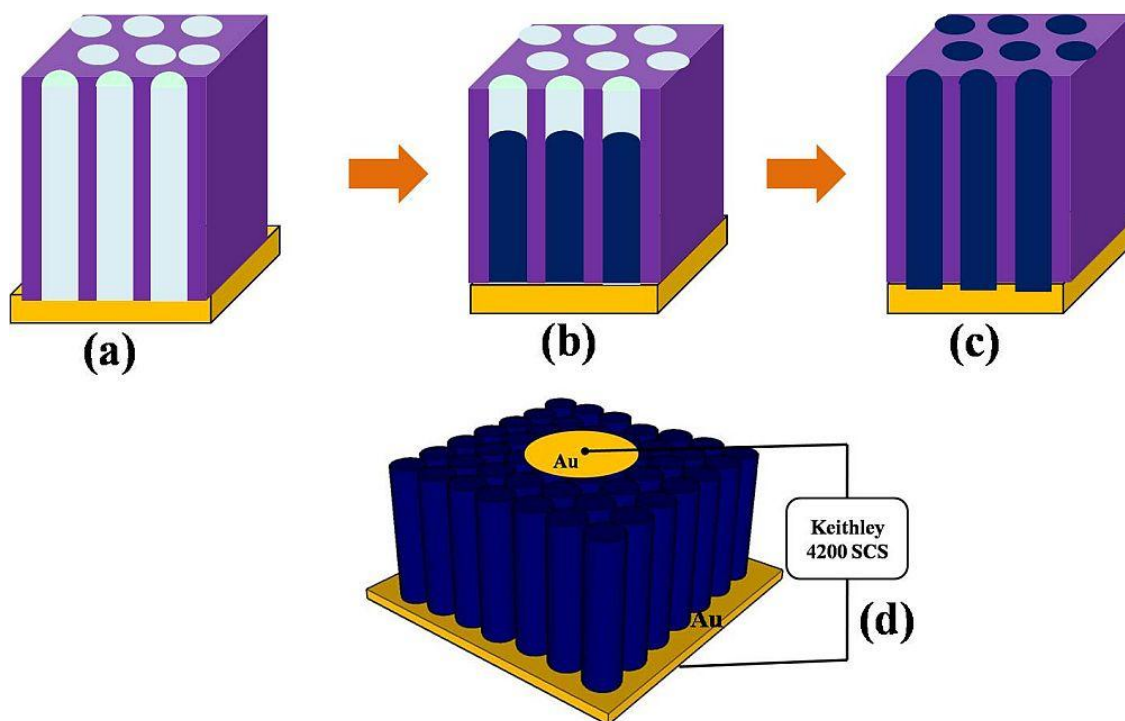
Figure 3.9: Schematic diagram of electrodeposition of Cu_2O nanopillars inside the AAO template (a) bare AAO template with bottom Au coating (b) AAO template with half filled Cu_2O nanopillars (c) AAO template with fully deposited Cu_2O nanopillars (d) Vertically aligned Cu_2O nanopillars after the removal of AAO template connected to Keithley 4200 SCS for electrical characterization**.**

3.3. RESULTS AND DISCUSSIONS

The crystalline structures of the Cu_2O nanopillars were characterized by X-ray diffraction (XRD) measurement after removing the AAO membrane. Figure 3.10 shows the XRD pattern of vertically aligned free standing Cu_2O nanopillars and it confirms that the Cu_2O nanopillars are in cubic phase. The presence of (111) and (200) and (110) planes indicates that electrodeposited Cu_2O nanopillars are polycrystalline in nature. The presence of less intense peak at $2\theta = 47$ may be due to Cu (111) which will generally get co-deposited along with Cu_2O.

After the electrochemical deposition, AAO templates embedded with Cu_2O nanopillars were treated with aqueous NaOH solution to dissolve the AAO template. Template removal step was carried out at different concentrations of NaOH for varying time periods. SEM images of

NaOH treated template were taken to analyze the effectiveness of each etching parameters in removing the AAO template. To begin with, the Cu_2O deposited AAO template was treated with 5M NaOH solution for 1 hour. On inspecting the sample using SEM (figure 3.11a), no trace of AAO template was found. However Cu_2O liberated from the template got entangled with each other and collapsed on the gold support. It was quite obvious that the sample was over-etched and the etchant not only reacted with AAO template but also with Cu_2O nanorods. Therefore to develop a recipe that will etch only the AAO template while maintaining the structural integrity of nanorods, a series of etching trials were performed. A mild etching recipe of 1M NaOH and 8 min etching time was chosen for the second trial. The idea behind choosing very low concentration of NaOH is to slow down the etch rate and a small time period is chosen to determine the smallest sample volume removed by the etchant. Subsequent etching trials were repeated by varying the time of etching and fixing the concentration of NaOH at 1M. Figure 3.11b is the top view SEM image of Cu_2O nanopillars embedded in AAO template treated using the above experimental condition. The image clearly shows that AAO template is still in its original state, which indicate that etchant concentration and reaction time is insufficient.
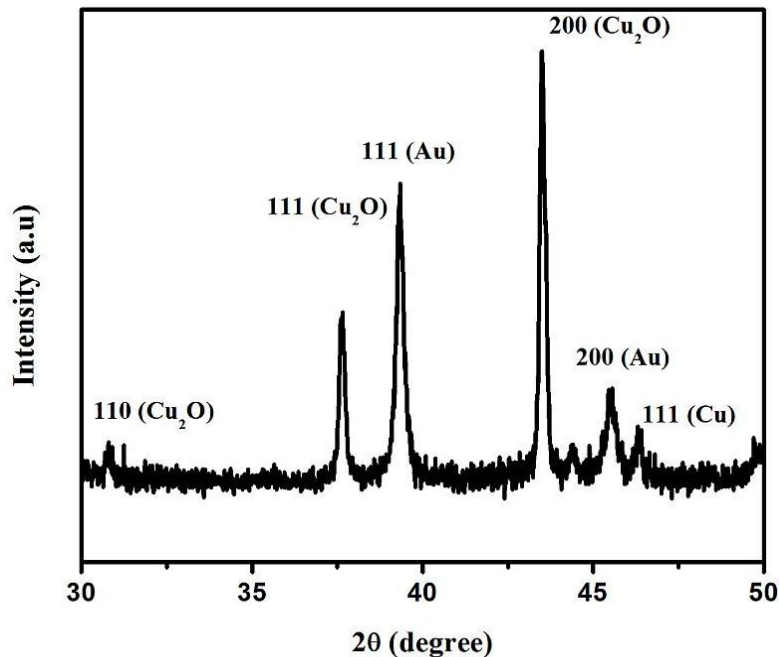
Figure 3.10: XRD pattern of vertically aligned free standing Cu_2O nanopillars after the removal of AAO template on gold thin film.

3.3.1. Removal of AAO Template to Obtain Vertically Aligned Free Standing Cu$_2$O Nanopillars
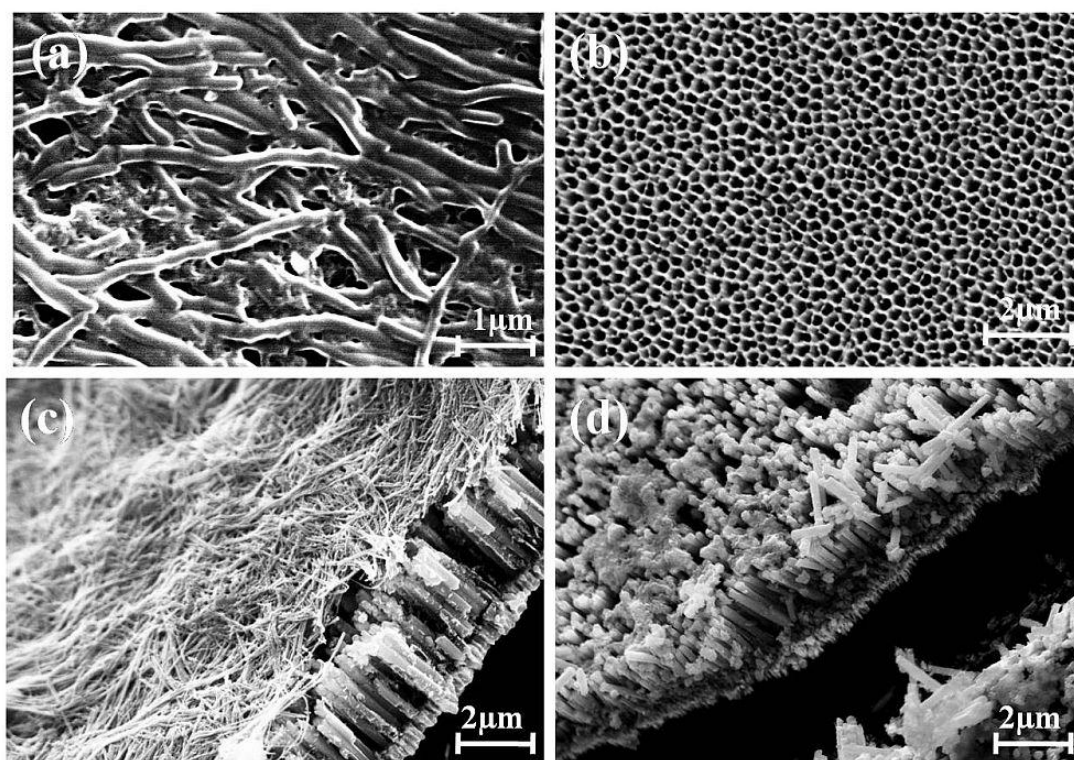
Figure 3.11: SEM images of Cu$_2$O nanopillars embeded in AAO template (a) AAO template dissolved in 5 M NaOH solution for 1 hr (b) 1M NaOH solution for 8 min (c) 1M NaOH solution for 25 min and (d) 1M NaOH solution for 30 min.

For the third trial, the sample soaking time in 1M NaOH was increased from 8 min to 25 min. Figure 3.11c shows the SEM image of Cu$_2$O nanopillars after removing the AAO template using the above parameters. From this image one can clearly see a highly ordered vertically aligned Cu$_2$O nanopillar under a stack of un-dissolved AAO template. This indicates that the etching time is good enough to disintegrate AAO but insufficient to completely dissolve them. Therefore, for the fourth trial, the soaking time period was increased from 25 to 30 min and we were able to achieve vertically aligned freestanding Cu$_2$O nanopillars with traces of AAO membrane (figure 3.11d).

Having established that 30 min soaking time almost removes the AAO template, three more etching trails were carried out in samples prepared under the same experimental condition

at three different etching time periods. The time periods used were 45 min, 50 min and 1hr. It turned out that the sample which has gone through 1 hr etching process resulted in very clean and vertically aligned Cu_2O nanopillars arrays and also exhibited good reproducibility (figure 3.12a - 3.12d). Though the samples which have gone through dissolution time period of 45 and 50 min exhibited well aligned Cu_2O nanopillars, they still had some traces of un-dissolved AAO.
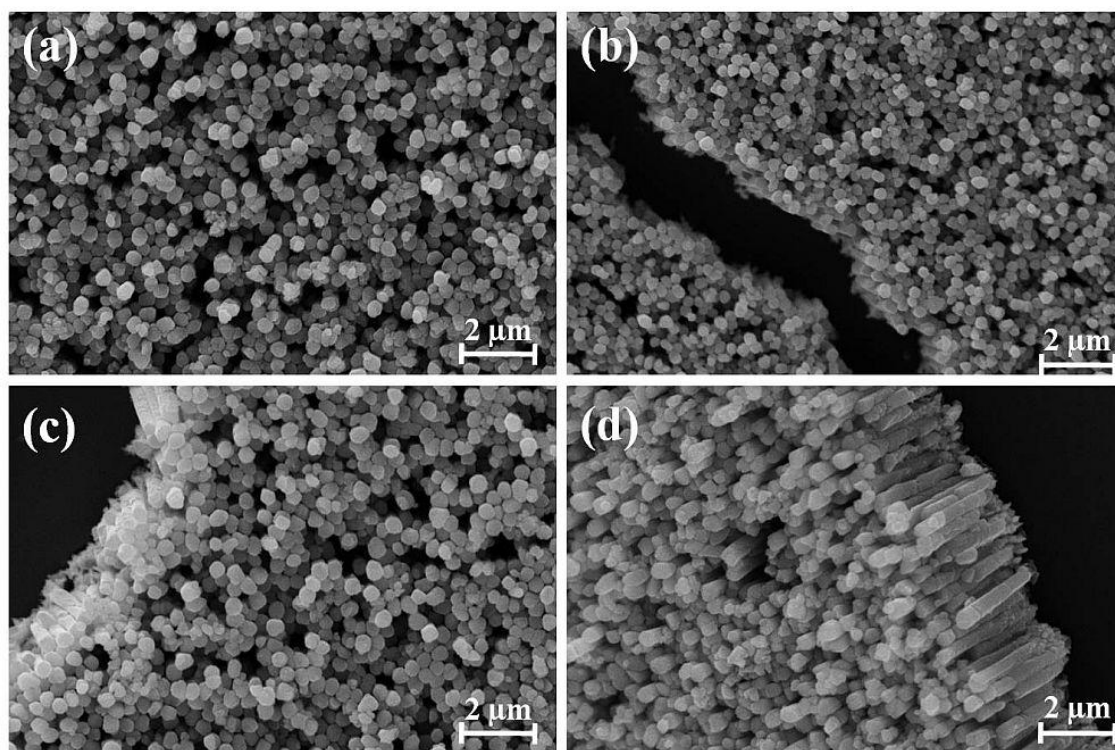
Figure 3.12: SEM images of vertically aligned Cu_2O nanopillars after the removal of AAO template in 1M NaOH solution for 1hr (a, b and c) Top view and (d) Cross sectional view.

From the above results we can conclude that 1M NaOH and 1hr dissolution time period are the optimized or suitable parameters for obtaining reproducible results. Though this experiment was carried out using commercially available AAO template with Cu_2O electrodeposited for 1000 seconds, it can be also extended to any other templates and materials deposited. However, care should be taken while choosing the etching parameters because the parameters used or optimized in this particular experiment will vary slightly from template to template and the materials deposited. From our experimental observation we suggest that for any sample prepared using longer/lesser deposition time, it is always suggested to use less concentration NaOH, preferably 1M NaOH, and vary the reaction time so that distortion free 1D

nanostructures can be obtained. Figure 3.12 shows the SEM images of vertically aligned Cu_2O nanopillars prepared by 1M NaOH solution and 1hr dissolution period. The length and diameter of the nanopillar was found to be ~4 μm and ~300 nm respectively. The XRD pattern of vertically aligned Cu_2O nanopillars and SEM image of samples prepared by 1M NaOH solution and 45 min and 50 min dissolution period were given in figure 3.13.
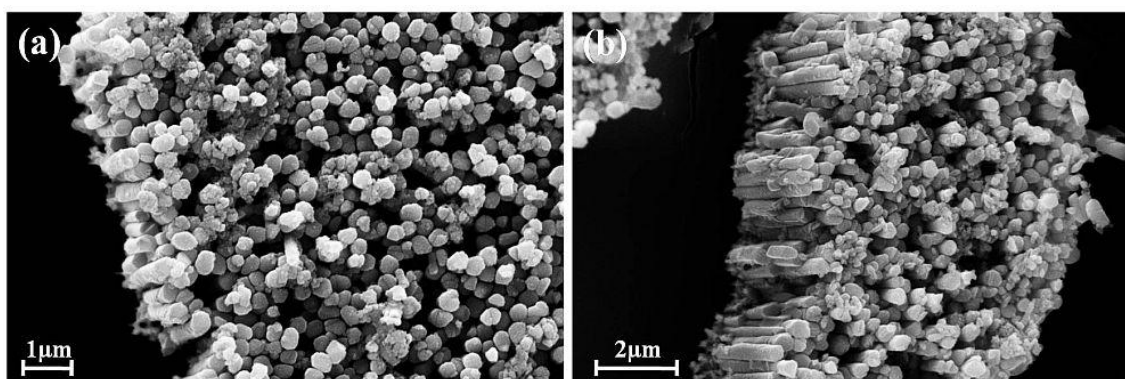
Figure 3.13: SEM images of vertically aligned Cu_2O nanopillars after the removal of AAO template in 1M NaOH solution for (a) 45 min and (b) 50 min.

3.3.2. Electrical Characteristics of Cu_2O Nanopillars

Figure 3.14 shows the electrical characteristics of vertically aligned Cu_2O nanopillars measured at different temperature (300 K-180K). From the I-V curve, we can clearly see that it exhibits symmetric characteristics. Generally, any metal/semiconductor based electrical devices can be explained based on two types of contacts at the junction. An ohmic contact, exhibiting linear I-V characteristics and the rectifying contact exhibiting non-linear I-V characteristics due to the existence of potential barrier at the junction [201, 202]. In addition, the electrical transport properties across this metal/semiconductor junction can be easily explained by using simple thermionic emission equations [203]. However, in most of metal-semiconductor-metal contacts based devices; two rectifying contacts are inevitable where the analysis of I-V (symmetric) characteristics using these conventional methods would lead to erroneous results [204]. Therefore, it is very necessary to use different electrical transport theory which can provide correct and reliable information. Herein, by considering two schottky barriers as a basic building block, we have analyzed the I-V characteristics of Au-Cu_2O Nanopillars-Au (MSM) structure

using back-to-back schottky diode model under the assumption of thermionic and field emission (TFE) theory [205].
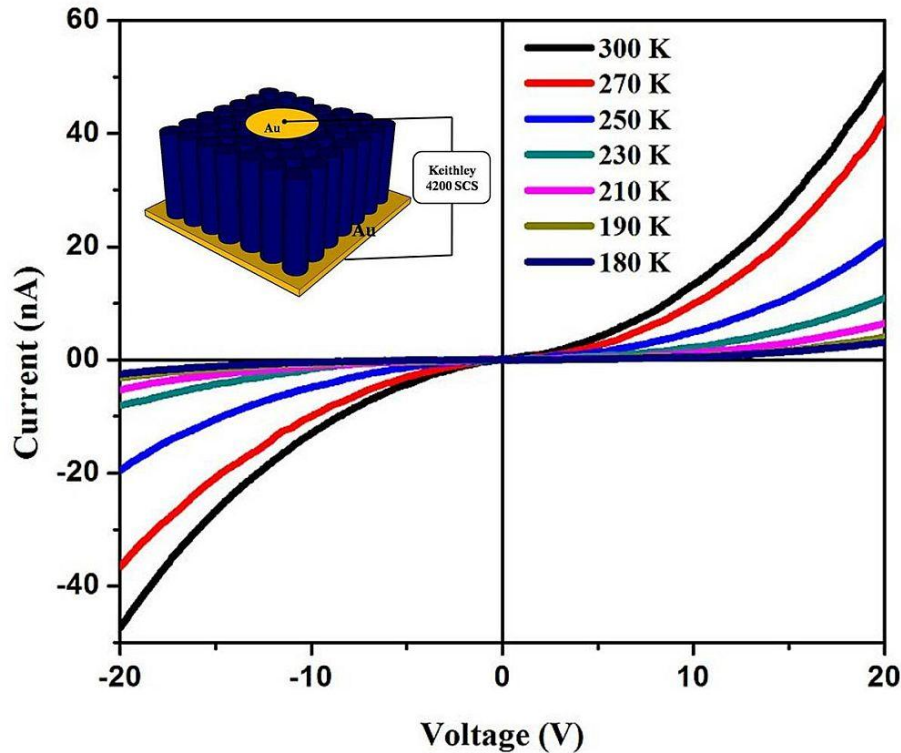
Figure 3.14: Temperature (180 K – 300 K) dependent current-voltage (I-V) characteristics of Cu_2O nanopillars (inset is the schematic representation of the device configuration used).

Figure 3.15a and 3.15b shows the schematic representation of metal-semiconductor-metal [Au-Cu_2O-Au -MSM] structure and its equivalent circuit consisting of two back to back Schottky diodes. The schottky barrier for the top and bottom schottky diode is referred as ϕ_{TSB} and ϕ_{BSB} respectively. When an external voltage V (positive or negative) is applied, the back to back diode configuration ensures that one junction is always forward biased and the other one is reverse biased (figure 3.15c). For instance, when positive voltage is applied to the top electrode, the potential at the top electrode is more positive when compared to the potential at the bottom electrode. In this case, the top diode is forward biased and the bottom diode is reverse biased. In the case of negative voltage applied to the top electrode, the potential at the bottom electrode becomes more positive than the top resulting in forward biased bottom electrode and reverse biased top electrode. Any voltage applied to the MSM structure will be distributed across top

and bottom Schottky diode and Cu_2O Nanopillars. When voltage V (positive or negative) is applied to the MSM structure, it can be divided into three portions V_1, V_2 and V_{NRs} as illustrated in the figure 3.15b. Where, V_1, V_2 and V_{NPs} are the voltages which are dropped across top schottky diode, bottom schottky diode and Cu_2O nanopillars respectively.
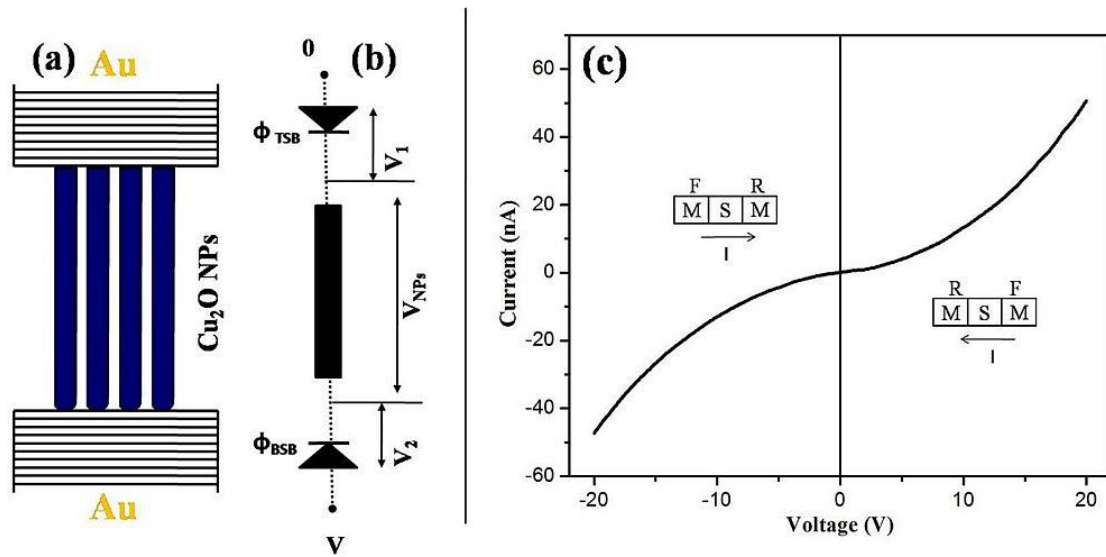
Figure 3.15: (a) Metal-semiconductor-Metal (MSM) representation and (b) equivalent circuit of Au-Cu_2O-Au structure (c) Room temperature I-V characteristics of Cu_2O nanopillars. F and R indicate the nature of biasing (F-forward, R-reverse) when voltage V (positive or negative) is applied across the metal-semiconductor junction.

The I-V characteristics of MSM structure, according to TFE, can be divided into two conduction regimes. In the first regime, the applied voltage V is small and most of the voltage is likely to be dropped across the reverse biased schottky diode [206]. As the voltage is gradually increased, the current is dominated by the tunnel assisted thermionic emission at the reverse biased junction. At high voltages, the transport enters the second regime, where the intrinsic resistance of Cu_2O nanopillars becomes more significant [207]. At this stage, most of the applied voltage is dropped across Cu_2O nanopillars and eventually the current is limited by conduction in the bulk which is almost linear.

In the first stage, the current due to voltage V is given by [198, 208],

$$I = A \times J_{TFE}(V, \Phi_B) = A \times J_{SR}(V, \Phi_B) \exp\left[V\left(\frac{q}{k_B T} - \frac{1}{E_0}\right)\right] = I_{SR} \exp\left[V\left(\frac{q}{k_B T} - \frac{1}{E_0}\right)\right] \quad (3.7)$$

where A is the cross-sectional area of the device and J_{SR} is the current density, and it can be written as,

$$J_{SR} = \frac{A^* T (\pi q E_{00})^{\frac{1}{2}}}{k_B} \exp\left(-\frac{\Phi_B}{qE_0}\right) \times \left[q(V-\zeta) + \frac{\Phi_B}{\cosh^2\left(\frac{qE_{00}}{k_B T}\right)}\right]^{\frac{1}{2}} \quad (3.8)$$

Where
$$E_0 = E_{00} \coth\left(\frac{qE_{00}}{KT}\right) \quad (3.9)$$

and

$$E_{00} = \frac{\hbar}{2}\left(\frac{N_d}{m^* \varepsilon_s}\right)^{\frac{1}{2}} \quad (3.10)$$

Here N_d, m^*, and ε_s are the carrier concentration, effective mass of holes and relative permittivity of Cu_2O NRs respectively. For further analysis equation (3.7) can be rewritten as given below [209],

$$\ln I = \ln I_{SR} + V\left(\frac{q}{kT} - \frac{1}{E_0}\right) \quad (3.11)$$

According to equation (3.11), the plot of $\ln I$ vs V gives the slope of q/kT-$1/E_0$ (figure 3.16). Therefore, the tunneling parameter (E_0) can be easily obtained from $\ln I$ vs V curve plotted for various (180 K -300 K) temperature. At room temperature, the value of E_0 was found to be 26.0 mV and it further increased to 26.3 mV for 180 K indicating that tunneling becomes more dominant at low temperature. By using E_0 values, the carrier concentrations present in the Cu_2O nanopillars were calculated. At room temperature it was found to be 5.45×10^{13} cm^{-3} and it further decreased to 3.45×10^{13} cm^{-3} on reducing the temperature to 180 K.
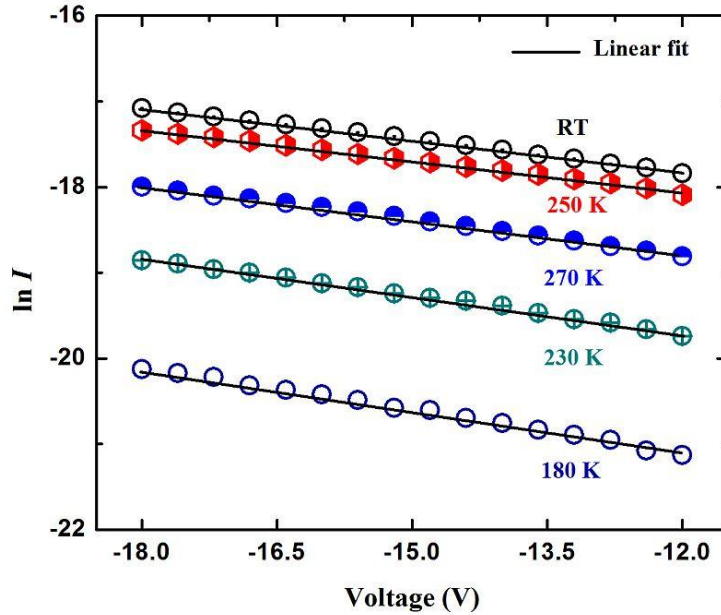
Figure 3.16: Temperature (180 K – 300 K) dependent semi logarithmic I-V characteristics of Cu$_2$O nanopillars. The dots and solid lines are the experiment and fitted results respectively.

According to TFE theory, the resistance of Cu$_2$O nanopillars can be obtained by differentiating the I-V curves at higher voltage [199].

$$R = \left(\frac{dV}{dI} \right) \qquad (3.12)$$

Figure 3.17a shows the resistance of Cu$_2$O nanopillars calculated at different temperatures calculated at higher voltage ranges. From the figure, we can clearly see that the resistance of Cu$_2$O nanopillars gradually increases as the temperature is decreased. At room temperature, the resistance of Cu$_2$O nanopillars was found to be $\sim 0.3 \times 10^3$ MΩ and it further increased to 3×10^3 MΩ at 180 K.

To further understand the electrical transport, the activation energy of the Cu$_2$O NRs was calculated by using the temperature dependent equation as given below [209],

$$R(T) = R_0 \exp\left(\frac{-E_a}{k_B T} \right) \qquad (3.13)$$

where E_a is the activation energy and K_BT is the Boltzman constant. Figure 3.17b shows the variation of ln R as a function of inverse of temperature (arhenius plot).
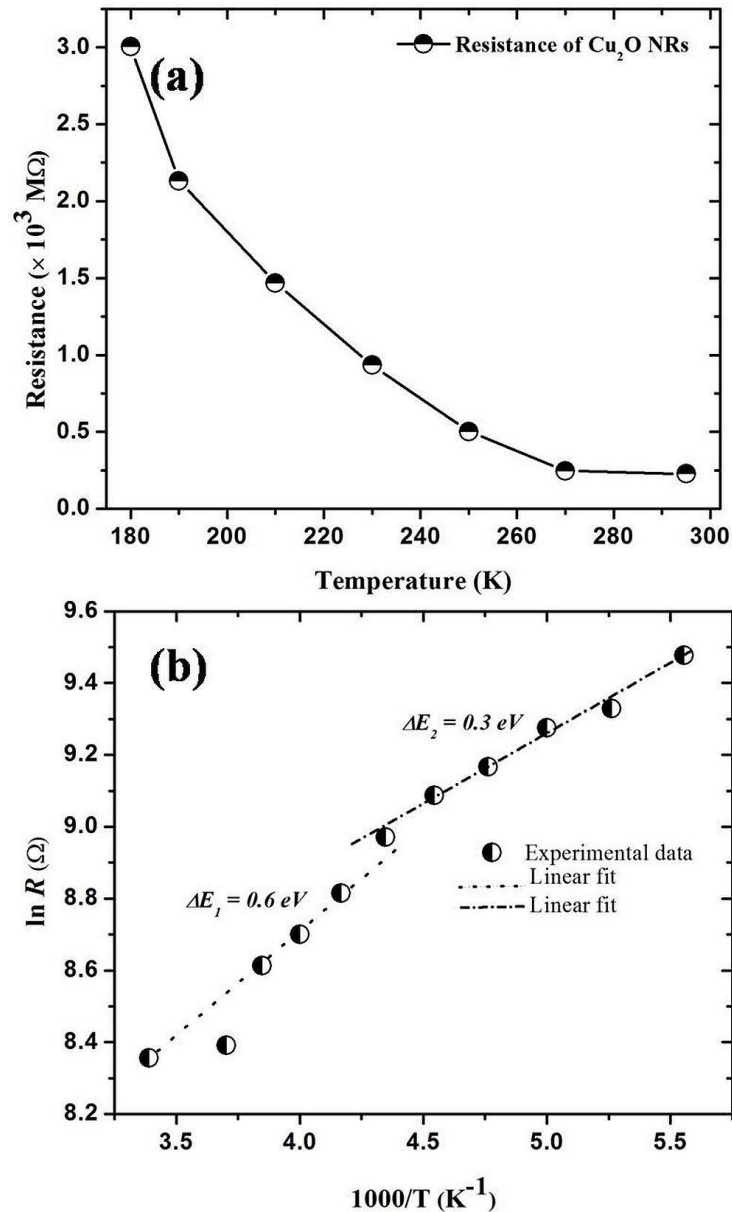
Figure 3.17: (a) Temperature dependent resistance variation of Cu_2O nanopillars and (b) ln (R) plotted as a function of 1000/T (Arhenius plot).

From the plot we can clearly see that there are two linear regions with different slopes emphasizing temperature dependent electrical transport. The activation energy for the region I

(300 K to 220 K) was calculated to be $\Delta E_1 = 0.6 \pm 0.1$ eV whereas for the region II (220 K to 180 K) it was found to be $\Delta E_2 = 0.37 \pm 0.04$ eV. These two activation energies (ΔE_1 and ΔE_2) calculated at region I and II can be attributed to copper (Cu) vacancy and the hole traps respectively located above the valence band maximum (VBM) [210]. This further confirms that there are defect levels with different activation energies which are contributing to the observed electrical properties of Cu_2O nanopillars at different temperature regime.

In summary, highly ordered Copper Oxide (Cu_2O) nanopillars were successfully grown inside the porous anodized alumina (AAO) template by electrodeposition technique. Nanopillars were liberated from the AAO template by appropriately choosing the NaOH solution. Temperature (180 K – 300 K) dependent current-voltage (I-V) characteristics of Cu_2O nanopillars revealed possible carrier activation from two defect sites with activation energies 0.3 and 0.6 eV respectively. The present study demonstrate a reliable recipe for the realization of free standing vertically aligned Cu_2O nanopillars on conductive substrate for solar cells and sensing applications.

CHAPTER FOUR

LOW TEMPERATURE HYDROGEN SENSING USING REDUCED GRAPHENE OXIDE AND TIN OXIDE NANOFLOWERS BASED HYBRID STRUCTURE

4.1. INTRODUCTION

Hydrogen (H_2) is considered to be one of the most promising sources of energy for next generation power and transportation sectors [211, 212]. It can be produced from zero-carbon methods such as wind, solar, nuclear power, and fossil sources using complete carbon capture and storage. Its extraordinary properties such as low molecular weight, high energy content and its combustibility without emitting any harmful gases make it an ideal choice for alternative energy source [212-214]. However, H_2 is very volatile and extremely flammable in nature, therefore a small leak in the atmosphere can cause a potential explosion [211, 215]. Since H_2 is a colorless and odorless gas, it cannot be detected by ordinary human senses [216]. Thus, development of cost effective H_2 sensors with high sensitivity and short response time is essential for safely harnessing energy from hydrogen.

One of the most promising candidates for sensing H_2 is reduced graphene oxide (RGO) which is chemically very facile to synthesize. RGO is a derivative of graphene and widely studied for gas sensing applications due to its high specific area (2630 m^2 g^{-1}) and high sensitivity [217]. In the recent past, though many studies have been carried out on RGO based H_2 sensing devices, most of those devices resulted in relatively high working temperature, poor sensitivity, high response and recovery time which are not suitable for practical applications [218, 219].

Metal oxides such as ZnO, CuO, WO_3, and SnO_2 were also widely investigated for their potential in monitoring various explosive and pollutant gases owing to their unique physical and chemical properties [220-222]. Among these, SnO_2 has attracted much attention in H_2 sensing applications owing to their high chemical stability, low cost, high sensitivity, fast response and recovery time. The sensing characteristics of SnO_2 are greatly dependent on various parameters such as morphology, porosity, surface to volume ratio, and shape [223]. So far, much of the H_2

sensing studies have been carried out on various types of SnO_2 nanomaterials, such as nanoparticles, nanorods, nanoflowers, nanograss and nanospheres [224-226]. Generally, the sensors made up of those SnO_2 nanostructures require high operating temperature (200-400°C) leading to higher power consumption [227]. In most of the cases the as prepared SnO_2 nanostructures are in powder form and the sensing devices are made out of these nanomaterials using binders which generally degrade the sensing characteristics [228].

An effective way to harness and improve the sensing characteristics of SnO_2 nanostructures will be to use RGO as a binder. Up to now, several RGO based composite materials has been synthesized by incorporation of metal/metal oxide nanoparticles for better sensing properties [229]. Although, above mentioned methods resulted in better H_2 sensing property, they still suffer from draw backs such as high cost, complex and time consuming process, which limit their wide applications [230, 231]. Moreover, the preparations of composites materials are carried out by an in-situ process which usually results in aggregation of RGO or nanoparticles limiting their efficiency [232].

In this work, we have integrated hydrothermally prepared 3D tin oxide nanoflowers (SnO_2 NFs) with solution processed 2D RGO nanosheets and used them to fabricate a highly sensitive H_2 sensor. The hybrid structure was found to possess structural properties (large surface area) of RGO and electrical properties of SnO_2. The hybrid composite nanostructure (RGO-SnO_2 NFs) exhibits highly enhanced sensitivity to hydrogen at low working temperature compared to pure RGO. The enhancement in the sensitivity to H_2 is due to the larger surface area and the formation of charge depletion layer at the RGO-SnO_2 NFs interface.

4.2. MATERIALS AND METHODS

4.2.1. Synthesis of Graphene Oxide

Graphene Oxide (GO) was synthesized by modified Hummer's method [233, 234]. Prior to drop casting process, the concentration of as prepared GO solution was diluted to 25% by the addition of pure DI water. Then it was ultra sonicated for 45 min to reduce the size of GO flakes and then centrifuged at 15000 rpm for 5 min in order to remove the thicker flakes. The top portion of the solution was collected in a vial and stored in room temperature for the further use.

By using this method, we were able to prepare 1 nm thick and few microns wide GO sheets. Figure 4.1a shows the atomic force microscopy (AFM) image of the GO thin film.

4.2.2. Synthesis of Tin Oxide (SnO$_2$) Nanoflowers

Tin Oxide nanoflowers (SnO$_2$ NFs) were successfully grown by hydrothermal method. Conventionally anisotropic growth is achieved by using environmentally harmful surfactants such as Cetyltrimethylammonium Bromide (CTAB) and Hexamethylenetetramine (HMTA). In this study we have synthesized SnO$_2$ NFs without using these surfactants by adopting the following recipe. 0.9 g of NaOH was added to 100 ml of glass beaker containing 40 ml of DI water followed by magnetic stirring for 30 min. Subsequently, 1.05 g of SnCl$_4$.5H$_2$O was added to the above solution while keeping it stirred. After 30 min, 40 ml of ethanol was added to the above solution very slowly which resulted in a white translucent solution. This resultant solution was transferred to teflon coated stainless steel autoclave and its temperature was maintained controllably in an oil bath at 200°C $\pm$ 1 for 24 hr. The light blue color final product was collected and washed with copious amount of DI water and ethanol to remove any unwanted chloride ion impurities followed by drying in convection air oven at 60°C for 12 hrs [235].
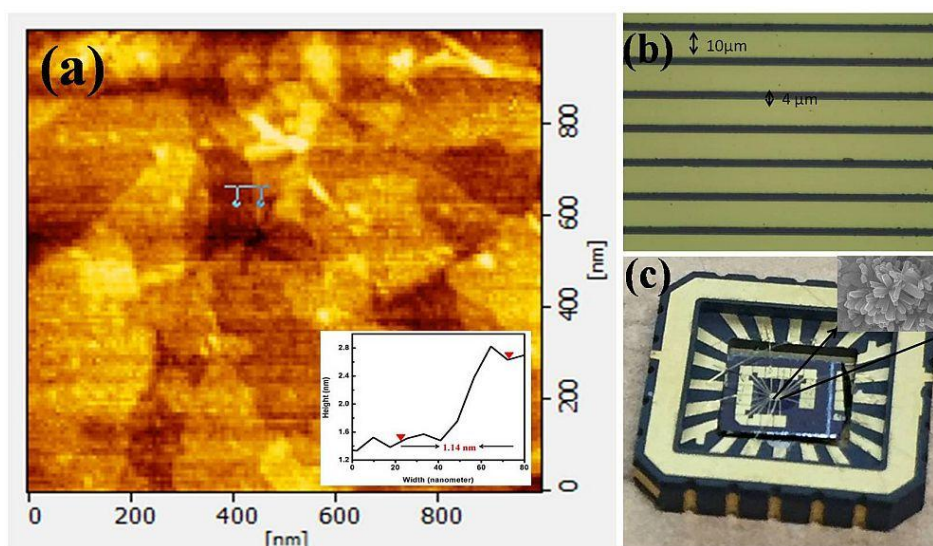
Figure 4.1: (a) AFM image of GO thin film drop coated on Si substrate. (b) Microscope image of as fabricated Au electrodes. (c) As fabricated gas sensor placed inside the chip carrier. Inset is the FE-SEM image of the drop casted RGO-SnO$_2$ based sensing layer.

4.2.3. Fabrication of Gas Sensing Device

The device fabrication consists of two steps. Firstly, the pre-patterned metal (Ti/Au) electrodes with 4 μm gaps were fabricated by photolithography technique. Following are the procedure taken for the fabrication of metal electrodes using photolithographic technique. The metal electrodes were fabricated by Photolithography (negative resist) technique. The following are the steps taken to fabricate the metal electrodes:

The entire process of fabricating interdigitated electrodes (figure 4.1b) was carried out in class 1000 clean room. To start with, Si substrates (3×3 cm) with 300 nm SiO_2 were cleaned by sonication in acetone and IPA, each for 10 min and then followed by cleaning it with nitrogen blow to remove any unwanted polymer or organic residues. After the cleaning process,

1) The photoresist was spin coated at 500 RPM for 5 sec followed by 5000 RPM for 25 sec.
2) Then it was baked at 90^0C for 1 min in the hot plate.
3) Then it was loaded into UV based mask aligner system (MDA-40FA) along with the required mask aligner (figure 4.3a).
4) The samples were subjected to UV photolithography, for defining the pattern, consisting two step exposures. In the first step, it was exposed to UV light for 1sec followed by heating at 130^0C for 105 sec. In the second step, it was exposed to 60 sec.
5) After the exposure, the sample was developed by dipping it in the developer for 22 sec then it was washed in DI water followed by nitrogen blow.
6) After developing, the sample was subjected to metal coating (Au (100 nm)/Ti (10 nm)) by e-beam evaporation technique (figure 4.3b).

Finally, lift-off process was carried out in acetone followed by cleaning it with IPA and nitrogen blow. During each process, we were able to fabricate maximum 6 electrodes in a 3×3 cm Si substrate and they were cut into individual electrodes (device) by dicer. It was further used for fabrication of gas sensing devices. Figure 4.1b shows the microscopic image of the interdigitated electrodes fabricated on SiO_2/Si substrate. Now the sensing layer was prepared by directly drop casting 0.5 μl of solution on a metal electrodes containing GO and SnO_2 NFs followed by annealing at 400^oC (figure 4.1c). The mixture solution is the uniform dispersion of 0.5 ml GO and 1 mg of SnO_2 NFs powder prepared by ultra sonicating it for 30 min. Under

same experimental condition control sample was prepared by directly drop casting 0.5 µl of 25% GO. To use the fabricated device as a gas sensor, it was connected to chip carrier using gold wire by wire bonder. Finally, it was fixed into sensing chamber by placing it in chip holder. Figure 4.2 shows the schematic diagram of RGO-SnO$_2$ NFs based hydrogen sensor. For clarity, only the hydroxyl groups in RGO were considered in schematic representation.
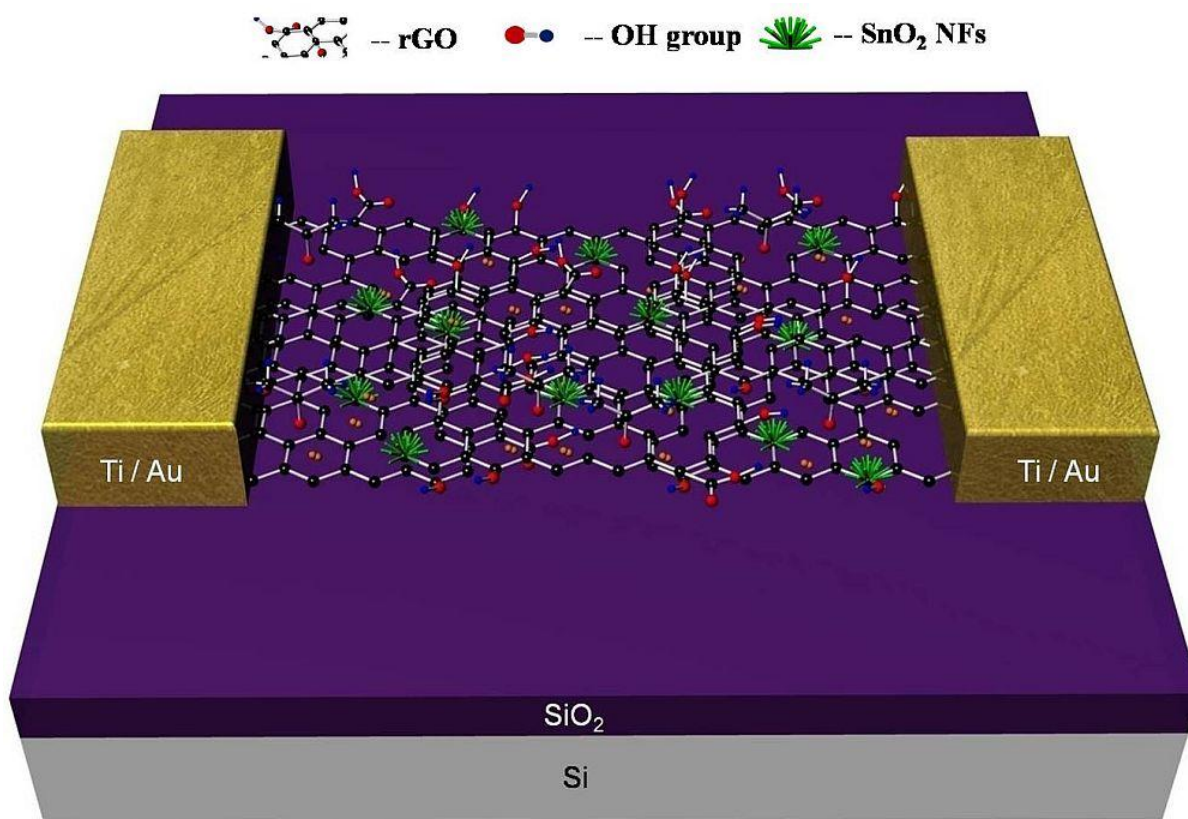
Figure 4.2: Schematic diagram of RGO-SnO$_2$ NFs based hydrogen gas sensor.

4.2.4. Hydrogen Gas Sensing Measurements

The gas sensing measurements were carried out in a closed chamber equipped with PID controlled electrical heater (figure 4.4). Before starting the sensing measurement the chamber was evacuated to ~ 1×10^{-3} mbar by rotary pump. To register sensing signal, high purity H$_2$ gas (99.99%) introduced at optimized concentrations by mass flow controller (MKS, USA) while monitoring the electrical response of the sensor by current-voltage (I-V) measurement system (Keithley 4200 SCS).
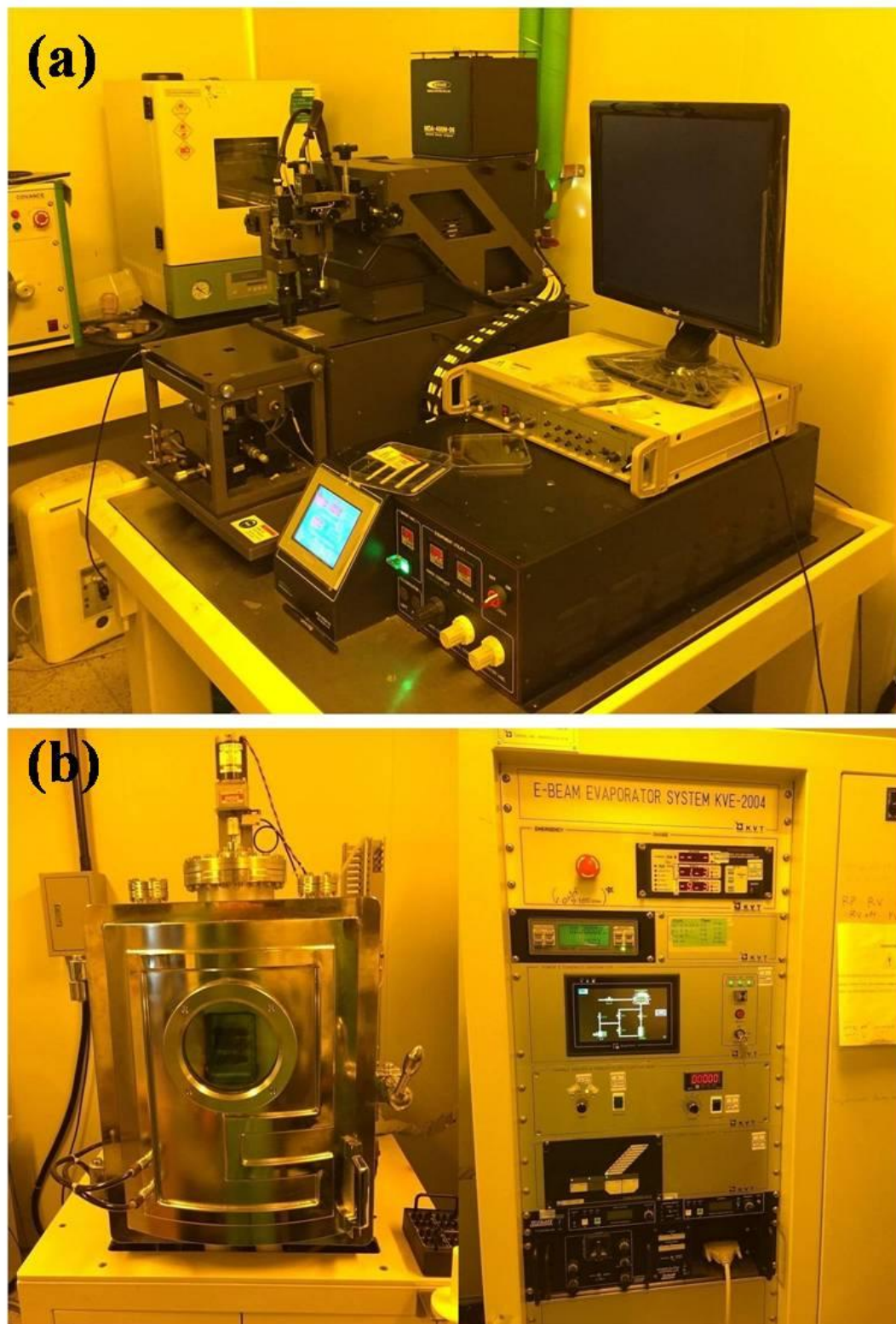
Figure 4.3: Experimental setup used for fabrication of interdigitated metal electrodes (a) Photo lithography unit (b) e-beam evaporation unit.
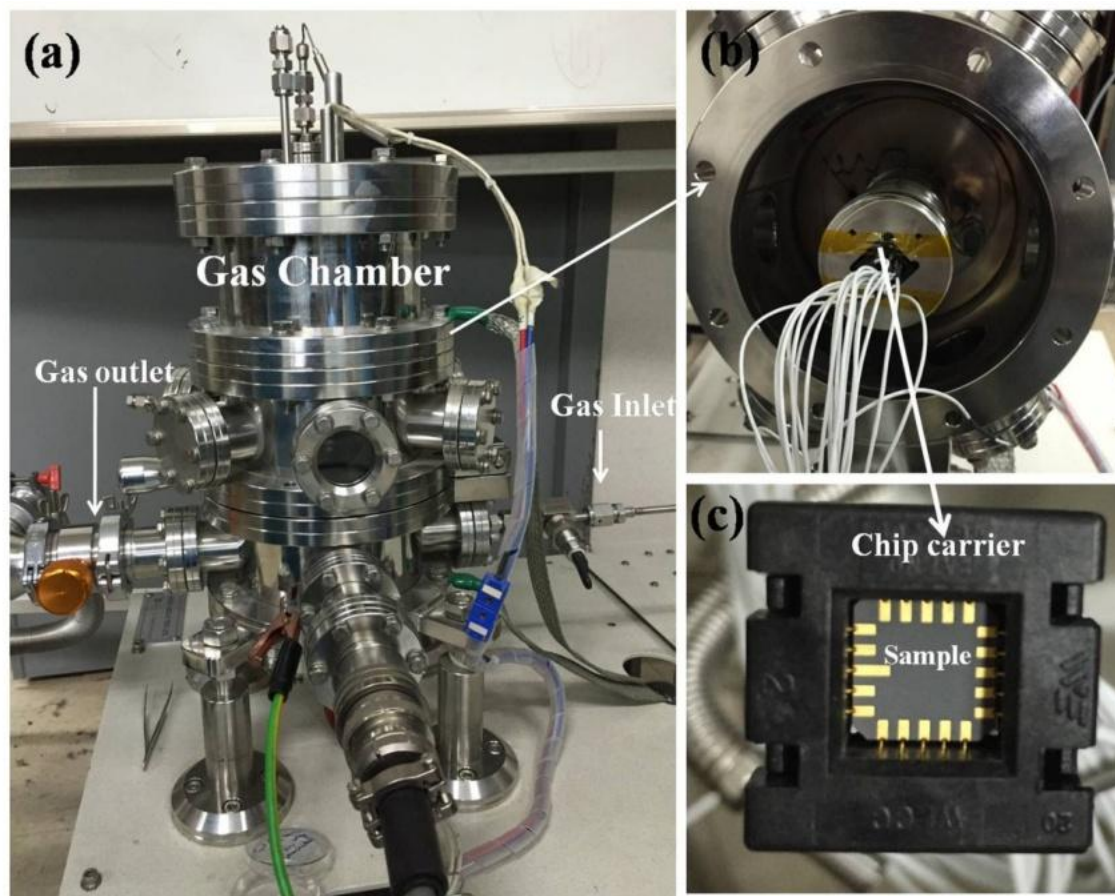
Figure 4.4: Experimental setup used for Gas sensing measurement

From FE-SEM images, it can be clearly seen that the as prepared hydrothermally grown SnO_2 forms a flower like structure (figure 4.5a and figure 4.5b). Each flower like structure consists of large number of nanorods with common base. The average width of the nanorods was found to be ~ 74 nm and the length to be ~ 250 nm. Figure 4.5c and 4.5d, shows that SnO_2 NFs are integrated into RGO in two ways. In the first case, SnO_2 NFs protrudes out of RGO layer, allowing top portion of the nanoflowers to interact with H_2. In the second case, SnO_2 NFs are completely covered by RGO sheets, which are free from wrinkles and agglomerations. The chemical reaction for the formation of SnO_2 NFs can be given by,

$$Sn^{4+} + 6OH \rightarrow Sn\,(OH)_6^{2-} \tag{4.1}$$

$$Sn\,(OH)_6^{2-} \rightarrow SnO_2 + 2H_2O + 2OH^- \tag{4.2}$$

4.3. RESULTS AND DISCUSSIONS
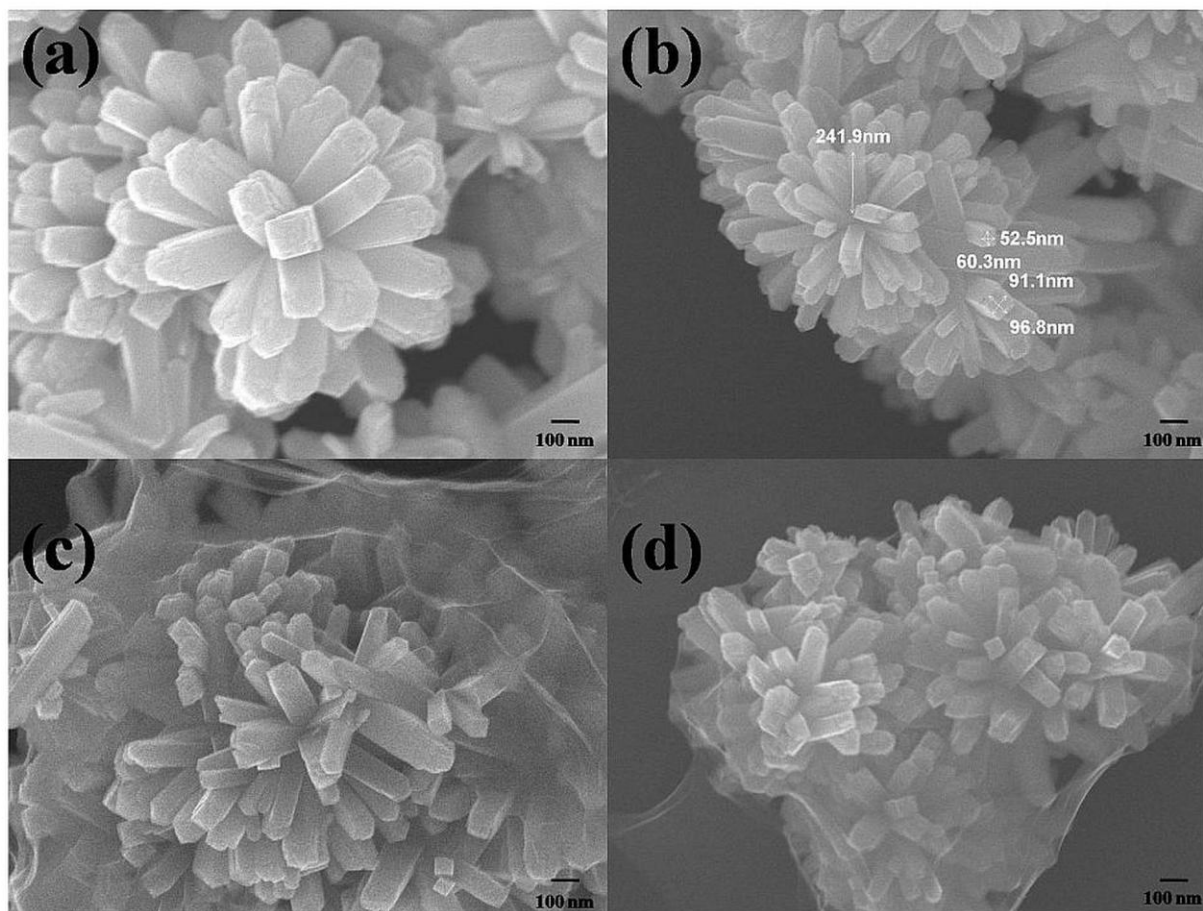
Figure 4.5: (a) and (b) FE-SEM images of hydrothermally prepared SnO_2 NFs. (c) and (d) FE-SEM images of RGO-SnO_2 NFs hybrid composite film.

From equation (4.1) and (4.2), it can be clearly understood that during the hydrothermal reaction an intermediate product is formed and it decomposes into large number of small SnO_2 nuclei and each nuclei further grows ($Sn(OH)_6^{2-}$) into nanoflowers consisting large number of nanorods. Since the growth of these SnO_2 NFs were carried out in the absence of surfactant the observed rod like structure can be attributed to chemical potential of the water/ethanol and the inherent crystalline structure of the SnO_2. For rutile structure, the surface energy of SnO_2 for various crystal faces can be sequenced as (110) < (100) < (101) < (001). It is this inherent crystal property, assisted by ethanol/water system, which promotes nuclei to grow

anisotropically along (001) direction forming nanorods structure by favoring the minimum surface energy [236].
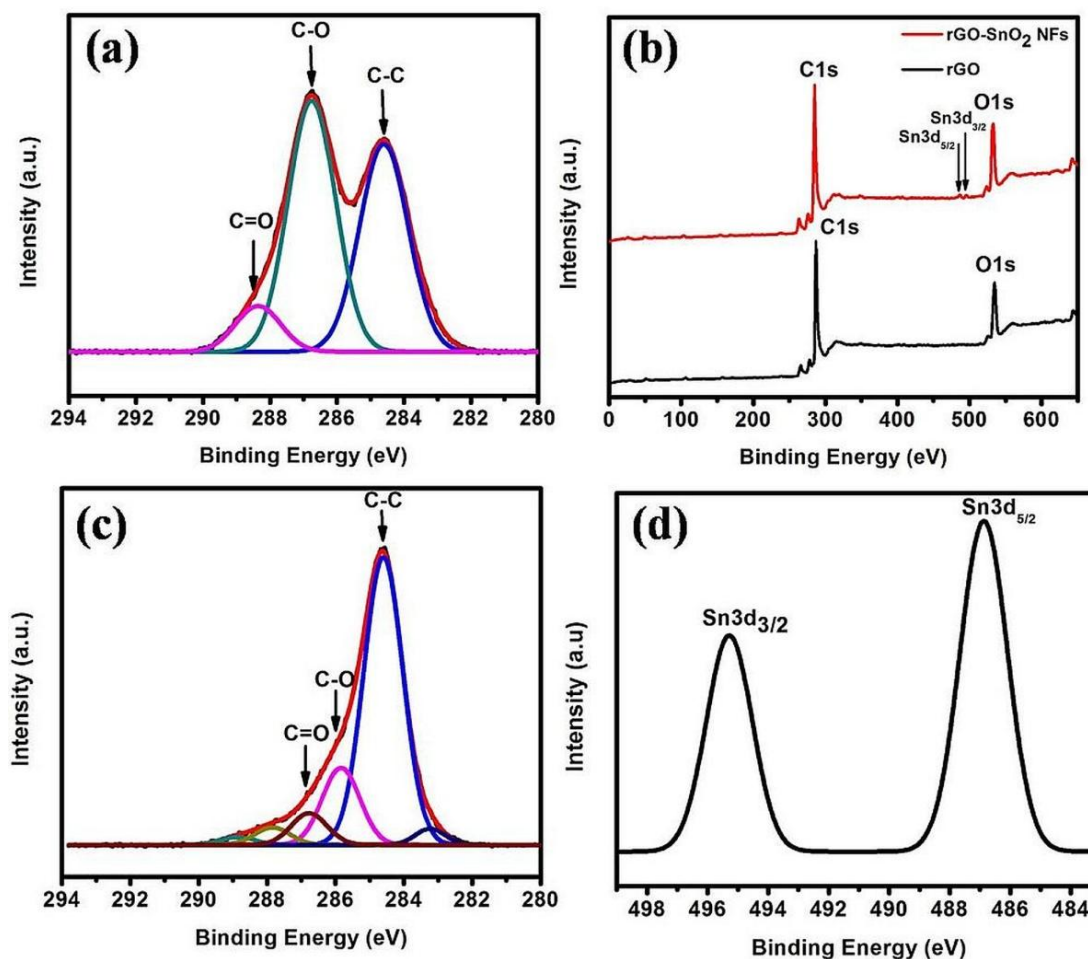
Figure 4.6: High resolution XPS and curve fit of (a) C1s in untreated GO. (b) XPS survey spectra of RGO with and without SnO_2 NFs. High resolution XPS and curve fit of (c) C1s in RGO-SnO_2 NFs hybrid composite and (d) Sn3d in RGO-SnO_2 NFs hybrid composite structure.

The chemical composition of GO, RGO and RGO-SnO_2 NFs hybrid structures were investigated by X-ray photoelectron spectroscopy (XPS) analysis. Figure 4.6b shows the survey spectrum of RGO and RGO-SnO_2 NFs. The bands observed at 284.6 and 530.4 eV are attributed to carbon (C) and oxygen (O) 1s core level binding energies, respectively [237]. In RGO-SnO_2 NFs, apart from C1s and O1s peaks, several bands associated with Sn element was also observed. The Sn 3d spectrum of RGO-SnO_2 NFs (figure 4.6b, and 4.6d) observed at 487.3 eV and 494.9 eV, confirms the presence of SnO_2 NFs in the hybrid structure [232, 238]. The C1s

spectrum of GO and RGO-SnO$_2$ NFs are given in figure 4.6a and 4.6c exhibiting three peaks at 284.6, 286.8 and 288.7 eV, attributed to C-C, C-O and C=O bands. The presence of C-O and C=O peaks in the C1s spectrum of RGO-SnO$_2$ NFs implies that oxygen containing groups such as hydroxyl, carbonyl and epoxide are still present even after the annealing treatment [237, 238]. However, the peak intensities of C-O and C=O has tremendously decreased compared to untreated GO (figure 4.6d) suggesting that most of the functional groups in RGO-SnO$_2$ NFs has been removed after the annealing at 400°C.
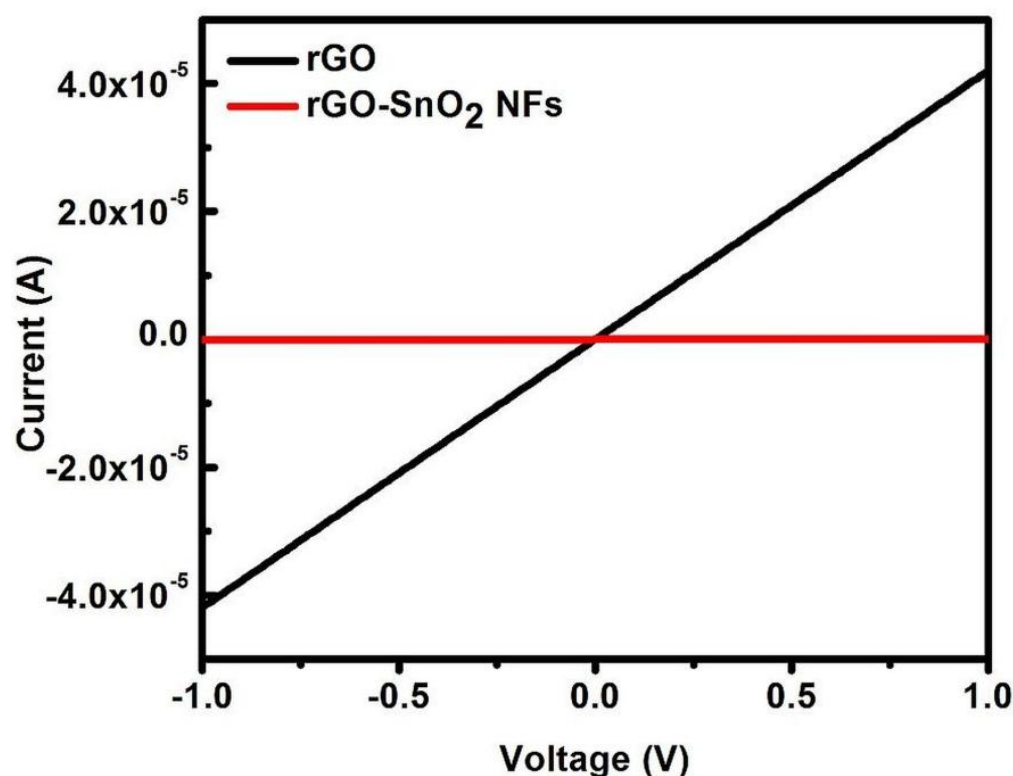
Figure 4.7: I-V characteristics of RGO and RGO-SnO$_2$ NFs hybrid composite annealed at 400°C.

4.3.1. Hydrogen Sensing Characteristics of RGO and RGO-SnO$_2$ NFs

The as fabricated sensing devices, both RGO and RGO-SnO$_2$ NFs, were initially tested for its room temperature (~25°C) conductivity by carrying out current - voltage (I-V) measurement. This is done to confirm the presence of RGO, as the parent material GO is non-conductive due to the extensive presence of saturated sp^3 bonds, high density of electronegative oxygen atoms bonded to carbon and other defects. From I-V characteristics (figure 4.7), the

resistance of the RGO based device is found to be ~ 20 kΩ which indicate that GO has been reduced successfully. The linearity of the I-V curve shows that the contacts have a very low Schottky barrier. After the addition of SnO_2 NFs to RGO, the resistance increased to ~ 30 MΩ which is three orders of magnitude greater than the pure RGO sample. This can be attributed to the formation of depletion layer, at the interface between SnO_2 NFs and RGO [232].

For all the sensing measurements, we first test the response of each sample to Hydrogen gas for a very long period of time. The graph for one such test measurement is shown below (figure 4.8). In the graph, it can be clearly seen that the response had reached the saturation value around 600 seconds. Therefore, for all the sensing measurement we had limited our exposure time to 400 sec as the sample reached 90% responsivity during this time and response increased very slowly thereafter.
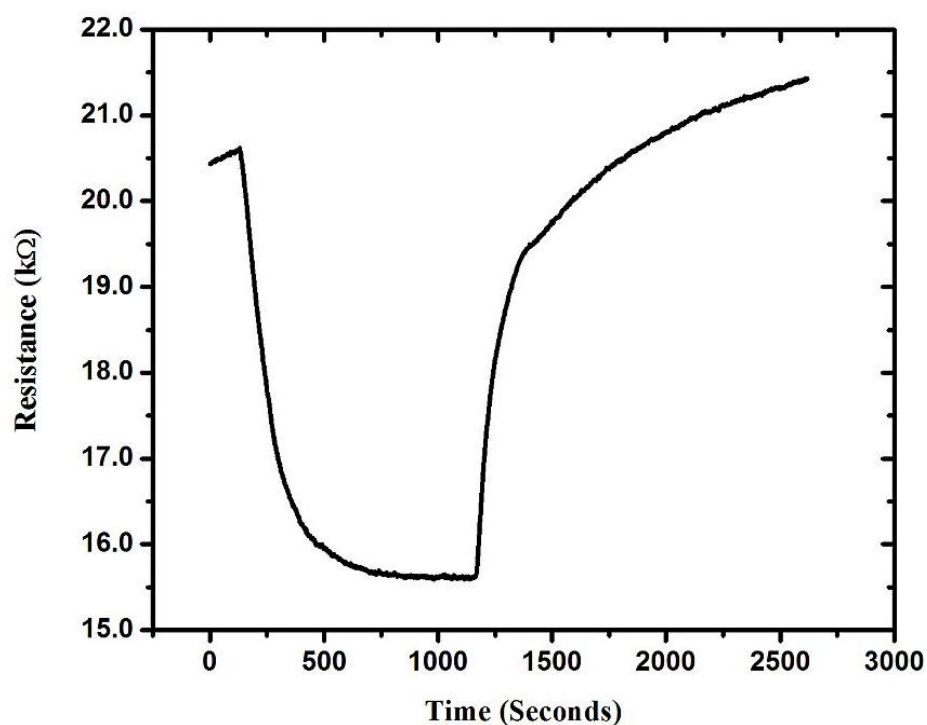
Figure 4.8: Test measurement of resistance variation for longer time period

Figure 4.9a and 4.9b shows the resistance variation of control sample and RGO-SnO_2 NFs composites upon exposure to H_2 measured at room temperature (RT) and 40^oC respectively. The measurements were performed for different concentration of H_2 ranging from 200 – 1000

ppm. The time used for introduction (ON) and removal (OFF) of H_2 was 400 s and 300 s respectively.
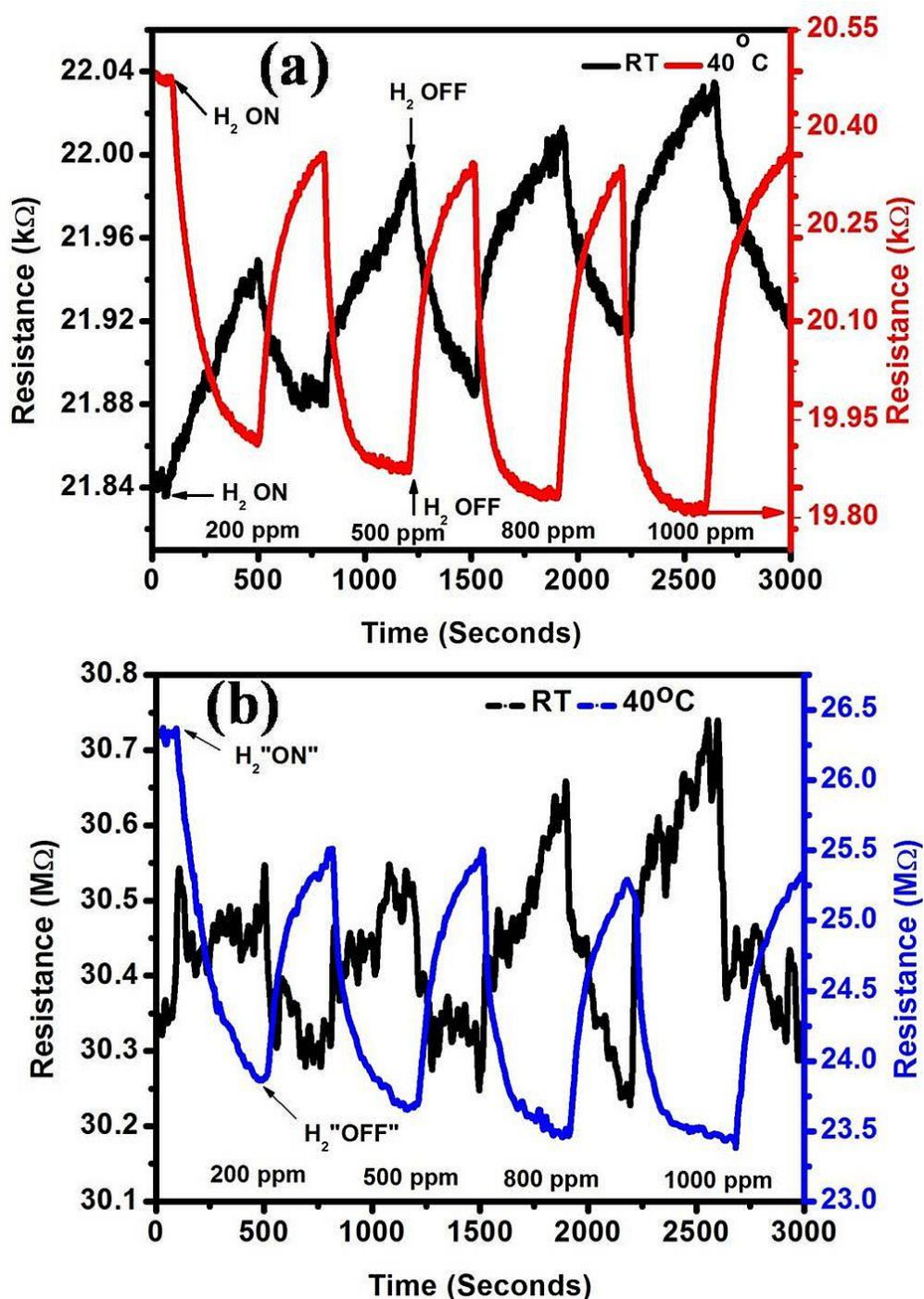
Figure 4.9: Resistance variation upon exposure to various concentration of hydrogen at room temperature and 40^oC respectively (a) in RGO and (b) RGO-SnO$_2$ NFs composite.

At room temperature, when hydrogen is "ON" the resistance of the device increased resulting in a peak (p-type conductivity) and it decreased while the temperature was increased to 40°C resulting in a valley (n-type conductivity). By plotting both the curve together we can clearly see that the peak and valleys occurs in opposite phase. This is an effect commonly seen in chemically processed samples where there exist significant number of vacancies, defects and hydroxyl group over which Oxygen get weakly adsorbed. On slightly increasing the surface temperature Oxygen gets desorbed leaving the sample surface electron rich. Similar kind of behavior was observed in RGO by Le-Sheng Zhang et. al [239].

The sensing response, response time and recovery time of both the devices were studied in order to understand the effect of incorporation of SnO_2 NFs into RGO nanosheets. The response of the device is defined as [240],

$$Response = (R - R_o)/R_o \times 100\% \qquad (4.3)$$

where, R is the resistance of the sample exposed to the gas and R_o is the baseline resistance in air. The H_2 sensing response of as fabricated sensors, both RGO and RGO-SnO_2 NFs, were carried out in a gas sensing chamber as described in the experimental section. H_2 was introduced (400 s) and removed (300 s) from the chamber periodically. Both introduction and removal of H_2 was considered as a single period (700 s). The H_2 concentration was varied after each period and the concentration used were 200, 500, 800 and 1000 ppm, resulting in a sensing curve containing four periods in series for a particular operating temperature.

Figure 4.10a and 4.10b shows the sensing responses of both RGO and RGO-SnO_2 NFs at different operating temperatures. The operating temperature used for the sensing measurement was 40°C, 50°C, and 60°C. From the room temperature sensing curve (figure 4.10b), it can be clearly seen that addition of SnO_2 NFs into RGO indeed improves the sensing response. The improvement becomes very remarkable when the operating temperature is increased to higher values (40°C and 60°C).

The responses of RGO-SnO_2 NFs at 60°C was found to be 19.6%, 21.2%, 22.74% and 22.91% for the concentration of 200, 500, 800, and 1000 ppm respectively. For the same concentration and operating temperature, the responses of RGO was calculated to be 8.6%,

9.59%, 10.28% and 10.51% and its highest response for 200 ppm was 22.2% at 150°C. For e.g. at 60°C the response of RGO has been improved by 126 % for 200 ppm due to the addition of SnO$_2$ NFs (figure 4.11). Furthermore, we also verified the variation in the sensitivity for 4 to 5 on-off cycle and it was found to be around 5%. This percentage was calculated by determining the difference in peak resistance value after every exposure cycle.
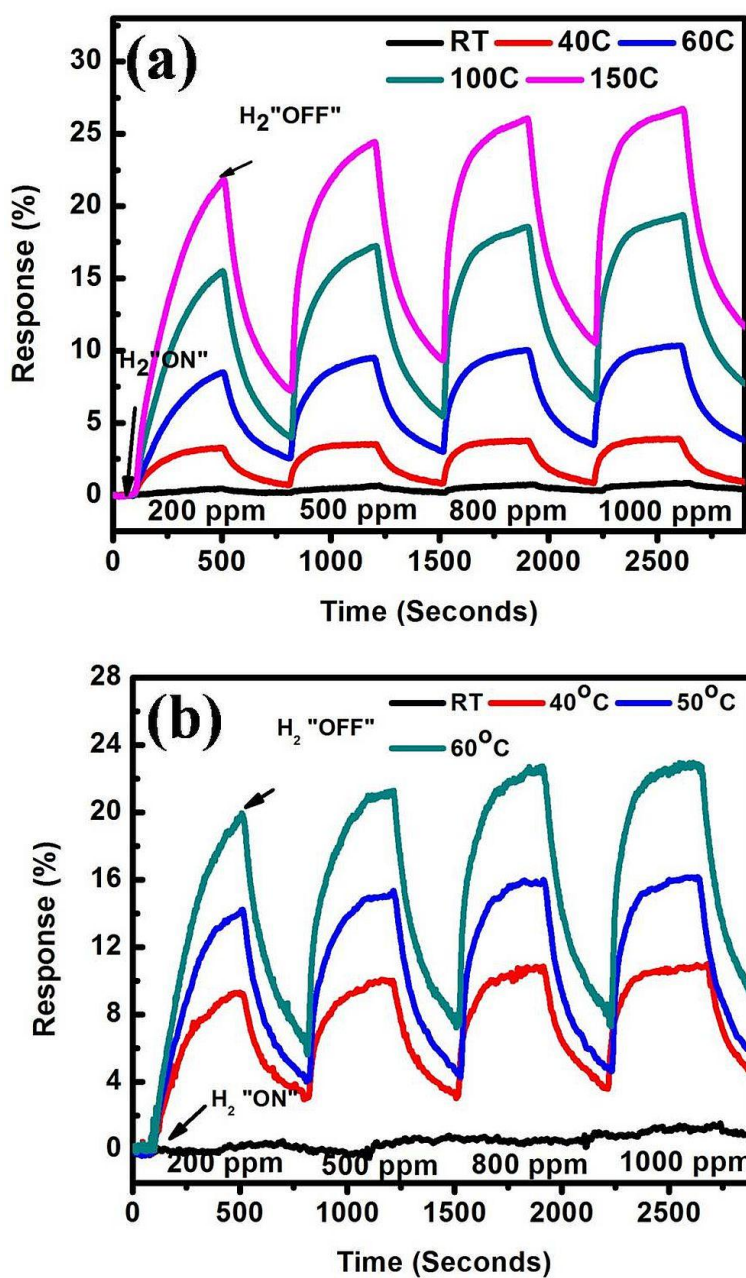
Figure 4.10: Hydrogen sensing characteristics of (a) RGSO and (b) RGO-SnO$_2$ NFs composite film.
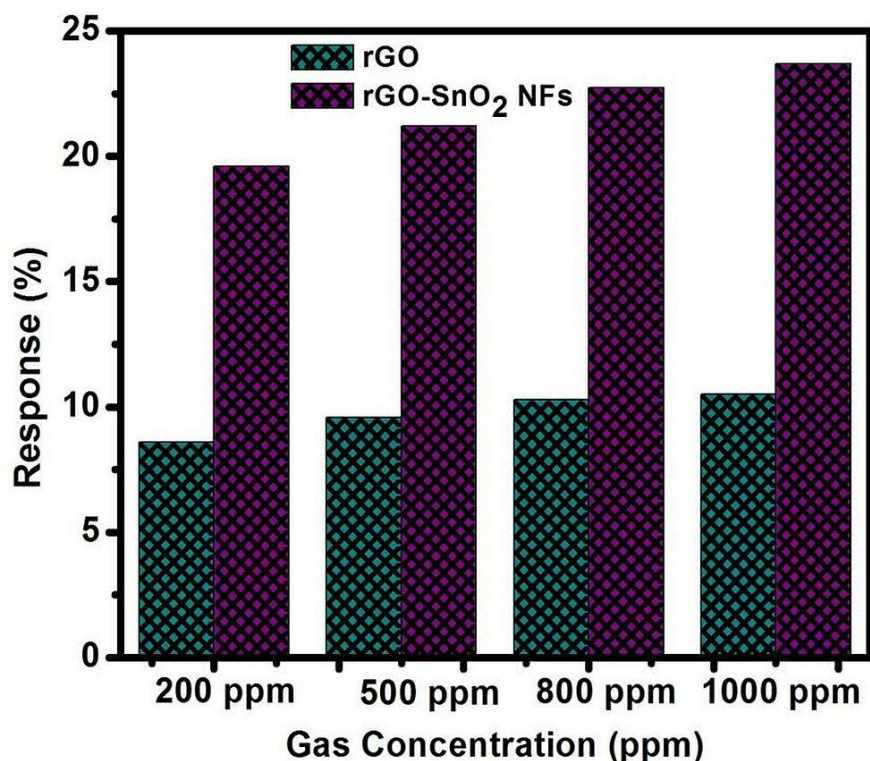
Figure 4.11: Comparative H_2 sensing response of RGO and RGO-SnO$_2$ NFs based composite film at 60°C.

Table 4.1: Comparison of Sensing Performance of the H$_2$ Sensor prepared in this work with those reported in the literature.

Materials	Working Temperature [^{o}C]	Concentration [ppm]	Response [%]	Reference
Reduced graphene oxide/SnO$_2$ nanoparticles	50°C	1000	3.2	[241]
Graphene/ZnO Nanocomposite	150°C	200	3.5	[242]
Palladium loaded Tungsten Oxide nanoparticles	200°C	200	20	[243]
Ni doped TiO$_2$ Nanotubes	200°C	1000	13.8	[244]
Reduced graphene oxide	300°C	200	17	[245]
Pd loaded SnO$_2$ nanofibres	320°C	1000	12	[246]
RGO-SnO$_2$ NFs	60°C	200	19.6	This work

We also have gathered sensing data from published literatures and listed them in Table 4.1. It is clear from the table that the sensing response reported in our work is much better than the previously published results on H_2 sensing.
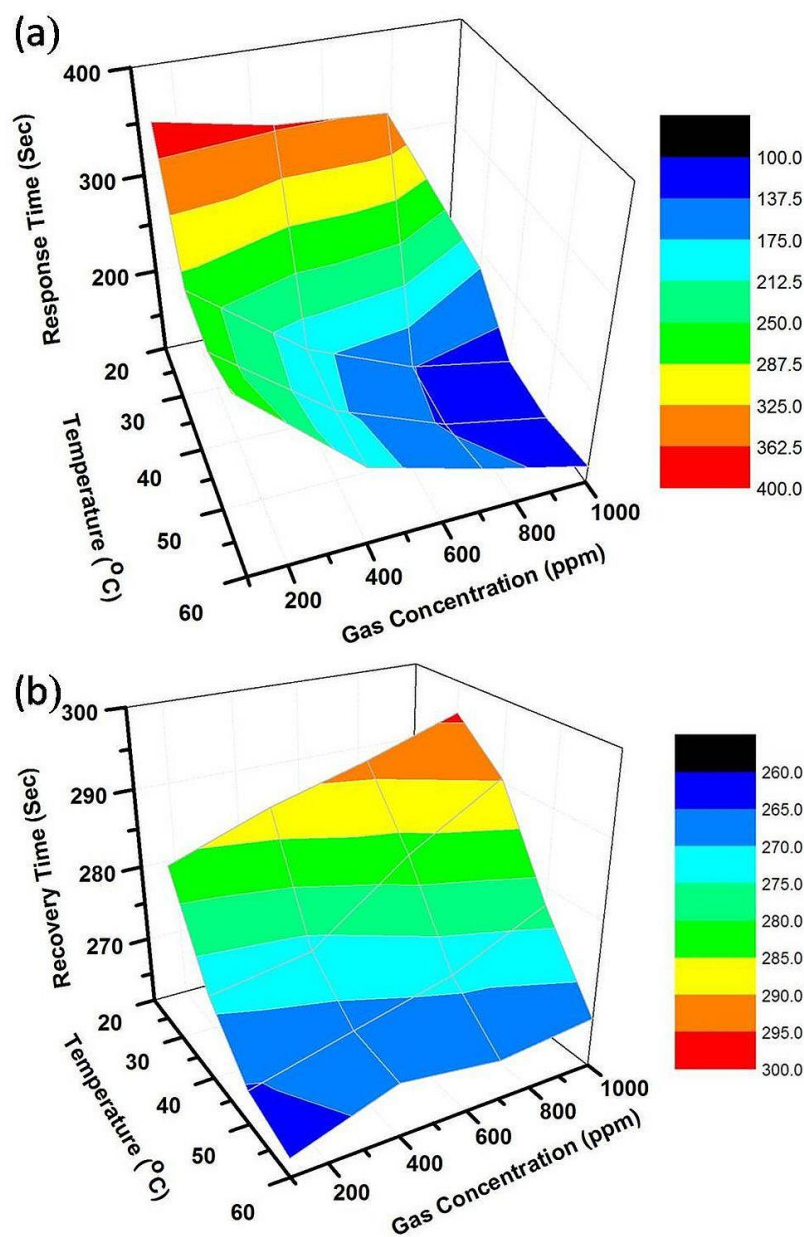
Figure 4.12: (a) Hydrogen sensing response time and (b) recovery time of RGO-SnO$_2$ NFs hybrid structure.

Figure 4.12a and 4.12b shows the H_2 response and recovery time curve (color strip in both the curve indicates the time) of RGO-SnO$_2$ NFs hybrid sensor. The response time is defined as the

time required for the response to increase from its base value to 90% of its highest value. The recovery time is defined as the time required for the response to decrease from 90% of its highest value to its initial value [229]. It was found that, when the operating temperature was increased by 10°C from RT the response time has decreased and the same trend was observed up to 60°C. The RGO-SnO$_2$ NFs showed a response time of 119.61 s at 60°C for the concentration of 1000 ppm as compared to the pure RGO sample which showed the response time of 145 s. The recovery time of hybrid sensor decreased monotonously as the operating temperature was increased from RT to 60°C and it showed a recovery time of 265 s for 1000 ppm at 60°C. The as prepared pure RGO sample showed a recovery time of 275 s at the same operating parameters. As in the case of sensitivity, we have also verified the variation in the response time and recovery time for different cycles and it was always found to be below 5%. A comparative study for the response and recovery time of our sample with already published literature shows that our sample sensing characteristics was much better than the previously reported values [table 4.2].

Table 4.2: Comparison of response and recovery time of H$_2$ Sensor prepared in this work with those reported in the literature.

Samples	Operating temperature (^{o}C)	Concentration (ppm)	Response time (sec)	Recovery time (s)	Reference
Nanostructured molybdenum oxide	200°C	1000	270	-	251
CuO-Cu$_x$Fe$_{3-x}$O4 nanostructured thin	295°C	1250	190	400	252
Pt/MoO$_3$ with La$_2$O$_3$ layer	180°C	1250	135	507	253
SnO$_2$ functionalized AlGaN/GaN	50°C	10000	240	570	254
Pd-WO$_3$ thick film	200°C	200	270	-	255

4.3.2. Selectivity of RGO-SnO$_2$ NFs Composites

For the practical sensor applications, a sensor should be highly selective to various gases. We therefore verified the selectivity of RGO-SnO$_2$ NFs sensors upon exposing it to NH$_3$ for 200 ppm at operating temperatures RT, 40°C and 60°C respectively. For example, at 60°C, the

sensing response of our sample to H_2 is 19.6 % whereas for NH_3 is 15.96 % (figure 4.13). The selectivity coefficient (K = Response $_{H2}$/Response$_{NH3}$) for H_2 to NH_3 at this operating condition was found to be 1.22 confirming selective detection of H_2.
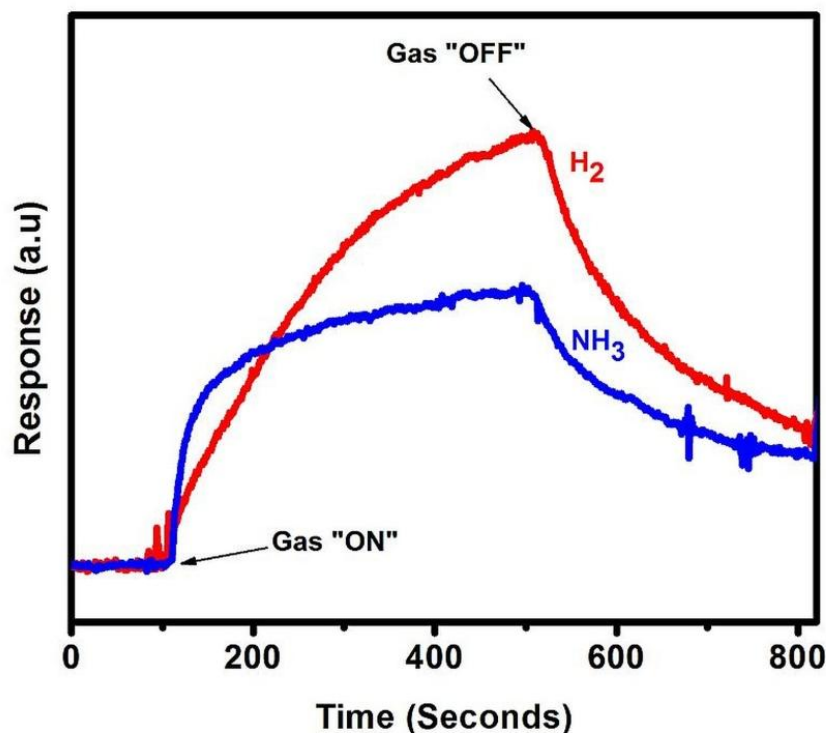
Figure 4.13: Sensing response of RGO-SnO$_2$ NFs to NH$_3$ and H$_2$ at the operating temperature of 60°C for 200 ppm.

The higher sensing performance of the RGO-SnO$_2$ NFs hybrid composite can be attributed to three factors.

4.3.3. Sensing Mechanism of RGO-SnO$_2$ NFs

(i) First and the foremost factor is the way by which SnO$_2$ NFs gets structurally integrated with RGO to improve the available active sites for H$_2$ interaction. As seen in FE-SEM images, the structural integration occurs in two ways namely type 1 and type 2. In type 1 hybrid structure, SnO$_2$ NFs protrudes out of the RGO sheets and it directly comes into contact with the H$_2$ molecules. The protruding nanorods create more open ends resulting in more active sites, such as vacancies, defects and unsaturated bonds which greatly facilitate the adsorption and

98

diffusion of H_2. In type 2 hybrid structure, SnO_2 NFs are covered by the RGO sheets and it plays significant role in preventing the aggregation of RGO sheets which in turn increases the active surface area (figure 4.15a and 4.15b).

(ii). Secondly, the change in resistance due to interaction between oxygen molecules absorbed on SnO_2 and H_2 gas. When O_2 molecule gets absorbed on the surface, it gets converted into negative ion by the following reaction [231].

$$O_2(air) \rightarrow O_2(ads) \tag{4.4}$$

$$O_2(ads) + e^- \rightarrow O_2^-(ads) \tag{4.5}$$

When SnO_2 is exposed to a reducing gas such as H_2, the gas molecules react with the oxygen ions on the surfaces of SnO_2 NFs, as shown in equation below. Such reactions result in the retrieval of the trapped electrons back to the conduction band of the sensing film and lead to a decrease in resistance of SnO_2 NFs (figure 4.14a and 4.14b).

$$2H_2 + O_2^-(ads) \rightarrow 2H_2O + e^- \tag{4.6}$$
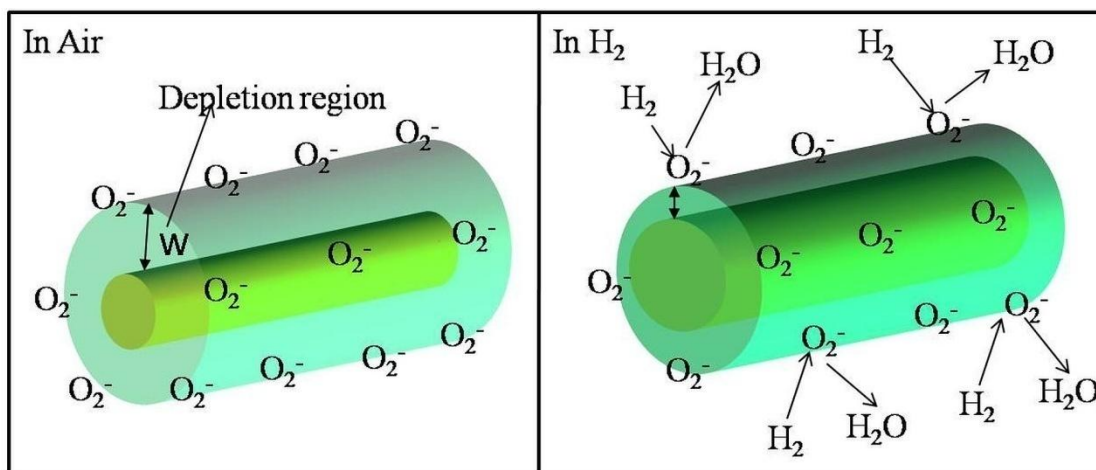
Figure 4.14: Schematic representation of H_2 sensing mechanism of SnO_2 nanorods

(iii) Thirdly, formation of heterojunction at the interface between and RGO and SnO_2 NFs. Since the work function of RGO (4.75 eV) is higher than that of SnO_2 (4.3 eV), as soon as a physical contact is formed between SnO_2 NFs and RGO, electron flows from SnO_2 NFs to

RGO in order to align the Fermi level to reach equilibrium state [215, 256, 257]. It results in the formation of depletion layer or potential barrier at the RGO-SnO$_2$ NFs interface. The width of the depletion layer changes due to interaction with H$_2$ producing noticeable change in resistance.
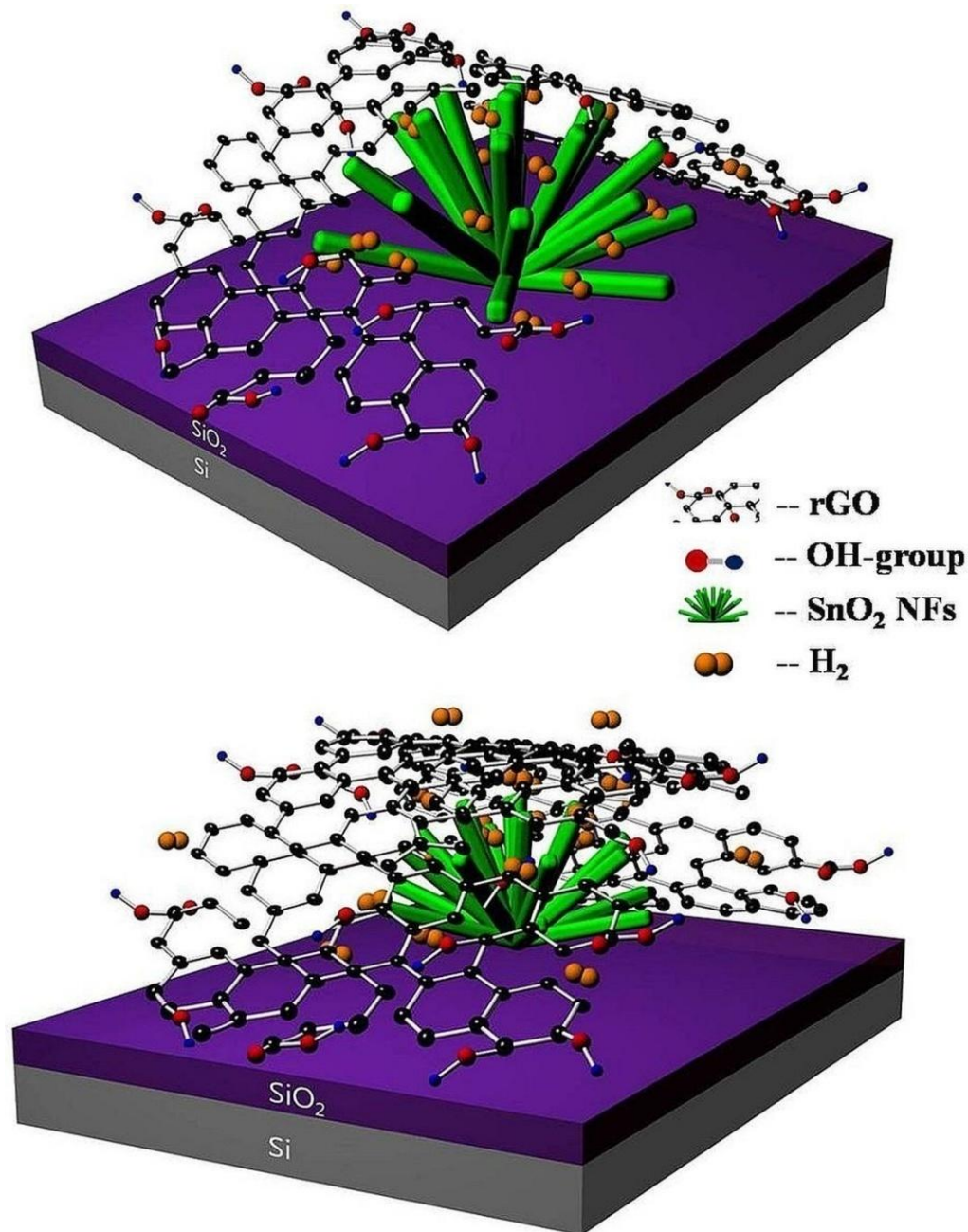
Figure 4.15: Schematic representation of incorporation of SnO$_2$ NFs into RGO layer. (a) type 1 hybrid structure and (b) type 2 hybrid structure.

By considering all these factors, the improved sensing characteristics of the RGO-SnO$_2$ NFs can be explained as follows. On injecting the H$_2$ gas, all these three types of interaction occurs simultaneously on the surface of RGO-SnO$_2$ NFs. The H$_2$ molecules directly interact with (i) RGO layer (R$_{RGO}$) (ii) and SnO$_2$ NFs (R$_{SnO2\ NFs}$) and the (iii) RGO-SnO$_2$ NFs interface (R$_{Interface}$) which results in modulation of their individual resistance contributing to the total change in resistance of the sensing layer resulting in improved sensing characteristics.

In summary, we have demonstrated low temperature H$_2$ sensor based on reduced graphene oxide (RGO) and tin oxide nanoflowers (SnO$_2$ NFs) hybrid composite film. This RGO-SnO$_2$ NFs hybrid film sensor showed an excellent response. The highly improved H$_2$ sensing characteristics of RGO-SnO$_2$ NFs hybrid are due to its (a) unique structural geometry that increased the surface area for H$_2$ adsorption, and (b) change in the width of depletion layer at the interface due to H$_2$ interaction.

<div align="center">

CHAPTER-5

MOLYBDENUM DISULFIDE NANOPARTICLES DECORATED REDUCED GRAPHENE OXIDE: HIGHLY SENSITIVE AND SELECTIVE HYDROGEN SENSOR

</div>

5.1. INTRODUCTION

Recently, transition metal dichalcogenides (TMDCs) based nanomaterials have attracted immense attention because they are found to exhibit wide range of physical and chemical properties. Most of the TMDC materials such as molybdenum disulfide (MoS_2), Tungsten selenide, Molybdenum selenide have tunable band gap, highly reactive surfaces, good optical absorption and mechanically very stable [211, 258, 259]. Of all the TMDC materials, nanostructured MoS_2 is a very promising candidate for gas sensors as it has high density of surface active sites [260-263].

The main bottleneck in using MoS_2 in sensing application is the stacking arrangement of Mo and S layer. It is a lamellar compound, consisting of three atomic layers which are held together by weak Van der waals interaction: Mo layer sandwiched between two S layers. This Van der waals interaction inevitably results in aggregation phenomenon which decreases the number of active sites as well as the whole sensing activity [264]. Therefore one needs to develop a strategy to unravel the number of active sites present in MoS_2. One method is to functionalize or hybridize this material with conductive templates or supports such as graphene or graphene oxide whose structural stability prevents the aggregation from occurring [265]. In this chapter, we have hybridized MoS_2 nanoparticles with reduced graphene oxide (RGO) to improve the sensing characteristics.

Among the graphene family, graphene oxide (GO) has been considered as an effective substrate for the decoration of nanoparticles owing to the coupling interactions between nanoparticles and oxygen-containing functional groups on the surface of GO sheets [266].

In this work, we embedded MoS_2 nanoparicles into RGO matrix producing size-controlled RGO/ MoS_2 composites for gas sensing. Here the RGO plays the dual role of support matrix for MoS_2 nanoparticles for better mechanical stability and also as a catalyst for enhancing

their gas sensing response. We have shown through this work that MoS_2 integrated with RGO have excellent response and sensitivity to H_2 at temperatures as low as 40^oC. Through this work, we intend to accelerate RGO/MoS_2 based composites in hydrogen sensing applications and provide more possibilities for reducing the hydrogen economy.

5.2. MATERIALS AND METHODS

5.2.1. Synthesis of Graphene Oxide

Graphene Oxide (GO) was synthesized by modified Hummer's method [164]. Prior to drop casting process, the concentration of as prepared GO solution was diluted to 25% by the addition of pure DI water. Then it was ultra sonicated for 45 min to reduce the size of GO flakes and then centrifuged at 15000 rpm for 5 min in order to remove the thicker flakes. The top portion of the solution was collected in a vial and stored in room temperature for the further use (figure 5.1a and 5.1b).

5.2.2. Synthesis of Molybdenum Disulphide (MoS_2) Nanoparticles

In a typical synthesis procedure, an aqueous solution of ammonium heptamolybdate tetrahydrate ((NH_4)$_6$$Mo_7O_{24}$·$4H_2O$, 2 g) and thiourea ($H_2NCSNH_2$, 1.8 g), was prepared by dissolving them in 100 ml of DI water followed by magnetic stirring for 1 hr. 3 ml of 1-Octanol and 1.4 g of sodium lauryl sulfate (SDS) was added into the above solution and was transferred to 100 ml Teflon lined autoclave. Finally, the total volume of the autoclave was adjusted to 70 % of its volume by adding DI water. Finally, the autoclave was subjected to hydrothermal reaction at 180 °C for 5 hr in oil bath. The autoclave was then gradually cooled down to room temperature and the black precipitate was separated by filtration followed by washing with copious amount of ethanol and DI water. The final product was dried in 60^0C in convection air oven for 12 hr and stored in glass vial for further use.

5.2.3. Fabrication of Gas Sensor

The electrodes for the sensors were fabricated on silicon (Si) substrate with 300 nm SiO_2 layer. Before fabrication, the silicon substrates were cleaned in acetone, ethanol and deionized water by ultrasonication followed by drying in nitrogen flow. The interdigitated electrodes were fabricated by e-beam evaporation by depositing 10 nm Ti and 100 nm Au onto a lithographically

patterned photoresist mold. The photoresist was removed by lift-off process. The resultant electrodes were washed with ethanol and copious amount of deionized water and finally dried by nitrogen flow. 1 mg of MoS_2 powder was suspended in 0.5 ml of GO solution under sonication for 1hr to produce uniform suspension, after which 3µl of MoS_2 nanoparticles dispersed GO solution was suspended on the metal electrodes followed by annealing at 400^oC (figure 5.1c and 5.1d). For comparison, the control sample was prepared by directly drop casting 3µl of 25% GO solution on SiO_2/Si substrate followed by heating at 400^oC.

Figure 5.1: Schematic representation of formation of RGO/MoS_2 composite sensing layer (a) Graphite (b) Graphene oxide (GO) preparation by modified hummer's method (c) RGO/MoS_2 composite (d) FE-SEM images of RGO/MoS_2 composite based sensing layer.

5.2.4. Hydrogen Gas Sensing Technique

The gas sensing measurements were carried out in a closed chamber equipped with PID controlled electrical heater. Before starting the sensing measurement, the chamber was evacuated to ~ 2×10^{-5} Torr by rotary pump. The sensing measurement was performed by sending high purity H_2, NO, and NH_3 gases to the gas sensing chamber. The flow rate was controlled using mass flow controllers and sensing response of the composite was monitored by measuring the change in current [267].

5.3. RESULTS AND DISCUSSIONS

Figure 5.2a shows the schematic diagram of RGO/MoS_2 based hydrogen sensor. Room temperature current-voltage (I-V) characteristics (figure 5.2b) of RGO and RGO/MoS_2 based devices exhibited linear (Ohmic) behavior with the resistance of 2.3 MΩ and 28 MΩ respectively, indicating that the contacts are ohmic in nature.

Figure 5.3a and 5.3b shows the surface morphology of pure MoS_2 and RGO/MoS_2 composite. The as prepared MoS_2 nanoparticles (size ~ 32 nm) after dispersion onto a silicon substrate instantaneously agglomerated as their surfaces have high density of active sites (figure 5.3a). Upon dispersing MoS_2 nanoparticles into RGO, they are found to be homogenously dispersed as shown in figure 3b. This clearly shows that the RGO is an ideal matrix material for MoS_2 nanoparticles to retain their surface properties.

Figure 5.2: (a) Schematic illustration of RGO/MoS_2 sensing device. (b) I-V characteristics of RGO/MoS_2 based device

Figure 5.3: FE-SEM image of as prepared (a) MoS_2 nanoparticles and (b) RGO/MoS_2 NPs composite

The atomic valence states and the composition of the MoS_2/RGO composites were characterized by X-ray photoelectron spectroscopy (XPS) and the following elements were identified: C, O, Mo, and S. In the C 1s XPS spectrum of GO, the three observable peaks correspond to C=O (288.3 eV), C-O (286.7 eV), and C-C (284.5 eV) groups respectively (figure 5.4a). For RGO/MoS_2 composite the intensities of all C 1s peaks pertaining to functional groups C=O, C-O, and C-C has decreased to a large extent (figure 5.4b). This is a confirmation of effective removal of oxygen functional groups after the annealing treatment. Figure 5.4c shows

high resolution XPS spectrum of RGO/MoS$_2$ composite in the Mo3d region. It can be deconvoluted into four peaks; the two intense peaks observed at 229.6 eV and 232.8 eV are characteristics signature of Mo 3d5/2 and Mo 3d3/2 states respectively. The peak observed at 226.8 eV corresponds to S 2s state of MoS$_2$, while the high binding energy peak observed at 236 eV can be attributed to Mo3d state of MoO$_3$ or MoO$_4^{2-}$, which may result from the oxidation of the composite sample in air. Furthermore, S 2p spectra of RGO/MoS$_2$ exhibited two main doublets located at binding energies of 162.4 eV and 164.0 eV corresponds to S 2p$_{3/2}$ and S 2p$_{1/2}$ lines of MoS$_2$ (figure 5.4d). Additionally, the binding energy at 165.6 eV suggests the existence of bridging disulfides S$_2^{2-}$ and S^{2-}. The high energy peak observed at 167.8 eV can be assigned to S^{4+} species in sulfate groups (SO$_3^{2-}$) which are usually observed at the edges of MoS$_2$ nanoparticles [265, 267].

Figure 5.4: (a) C1s XPS spectrum of GO (b) C1s spectrum of RGO/MoS$_2$ nanoparticles composite (c) Mo3d spectrum of RGO/MoS$_2$ and (d) S 2p spectra of RGO/MoS$_2$ NPs composite.

5.3.1 Gas Sensing Properties

The gas sensing response of RGO/MoS$_2$ was assessed by monitoring the resistance change upon exposure to trace concentrations (200 and 500 ppm) of H$_2$, NO and NH$_3$ at operating temperatures ranging from RT to 60°C. The sensing response was monitored with semiconductor characterization system (Keithley 4200 SCS) at different operating temperature. A voltage of 1V was applied to sensing device and response towards H$_2$ was calculated according the following equation [268, 269].

$$R(\%) = 100 \times \Delta R/R_o = 100 \times (R_{gas} - R_o)/R_o \qquad (5.1)$$

where R$_o$ is the resistance of RGO/MoS$_2$ devices before the exposure to H$_2$ gas, and R$_{gas}$ is the resistance of the device in the presence of H$_2$. Hydrogen was introduced (400 s) and removed (300 s) from the gas chamber periodically. Both introduction and removal of H$_2$ was considered as a single period (700 s). H$_2$ concentration was fixed at 200 ppm for the first period and at the end of the cycle, the concentration was increased to 500 ppm. This results in a sensing curve containing two periods in series for a particular operating temperature as shown in figure 5.5. For comparison, pure RGO, prepared by using the same experimental condition, is used as a control sample. Figure 5.5a and 5.5b shows the typical H$_2$ sensing profiles of RGO and RGO/MoS$_2$ with the concentrations of 200 and 500 ppm at different operating temperatures. For the RGO/MoS$_2$ sensor, the sensing response was very sharp with resistance increasing rapidly as H$_2$ gas is introduced. It also showed reasonably quick recovery after removing the H$_2$ gas. Considering the fact that only 200 ppm of H$_2$ gas was used, the sample seemed to possess remarkable sensitivity to H$_2$ gas. Control sample RGO showed similar characteristics but with significantly lower responsivity.

For RGO/MoS$_2$, at room temperature, the response plateaued at ~ 1.1 % for 200 ppm of H$_2$ and across all concentrations ranges. The response however significantly increased to 15.6% on heating the sample to 60°C. From the sensing response of the control sample and composite, it is quite evident that addition of MoS$_2$ nanoparticles had improved the responsivity by 81%. The response of control sample and composite seemed to vary very little with increase in H$_2$ concentration. This is due to the fact that the sensing response depends mainly on the active surface area of the sensing materials. RGO with its planar structure offers maximum exposure to

active sites for H_2 and hence exhibits good sensitivity even for lower gas concentration. In the case of composite the presence of MoS_2 nanoparticles improved the sensing response by providing more active sites for H_2 bonding.

Figure 5.5: Hydrogen Sensing response of (a) RGO and (b) RGO/MoS_2 composite at operating temperatures of RT, 40°C and 60°C for the concentration of 200 ppm – 1000 ppm.

Table 5.1 compares the H_2 sensing response of various materials reported in the literature with those of RGO/MoS_2 composite which was used in this study. It is clear that the

RGO/MoS$_2$ composite exhibits excellent H$_2$ sensing response compared to the reported samples at a given concentration and operating temperature.

Table 5.1: Comparison of H$_2$ sensing response of the RGO/MoS$_2$ nanoparticles composite prepared in this work with those reported in the literature.

Materials	Working Temperature [^{o}C]	Concentration [ppm]	Response [%]	Reference
Reduced graphene oxide	300°C	200	17	[245]
Graphene/ZnO Nanocomposite	150°C	200	3.5	[242]
Pt/Pd bimetallic ultra-thin films	150°C	10000	13.5	[248]
Ni doped TiO$_2$ Nanotubes	200°C	1000	13.8	[244]
Graphene	130°C	10000	7.6	[250]
ZnO:Cd nanorods	220°C	1000	6.13	[249]
Pd loaded SnO$_2$ nanofibres	320°C	1000	12	[246]
RGO/MoS$_2$ Nanoparticles	60°C	200	15.6	This work

The response time and recovery time of RGO/MoS$_2$ based sensor to 200 ppm of H$_2$ were 251 s and 260 s respectively which are much less than the previously reported values suggesting excellent performance of RGO/MoS$_2$ in H$_2$ gas detection.

5.3.2. Selectivity

For practical sensing applications, a sensor should be highly selective to various gases. We investigated the selectivity of RGO/MoS$_2$ sensors by exposing NO and NH$_3$ for different concentration (200 to 500 ppm) at different operating temperatures. Selectivity is quantified by taking the ratio of sensing response of H$_2$ with respect to other gases such as NO and NH$_3$ which are used in this study. The selectivity ratio or selectivity coefficient (K$_{SC}$) of H$_2$ for other gases such as NO and NH$_3$ were calculated using the following equation [273].

$$K_{SC} = \frac{S_{H_2}}{S_{NO,NH_3}} \qquad (5.2)$$

where S_{H_2}, S_{NO} and S_{NH_3} are the responses of the sensor to H$_2$, NO and NH$_3$ gases respectively.

Table 5.2: The Selectivity coefficient "K_{SC}" of the RGO/MoS$_2$ nanoparticles based H$_2$ sensor at 200 ppm in comparison to ammonia (NH$_3$) and nitric oxide (NO) gases at different operating temperature.

	K_{SC} at 200 ppm		
Operating temperature	RT	40°C	60°C
Ammonia	1.05	2.5	2.9
Nitric Oxide	1.3	2.9	3.6

Figure 5.6: Comparative sensing response of RGO/MoS$_2$ nanoparticles based composite at 60°C for 200 ppm and 500 ppm concentrations of H$_2$, NO and NH$_3$.

Table 5.2 lists the selectivity coefficient "K_{SC}" of RGO/MoS$_2$ based H$_2$ sensor for 200 ppm operated at RT, 40°C and 60°C. The selectivity coefficient "K_{SC}" for the operating temperature 60°C is the highest. The higher values of K_{SC} indicates the more selective detection of H$_2$, that is the value of K_{SC} = 3.6 for NO suggests that the H$_2$ response of RGO/MOS$_2$ is 3.6

higher than that of NO whereas K_{SC} = 2.9 for NH_3 shows that H_2 response is 2.9 times higher [270-272]. It is to be pointed out that both NH_3 and NO are highly reactive gases due to the presence of unpaired electrons which allows them to easily bond with any surface. Greater selectivity shown by the composite to H_2 can only be related to the size effect. H_2 being very small in comparison to NO and NH_3 can percolate through defects and pores and access the active sites present underneath the surface [274, 276]. This leads to higher response for H_2 in comparison to other gases. Figure 5.6 shows the comparison of selective H_2 response of RGO/MoS_2 layer compared to NO and NH_3 at different concentrations and at 60^oC.

It is also to be noted that, the addition of MoS_2 nanoparticles also improved the sensing response characteristics of RGO towards NH_3 and NO as in the case of H_2. However, the improvement was more significant for H_2 in comparison to NO and NH_3, which can be attributed to the structural characteristics of sensing layer. From the FE-SEM images, it can be clearly seen that MoS_2 nanoparticles are incorporated into RGO layer such that some nanoparticles are anchored on the top surface of RGO layer and some are underneath it. These structures play a significant role in sensing characteristics of the composite. Recently, it has been reported that graphene oxide is tortuous in nature with the presence of nanochannels in the space between each graphene oxide layers [276, 277]. The pores in the graphene oxide act as the permeation route for gases with very small size. When the sensing gases (H_2, NH_3 and NO) is exposed to RGO/MoS_2 layer the gases have the possibility of interacting with (i) RGO layer (ii) MoS_2 nanoparticles anchored on RGO and (iii) MoS_2 nanoparticles which are present underneath the RGO layer. The highly improved H_2 sensing response characteristics of RGO/MoS_2 compared to other (NH_3 and NO) gases can be attributed to interaction of H_2 gas with MoS_2 nanoparticles anchored on the top and bottom surface of RGO. The top RGO layers serves as a filtering layer which selectively permits only H_2 gas due to its smaller size to pass through and interact with MoS_2 nanoparticles buried underneath. However, for both NH_3 and NO percolation is not possible due to their larger sizes and their activity is confined to the top surface. Figure 5.7 depicts the sensing mechanism involved in RGO/MoS_2. H_2 molecule with their smaller size were able to easily permeate through the nanochannels/nanopores (red circles) and defects whereas this permeation is very limited for NH_3 and NO because of their sizes. This phenomenon can be attributed to the improved sensing response characteristics of RGO/MoS_2 for H_2 over NH_3 and NO.

Figure 5.7: Schematic representation of type III interaction of H_2 sensing in RGO/MoS$_2$ nanoparticles based composite.

5.3.3. Sensing Mechanism

The sensing mechanism (resistance change on exposure to H_2) can be explained based on the interaction between hydrogen atom and chemisorbed oxygen ions (O_2^-) on the surfaces or at the interfaces (heterojunction) of the RGO/MoS$_2$ nanocomposite. The adsorption of oxygen molecules on the surface of MoS$_2$ or RGO/MoS$_2$ interface can be given by [274],

$$O_2 + e^- \rightarrow O_2^-$$ (5.3)

Upon injection of hydrogen the net reaction can be given by,

$$2H_2 + O_2^- \rightarrow H_2O + e^-$$ (5.4)
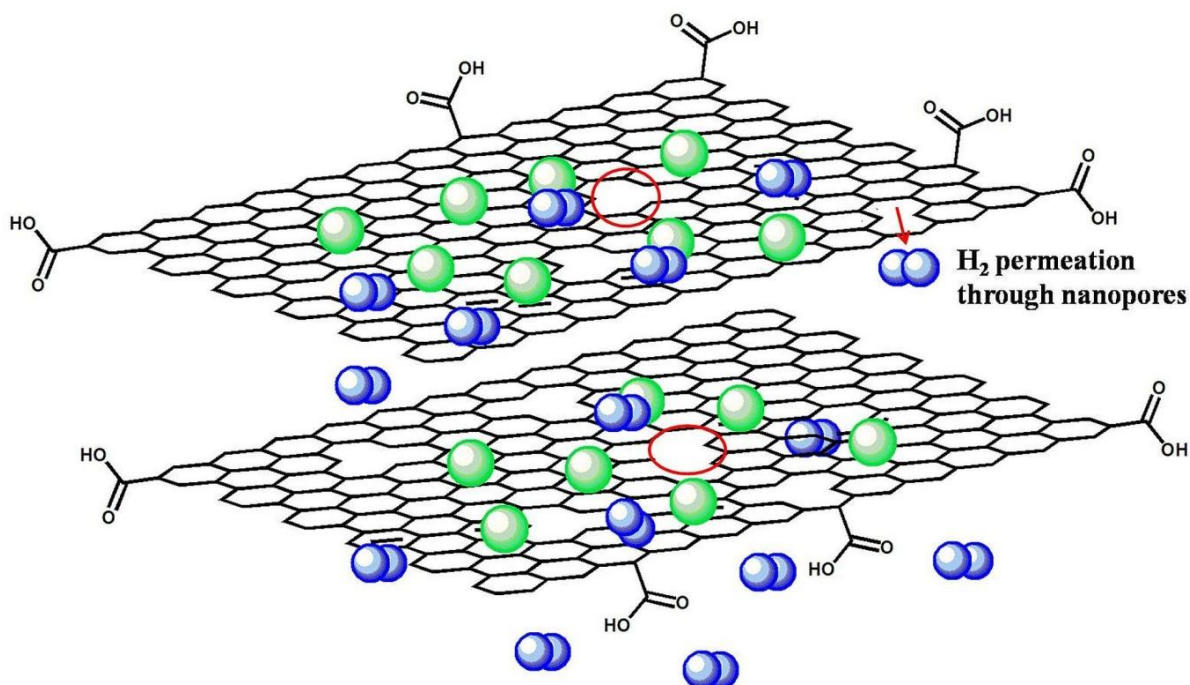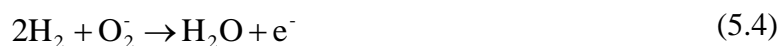
A space charge layer (SCL) is formed on the surface of MoS$_2$ nanoparticles when the electrons are trapped by the adsorbed oxygen species forming a high resistance state. When H_2 is introduced, the H_2 molecules react with the ionic oxygen species, and the electrons trapped by the oxygen adsorbents are then released back to MoS$_2$ nanoparticles, forming a low resistance

state. In addition, the Schottky barrier around the interface of RGO and MoS_2 can result in the specific capture and migration of electrons from MoS_2 nanoparticles to RGO nanosheets. Thus the role of RGO nanosheets as an electron mediator further facilitates the transfer of electrons from H_2 molecules to the RGO/MoS_2 nanostructure (figure 5.8). All the above reasons make the conductivity undergo greater changes and improve the gas sensing performance of the RGO/MoS_2 composite.
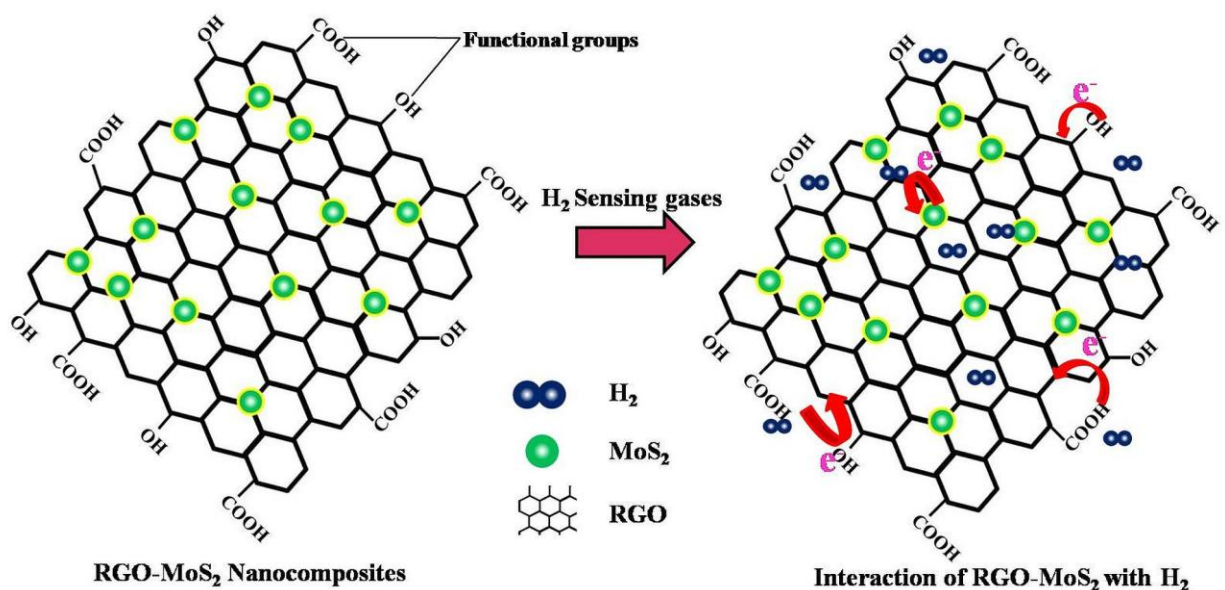
Figure 5.8: Schematic representation of H_2 sensing mechanism of RGO/MoS_2 nanoparticles based composite.

In summary, we have investigated the (H_2) sensing behavior of reduced graphene oxide (RGO)/Molybdenum disulfide (MoS_2) nano particles (NPs) based composite film fabricated by facile drop casting method. The RGO/MoS_2 composite exhibited highly enhanced H_2 response (~ 15.6 %) for 200 ppm at an operating temperature of $60^{o}C$. Furthermore, RGO/MoS_2 composite showed excellent selectivity to H_2 with respect to ammonia (NH_3) and nitric oxide (NO) which are highly reactive gas species. The composite's response to H_2 is 2.9 times higher than that of NH_3 whereas for NO it is 3.5. This highly improved H_2 sensing response and selectivity of RGO/MoS_2 at low operating temperature were attributed to the structural integration of MoS_2 nanoparticles in the nanochannels and pores in the RGO layer.

CHAPTER SIX

SUMMARY AND CONCLUSIONS

In summary, we have shown that the metal electrode performance on the ZnO NRs can be improved by using RGO as an interlayer. The RGO interlayer was realized by reducing drop casted GO on vertically aligned ZnO NRs by annealing at 60°C. Successful reduction of GO was confirmed from the ratio of I_D/I_G in the Raman spectrum. This one-step reduction process can be a suitable method for making contacts with low SB on ZnO NRs without the use of expensive polymer fillers and a high temperature annealing process. The technique is very cost effective and highly promising for the realization of reliable electrical contacts for transport measurement in ZnO NRs. Moreover, RGO integrated with ZnO NRs can find applications in sensing, field emission, energy storage and cryogenic device applications. Currently, more systematic studies are underway to study how thickness of RGO thin film affects the transport characteristics in ZnO NRs.

Highly ordered Cu_2O nanopillars were grown by AAO template assisted electrodeposition technique. AAO template etching parameters were optimized for obtaining free standing Cu_2O nanopillars. Temperature dependent electron transport properties of Au-Cu_2O-Au were analyzed by constructing a simple resistor sandwiched between two back to back schottky barriers. Thermionic field emission (TFE) theory was found to be the conduction mechanism involved in the electrical behavior. Using this model, tunneling parameter, carrier concentration and resistance of Cu_2O nanopillar were extracted. Overall, this work is a cost effective and promising approach towards the realization of vertically aligned Cu_2O nanopillars on conductive substrate which is very much in need for the solar cells and sensing applications.

The low temperature RGO-SnO_2 NFs composite based H_2 sensor fabricated by a simple drop-casting process. The surface morphology of the hybrid structure was characterized by a field emission scanning electron microscope (FE-SEM), demonstrating that incorporation of SnO_2 NFs prevents the irreversible restacking of RGO. The sensing property of the RGO-SnO_2 NFs hybrid structure was studied at different operating temperatures (RT, 40 °C, 50 °C and 60 °C) by exposing it to various concentrations of H_2 ranging from 200 ppm to 1000 ppm. The as fabricated RGO-SnO_2 NFs hybrid structure exhibited an excellent response of 19.6% to 200 ppm

of H_2 at 60 °C which is 126% improvement compared to the pure RGO. The improved response was attributed to the enhanced active surface area provided by SnO_2 NFs and the formation of a heterojunction at the RGO and SnO_2 NFs interface. Our work suggests that the RGO-SnO_2 NFs based hybrid composite can be a potential pathway to achieve a low temperature H_2 gas sensor with better sensing performance than their constituents alone. This work demonstrates that the as-prepared RGO-SnO_2 hybrid composite can be used for practical applications for monitoring H_2 at temperatures as low as 60°C. Currently, a systematic study on the effect of various concentrations of SnO_2 NFs on further improving the sensing properties of RGO thin film is being carried out.

Finally, highly sensitive and selective RGO/MoS_2 based H_2 sensor was fabricated by facile drop coating technique. The as prepared RGO/MoS_2 sensor exhibited 81% improvement in the sensing response for the concentration of 200 ppm at the operating temperature of 60°C compared to pure RGO sensor. In addition, this RGO/MoS_2 based sensor was found to be highly selective towards H_2 compared to NH_3 and NO with selective coefficient (K_{SC}) of 2.9 and 3.5. We envisage that the RGO/MoS_2 nanoparticles based composite can be a potential candidate for H_2 sensing device applications at low operating temperature.

The overall achievements of this thesis work can be summarized as follows,

- ❖ Vertically aligned free standing ZnO NRs were successfully grown on conductive ITO substrates using hydrothermal technique.
- ❖ Graphene oxide was used as a short circuit inhibitor and interfacial material to improve ohmicity of the contacts.
- ❖ The temperature (10 K - 298 K) dependent electrical transport properties of as grown ZnO NRs were carried out with the help of *in-situ* reduced graphene oxide as an interlayer for the metal contacts.
- ❖ In this work, we have shown that, unlike the conventional method, the reduction (*in-situ*) of graphene oxide on top of ZnO NRs can be carried out at temperature as low as 60°C.
- ❖ Established a standard procedure or protocol for realizing vertically aligned Cu_2O nanopillars on Au thin film.

❖ The temperature (180 K – 300 K) dependent electrical transport characteristics were carried out in two terminal configurations and were explained based on metal-semiconductor-metal (MSM) model.

❖ RGO-SnO$_2$ nanocomposite was identified as a H$_2$ gas sensor with high responsivity and selectivity at temperature as low as 60°C. The sensing response of the composite showed 126% improvement in performance in comparison to control sample (RGO). This many fold improvement was attributed to structural integration of SnO$_2$ NFs into RGO as well as the formation of heterojunction at the RGO and SnO$_2$ NFs interface.

❖ Further improvement in H$_2$ gas sensing is achieved by using RGO/MoS$_2$ nanocomposite which was prepared by simple drop casting method. The as prepared composite showed an excellent gas sensing response and selectivity towards H$_2$ compared to the pure RGO and RGO-SnO$_2$ composite. The observed improvement in the selectivity and sensing response was attributed to the presence of nanopores/nanochannels in the RGO/MoS$_2$ nanocomposites.

Our future work will be in the direction of fabrication of ZnO NRs and Cu$_2$O thin film based heterostructure based solar cells. The main focus of this work will be to study the relation between quality of heterostructure interface and photocurrent by carrying out temperature dependent electrical transport measurement with and without light illumination.

REFERENCES

[1] A.S. Edelstein (ed), *Nanomaterials:* Synthesis, Properties and Applications, *IOP publishing, Bristol*, (1999).

[2] Daniel, M.-C. and Astruc, D. 2004. Gold Nanoparticles: Assembly, Supramolecular Chemistry, Quantum-Size-Related Properties, and Applications toward Biology, Catalysis, and Nanotechnology. *Chemical Reviews,* 104**,** 293-346.

[3] J.R. Weertman, R.S. Averback, *Nanomaterials: Synthesis, Properties and Applications*, A.S. Edelstein, R.C. Cammarata (eds), *IOP publishing, London*, (1996) 323.

[4] Colvin, V. L. 2003. The potential environmental impact of engineered nanomaterials. *Nat Biotech,* 21**,** 1166-1170.

[5] Cuenot, S., Frétigny, C., Demoustier-champagne, S. and Nysten, B. 2004. Surface tension effect on the mechanical properties of nanomaterials measured by atomic force microscopy. *Physical Review B,* 69**,** 165410.

[6] Carl C. Koch (ed), Nanostructured Materials; Processing, Properties and Applications*, (2nd edn.)*, William Andrew Inc., USA, (2007).

[7] K.P. Jayadevan, T.Y. Tseng, Encyclopedia of Nanoscience and Nanotechnology*,* H.S. Nalwa (ed), American Scientific, California, 8 (2004).

[8] W. Chen, Handbook of Nanostructured Materials and Nanotechnology; Optical Properties, H.S. Nalwa (ed), Academic Press, New York, 4 (2000).

[9] R. P. Feynman. *Philosophical Transactions*. Reinhold, New York, 1961.

[10] Williams, D. B. and Carter, C. B. 1996. The Transmission Electron Microscope. Transmission Electron Microscopy: A Textbook for Materials Science. Boston, MA: Springer US.
[11] 2008. Characterization Techniques for Nanomaterials. Nanotechnology-Enabled Sensors. Boston, MA: Springer US.

[12] Binnig, G., Quate, C. F. and Gerber, C. 1986. Atomic Force Microscope. *Physical Review Letters,* 56**,** 930-933.

[13] Verma, A. and Stellacci, F. 2010. Effect of Surface Properties on Nanoparticle–Cell Interactions. *Small,* 6**,** 12-21.

[14] Khin, M. M., Nair, A. S., Babu, V. J., Murugan, R. and Ramakrishna, S. 2012. A review on nanomaterials for environmental remediation. *Energy & Environmental Science,* 5**,** 8075-8109.

[15] C. Mavroidis and A. Ferreira, Nanorobotics: Current Approaches and Technique, Springer, New York, (2013).

[16]. Jimenez-Cadena, G., Riu, J. and Rius, F. X. 2007. Gas sensors based on nanostructured materials. *Analyst,* 132**,** 1083-1099.

[17] Ting, Z., Syed, M., Nosang, V. M. and Marc, A. D. 2008. Recent progress in carbon nanotube-based gas sensors. *Nanotechnology,* 19**,** 332001.

[18] Berseth, P. A., Harter, A. G., Zidan, R., Blomqvist, A., Araújo, C. M., Scheicher, R. H., ahuja, R. and Jena, P. 2009. Carbon Nanomaterials as Catalysts for Hydrogen Uptake and Release in NaAlH$_4$. *Nano Letters,* 9**,** 1501-1505.

[19] Peralta-Videa, J. R., Zhao, L., Lopez-Moreno, M. L., De la rosa, G., Hong, J. and Gardea-Torresdey, J. L. 2011. Nanomaterials and the environment: A review for the biennium 2008–2010. *Journal of Hazardous Materials,* 186**,** 1-15.

[20] Chen, A. and Chatterjee, S. 2013. Nanomaterials based electrochemical sensors for biomedical applications. *Chemical Society Reviews,* 42**,** 5425-5438.

[21] Shan, C., Yang, H., Song, J., Han, D., ivaska, A. & Niu, L. 2009. Direct Electrochemistry of Glucose Oxidase and Biosensing for Glucose Based on Graphene. *Analytical Chemistry,* 81**,** 2378-2382.

[22] Xia, Y., Yang, P., Sun, Y., Wu, Y., Mayers, B., Gates, B., Yin, Y., Kim, F. and Yan, H. 2003. One-Dimensional Nanostructures: Synthesis, Characterization, and Applications. *Advanced Materials,* 15**,** 353-389.

[23] Lieber, C. M. 1998. One-dimensional nanostructures: Chemistry, physics & applications. *Solid State Communications,* 107**,** 607-616.

[24] Zach, M. P., Inazu, K., Ng, K. H., Hemminger, J. C. and Penner, R. M. 2002. Synthesis of Molybdenum Nanowires with Millimeter-Scale Lengths Using Electrochemical Step Edge Decoration. *Chemistry of Materials,* 14**,** 3206-3216.

[25] Park, W. I., Zheng, G., Jiang, X., Tian, B. and Lieber, C. M. 2008. Controlled Synthesis of Millimeter-Long Silicon Nanowires with Uniform Electronic Properties. *Nano Letters,* 8**,** 3004-3009.

[26] Huang, Y., Duan, X., Wei, Q. and Lieber, C. M. 2001. Directed Assembly of One-Dimensional Nanostructures into Functional Networks. *Science,* 291**,** 630-633.

[27] Iijima, S. 1991. Helical microtubules of graphitic carbon. *Nature,* 354**,** 56-58.

[28] Huang, M. H., Wu, Y., Feick, H., Tran, N., Weber, E. and Yang, P. 2001a. Catalytic Growth of Zinc Oxide Nanowires by Vapor Transport. *Advanced Materials,* 13**,** 113- 116.

[29] Wang, W., Zhan, Y. and Wang, G. 2001. One-step, solid-state reaction to the synthesis of copper oxide nanorods in the presence of a suitable surfactant. *Chemical Communications*, 727-728.

[30] Roy, P., Berger, S. and Schmuki, P. 2011. TiO2 Nanotubes: Synthesis and Applications. *Angewandte Chemie International Edition,* 50, 2904-2939.

[31] Xi, Y., Hu, C. G., Han, X. Y., Xiong, Y. F., Gao, P. X. and Liu, G. B. 2007. Hydrothermal synthesis of ZnO nanobelts and gas sensitivity property. *Solid State Communications,* 141, 506-509.

[32] And, A. L. E. and Rosen, M. 2000. The Electronic Structure of Semiconductor Nanocrystals. *Annual Review of Materials Science,* 30, 475-521.

[33] Kayanuma, Y. 1988. Quantum-size effects of interacting electrons and holes in semiconductor microcrystals with spherical shape. *Physical Review B,* 38, 9797-9805.

[34] Tsuchiya, M., Gaines, J. M., Yan, R. H., Simes, R. J., Holtz, P. O., Coldren, L. A. and Petroff, P. M. 1989. Optical Anisotropy in a Quantum-Well-Wire Array with Two-Dimensional Quantum Confinement. *Physical Review Letters,* 62, 466-469.

[35] Park, N.-M., Choi, C.-J., Seong, T.-Y. and Park, S.-J. 2001. Quantum Confinement in Amorphous Silicon Quantum Dots Embedded in Silicon Nitride. *Physical Review Letters,* 86, 1355-1357.

[36] Lu, W., Xiang, J., Timko, B. P., Wu, Y. and Lieber, C. M. 2005. One-dimensional hole gas in germanium/silicon nanowire heterostructures. *Proceedings of the National Academy of Sciences of the United States of America,* 102, 10046-10051.

[37] Zhuang, H. L., Zhang, L., Xu, H., Kent, P. R. C., Ganesh, P. and Cooper, V. R. 2016. Tunable one-dimensional electron gas carrier densities at nanostructured oxide interfaces. *Sci Rep,* 6, 25452.

[38] Wharam, D. A., Thornton, T. J., Newbury, R., Pepper, M., Ahmed, H., Frost, J. E. F., Hasko, D. G., Peacock, D. C., Ritchie, D. A. and Jones, G. A. C. 1988. One-dimensional transport and the quantisation of the ballistic resistance. *Journal of Physics C: Solid State Physics,* 21, L209.

[39] Wharam, D. A., Thornton, T. J., Newbury, R., Pepper, M., Ahmed, H., Frost, J. E. F., hasko, D. G., Peacock, D. C., Ritchie, D. A. and Jones, G. A. C. 1988. One-dimensional transport and the quantisation of the ballistic resistance. *Journal of Physics C: Solid State Physics,* 21, L209.

[40] Alivisatos, A. P. 1996. Semiconductor Clusters, Nanocrystals, and Quantum Dots. *Science,* 271, 933-937.

[41] Roduner, E. 2006. Size matters: why nanomaterials are different. *Chemical Society Reviews,* 35**,** 583-592.

[42] Fernández-García, M. and Rodriguez, J. A. 2011. Metal oxide nanoparticles. *Encyclopedia of Inorganic and Bioinorganic Chemistry*.

[43] Comini, E. 2006. Metal oxide nano-crystals for gas sensing. *Analytica Chimica Acta,* 568**,** 28-40.

[44] Bach, U., Corr, D., Lupo, D., Pichot, F. and Ryan, M. 2002. Nanomaterials-Based Electrochromics for Paper-Quality Displays. *Advanced Materials,* 14**,** 845-848.

[45] Yu, X., Marks, T. J. and Facchetti, A. 2016. Metal oxides for optoelectronic applications. *Nat Mater,* 15**,** 383-396.

[46] A.K. Srivastava (ed), Oxide Nanostructures: Growth, Microstructures, and Properties, Taylor and Francis, (2014).

[47] Huang, H., Liang, B., Liu, Z., Wang, X., Chen, D. and Shen, G. 2012. Metal oxide nanowire transistors. *Journal of Materials Chemistry,* 22**,** 13428-13445.

[48] Lee, C. J., Lee, T. J., Lyu, S. C., Zhang, Y., Ruh, H. and Lee, H. J. 2002. Field emission from well-aligned zinc oxide nanowires grown at low temperature. *Applied Physics Letters,* 81**,** 3648-3650.

[49] Dang, H. Y., Wang, J. and Fan, S. S. 2003. The synthesis of metal oxide nanowires by directly heating metal samples in appropriate oxygen atmospheres. *Nanotechnology,* 14**,** 738.

[50] Xiong, Y., LI, Z., Zhang, R., Xie, Y., Yang, J. and Wu, C. 2003. From Complex Chains to 1D Metal Oxides: A Novel Strategy to Cu_2O Nanowires. *The Journal of Physical Chemistry B,* 107**,** 3697-3702.

[51] Klingshirn, C.F., Waag, A., Hoffmann, A. and Geurts, J., 2010. *Zinc oxide: from fundamental properties towards novel applications* (Vol. 120). Springer Science & Business Media.

[52] Zhong Lin, W. 2004. Zinc oxide nanostructures: growth, properties and applications. *Journal of Physics: Condensed Matter,* 16**,** R829.

[53] Janotti, A. and Van de Walle, C.G., 2009. Fundamentals of zinc oxide as a semiconductor. *Reports on Progress in Physics*, *72* (12), p.126501.

[54] Dulub, O., Boatner, L.A. and Diebold, U., 2002. STM study of the geometric and electronic structure of ZnO (0001)-Zn, (0001)-O, (1010), and (1120) surfaces. *Surface Science*, *519*(3), pp.201-217.

[55] Meyer, B. and Marx, D., 2003. Density-functional study of the structure and stability of ZnO surfaces. *Physical Review B*, *67*(3), p.035403.

[56] Özgür, Ü., Alivov, Y.I., Liu, C., Teke, A., Reshchikov, M., Doğan, S., Avrutin, V.C.S.J., Cho, S.J. and Morkoc, H., 2005. A comprehensive review of ZnO materials and devices. *Journal of applied physics*, *98* (4), p.041301.

[57] Jagadish, C. and Pearton, S.J. eds., 2011. Zinc oxide bulk, thin films and nanostructures: processing, properties, and applications. Elsevier.

[58] Chelikowsky, J.R., 1977. An oxygen pseudopotential: Application to the electronic structure of ZnO. *Solid State Communications*, 22(6), pp.351-354.

[59] Rössler, U., 1969. Energy bands of hexagonal II-VI semiconductors. *Physical Review*, *184*(3), p.733.

[60] Vogel, D., Krüger, P. and Pollmann, J., 1995. Ab initio electronic-structure calculations for II-VI semiconductors using self-interaction-corrected pseudopotentials. *Physical Review B*, *52*(20), p.R14316.

[61] Cheng, A.J., 2008. One dimensional zinc oxide nanostructures for optoelectronic applications: solar cells and photodiodes. ProQuest.

[62] Li, Y., Tompa, G.S., Liang, S., Gorla, C., Lu, Y. and Doyle, J., 1997. Transparent and conductive Ga-doped ZnO films grown by low pressure metal organic chemical vapor deposition. *Journal of Vacuum Science & Technology A*, *15* (3), pp.1063-1068.

[63] D.W. Palmer, Available from: http://www.semiconductors.co.uk/propiivi5410.htm.

[64] Ruiz, E., Alvarez, S., Alemany, P. and Evarestov, R.A., 1997. Electronic structure and properties of Cu $_2$O. *Physical Review B*, *56* (12), p.7189.

[65] Korzhavyi, P.A. and Johansson, B., 2011. Literature review on the properties of cuprous oxide Cu_2O and the process of copper oxidation. Swedish Nuclear Fuel and Waste Management Company.

[67] Kleinman, L. and Mednick, K., 1980. Self-consistent energy bands of Cu_2O. *Physical Review B*, *21*(4), p.1549.

[68] Robertson, J., 1983. Electronic structure and x-ray near-edge core spectra of Cu$_2$ O. *Physical Review B*, *28* (6), p.3378.

[69] Biccari, F., 2012. Defects and doping in Cu_2O. Lulu. com.

[70] Wood, B.J., Wise, H. and Yolles, R.S., 1969. Selectivity and stoichiometry of copper oxide in propylene oxidation. *Journal of Catalysis*, *15* (4), pp.355-362.

[71] Olsen, L.C., Addis, F.W. and Miller, W., 1982. Experimental and theoretical studies of Cu$_2$O solar cells. *Solar cells*, *7* (3), pp.247-279.

[72] Mittiga, A., Salza, E., Sarto, F., Tucci, M. and Vasanthi, R., 2006. Heterojunction solar cell with 2% efficiency based on a Cu$_2$O substrate. *Applied Physics Letters*, *88*(16), pp.163502-163502.

[73] Dodoo-Arhin, D., 2010. Nanostructured Copper Oxides*: Production and* Applications (Doctoral dissertation, University of Trento).

[74] Elements, N.T.B. and Binary Compounds, I., 1998. Landolt-Börnstein-Group III Condensed Matter Vol. 41C, edited by O. Madelung, U. Rössler, and M. Schulz.

[75] Meyer M, Onida G, Ponchel A, Reining L. Electronic structure of stannous oxide. Computational materials science. 1998 Feb 28;10 (1):319-24.

[76] Das, S. and Jayaraman, V., 2014. SnO$_2$: A comprehensive review on structures and gas sensors. *Progress in Materials Science*, *66*, pp.112-255.

[77] Batzill, M. and Diebold, U., 2005. The surface and materials science of tin oxide. *Progress in surface science*, *79* (2), pp.47-154.

[78] Falabretti, B. and Robertson, J., 2007. Electronic structures and doping of SnO$_2$, CuAlO$_2$, and CuInO$_2$. *Journal of Applied Physics*, *102* (12), p.3703.

[79] Janotti, A., Varley, J.B., Lyons, J.L. and Van de Walle, C.G., 2012. Controlling the Conductivity in Oxide Semiconductors. In *Functional Metal Oxide Nanostructures* (pp. 23-35). Springer New York.

[80] Belliard, F., Connor, P.A. and Irvine, J.T.S., 2000. Novel tin oxide-based anodes for Li-ion batteries. *Solid State Ionics*, *135* (1), pp.163-167.

[81] Kay, A. and Grätzel, M., 2002. Dye-sensitized core-shell nanocrystals: improved efficiency of mesoporous tin oxide electrodes coated with a thin layer of an insulating oxide. *Chemistry of Materials*, *14* (7), pp.2930-2935.

[82] Furuta, S., Matsuhashi, H. and Arata, K., 2004. Catalytic action of sulfated tin oxide for etherification and esterification in comparison with sulfated zirconia. *Applied Catalysis A: General*, *269* (1), pp.187-191.

[83] Rödl, C. and Schleife, A., 2014. Photoemission spectra and effective masses of n-and p-type oxide semiconductors from first principles: ZnO, CdO, SnO$_2$, MnO, and NiO. *physica status solidi (a)*, *211*(1), pp.74-81.

[84] Lino, A.T., Borges, P.D., Scolfaro, L.M.R., Rodrigues, S.C.P. and da Silva Jr, E.F., 2007, April. Optical Properties and Carrier Effective Masses of Rutile SnO$_2$ as Obtained from Full Relativistic Ab Initio Calculations. In *PHYSICS OF SEMICONDUCTORS: 28th International Conference on the Physics of Semiconductors-ICPS 2006* (Vol. 893, No. 1, pp. 259-260). AIP Publishing.

[85] Baur, W.H., 1956. Über die verfeinerung der kristallstrukturbestimmung einiger vertreter des rutiltyps: TiO$_2$, SnO$_2$, GeO$_2$ und MgF$_2$. *Acta Crystallographica*, *9* (6), pp.515-520.

[86] Nagasawa, M., Shionoya, S. and Makishima, S., 1965. Electron Effective Mass of SnO$_2$. *Journal of the Physical Society of Japan*, *20* (6), p.1093.

[87] Ozin, G.A., Arsenault, A.C. and Cademartiri, L., 2009. *Nanochemistry: a chemical approach to nanomaterials*. Royal Society of Chemistry.

[88] Biswas, A., Bayer, I.S., Biris, A.S., Wang, T., Dervishi, E. and Faupel, F., 2012. Advances in top–down and bottom–up surface nanofabrication: Techniques, applications & future prospects. *Advances in colloid and interface science*, *170* (1), pp.2-27.

[89] Devan, R.S., Patil, R.A., Lin, J.H. and Ma, Y.R., 2012. One-Dimensional Metal-Oxide Nanostructures: Recent Developments in Synthesis, Characterization, and Applications. *Advanced Functional Materials*, *22* (16), pp.3326-3370.

[90] Li, Y., Yang, X.Y., Feng, Y., Yuan, Z.Y. and Su, B.L., 2012. One-dimensional metal oxide nanotubes, nanowires, nanoribbons, and nanorods: synthesis, characterizations, properties and applications. *Critical Reviews in Solid State and Materials Sciences*, *37* (1), pp.1-74.

[91] Liu, B. and Zeng, H.C., 2003. Hydrothermal synthesis of ZnO nanorods in the diameter regime of 50 nm. *Journal of the American Chemical Society*, *125*(15), pp.4430-4431.

[92] Yi, J.B., Pan, H., Lin, J.Y., Ding, J., Feng, Y.P., Thongmee, S., Liu, T., Gong, H. and Wang, L., 2008. Ferromagnetism in ZnO Nanowires Derived from Electro-deposition on AAO Template and Subsequent Oxidation. *Advanced Materials*, *20* (6), pp.1170-1174.

[93] Gao, T., Li, Q. and Wang, T., 2005. Sonochemical synthesis, optical properties, and electrical properties of core/shell-type ZnO nanorod/CdS nanoparticle composites. *Chemistry of materials*, *17* (4), pp.887-892.

[94] Wan, J., Chen, X., Wang, Z., Yang, X. and Qian, Y., 2005. A soft-template-assisted hydrothermal approach to single-crystal Fe$_3$O$_4$ nanorods. *Journal of Crystal Growth*, *276*(3), pp.571-576.

[95] Tang, Q., Zhou, W., Shen, J., Zhang, W., Kong, L. and Qian, Y., 2004. A template-free aqueous route to ZnO nanorod arrays with high optical property. *Chemical communications*, (6), pp.712-713.

[96] Haberkorn, N., Gutmann, J.S. and Theato, P., 2009. Template-assisted fabrication of free-standing nanorod arrays of a hole-conducting cross-linked triphenylamine derivative: toward ordered bulk-heterojunction solar cells. *Acs Nano*, *3* (6), pp.1415-1422.

[97] Satishkumar, B.C., Govindaraj, A., Nath, M. and Rao, C.N.R., 2000. Synthesis of metal oxide nanorods using carbon nanotubes as templates. *Journal of Materials Chemistry*, *10* (9), pp.2115-2119.

[98] Limmer, S.J., Seraji, S., Wu, Y., Chou, T.P., Nguyen, C. and Cao, G.Z., 2002. Template-based growth of various oxide nanorods by sol-gel electrophoresis. *Advanced Functional Materials*, *12* (1), pp.59-64.

[99] Sellmyer, D.J., Zheng, M. and Skomski, R., 2001. Magnetism of Fe, Co and Ni nanowires in self-assembled arrays. *Journal of Physics: Condensed Matter*, *13* (25), p.R433.

[100] Rhoderick, E.H. and Williams, R.H., 1988. *Metal-semiconductor contacts*(Vol. 129). Oxford: Clarendon Press.

[101] Prietsch, M., 1995. Ballistic-electron emission microscopy (BEEM): studies of metal/semiconductor interfaces with nanometer resolution. *Physics Reports*, *253* (4), pp.163-233.

[102] Clerc, R., Spinelli, A., Ghibaudo, G. and Pananakakis, G., 2002. Theory of direct tunneling current in metal–oxide–semiconductor structures. *Journal of applied physics*, *91* (3), pp.1400-1409.

[103] Caroli, C., Combescot, R., Nozieres, P. and Saint-James, D., 1971. Direct calculation of the tunneling current. *Journal of Physics C: Solid State Physics*, *4* (8), p.916.

[104] Calvet, L.E., 2001. Electrical Transport in Schottky Barrier MOSFETs(Doctoral dissertation, Yale University).

[105] Hübert, T., Boon-Brett, L., Black, G. and Banach, U., 2011. Hydrogen sensors–a review. *Sensors and Actuators B: Chemical*, *157* (2), pp.329-352.

[106] Korotcenkov, G., Han, S.D. and Stetter, J.R., 2009. Review of electrochemical hydrogen sensors. *Chemical reviews*, *109* (3), pp.1402-1433.

[107] Arafat, M.M., Dinan, B., Akbar, S.A. and Haseeb, A.S.M.A., 2012. Gas sensors based on one dimensional nanostructured metal-oxides: a review. *Sensors*, *12* (6), pp.7207-7258.

[108] Wang, C., Yin, L., Zhang, L., Xiang, D. and Gao, R., 2010. Metal oxide gas sensors: sensitivity and influencing factors. *Sensors*, *10* (3), pp.2088-2106.

[109] Liu, B., Chen, L., Liu, G., Abbas, A.N., Fathi, M. and Zhou, C., 2014. High-performance chemical sensing using schottky-contacted chemical vapor deposition grown monolayer MoS_2 transistors. *Acs Nano*, *8* (5), pp.5304-5314.

[110] Lu, G., Ocola, L.E. and Chen, J., 2009. Reduced graphene oxide for room-temperature gas sensors. *Nanotechnology*, *20* (44), p.445502.

[111] Basu, S. and Bhattacharyya, P., 2012. Recent developments on graphene and graphene oxide based solid state gas sensors. *Sensors and Actuators B: Chemical*, *173*, pp.1-21.

[112] Geim, A.K. and Novoselov, K.S., 2007. The rise of graphene. *Nature materials*, *6*(3), pp.183-191.

[113] Novoselov, K.S.A., Geim, A.K., Morozov, S., Jiang, D., Katsnelson, M., Grigorieva, I., Dubonos, S. and Firsov, A., 2005. Two-dimensional gas of massless Dirac fermions in graphene. *nature*, *438* (7065), pp.197-200.

[114] Wu, W., Liu, Z., Jauregui, L.A., Yu, Q., Pillai, R., Cao, H., Bao, J., Chen, Y.P. and Pei, S.S., 2010. Wafer-scale synthesis of graphene by chemical vapor deposition and its application in hydrogen sensing. *Sensors and Actuators B: Chemical*, *150* (1), pp.296-300.

[115] Lu, G., Ocola, L.E. and Chen, J., 2009. Reduced graphene oxide for room-temperature gas sensors. *Nanotechnology*, *20* (44), p.445502.

[116] Zhang, Z., Zou, X., Xu, L., Liao, L., Liu, W., Ho, J., Xiao, X., Jiang, C. and Li, J., 2015. Hydrogen gas sensor based on metal oxide nanoparticles decorated graphene transistor. *Nanoscale*, *7* (22), pp.10078-10084.

[117] Chung, M.G., Kim, D.H., Seo, D.K., Kim, T., Im, H.U., Lee, H.M., Yoo, J.B., Hong, S.H., Kang, T.J. and Kim, Y.H., 2012. Flexible hydrogen sensors using graphene with palladium nanoparticle decoration. *Sensors and Actuators B: Chemical*, *169*, pp.387-392.

[118] Russo, P.A., Donato, N., Leonardi, S.G., Baek, S., Conte, D.E., Neri, G. and Pinna, N., 2012. Room-Temperature Hydrogen Sensing with Heteronanostructures Based on Reduced Graphene Oxide and Tin Oxide. *Angewandte Chemie International Edition*, *51* (44), pp.11053-11057.

[119] Kalantar-zadeh, K. and Fry, B., 2008. Characterization techniques for nanomaterials. *Nanotechnology-Enabled Sensors*, pp.211-281.

[120] Watts, J.F. and Wolstenholme, J., 2003. An introduction to surface analysis by XPS and AES. An Introduction to Surface Analysis by XPS and AES, by John F. Watts, John Wolstenholme, pp. 224. *ISBN 0-470-84713-1. Wiley-VCH, May 2003.*, p.224.

[121] Whittig, L.D., Allardice, W.R. and Klute, A., 1986. X-ray diffraction techniques. *Methods of soil analysis. Part 1. Physical and mineralogical methods*, pp.331-362.

[122] Klug, H.P. and Alexander, L.E., 1954. *X-ray diffraction procedures* (Vol. 2). New York: Wiley.

[123] Goldstein, J., Newbury, D.E., Echlin, P., Joy, D.C., Romig Jr, A.D., Lyman, C.E., Fiori, C. and Lifshin, E., 2012. *Scanning electron microscopy and X-ray microanalysis: a text for biologists, materials scientists, and geologists*. Springer Science & Business Media.

[124] Binnig, G., Quate, C.F. and Gerber, C., 1986. Atomic force microscope. *Physical review letters*, *56*(9), p.930.

[125] Butt, H.J., Cappella, B. and Kappl, M., 2005. Force measurements with the atomic force microscope: Technique, interpretation and applications. *Surface science reports*, *59*(1), pp.1-152.

[126] Long, D.A., 1977. Raman spectroscopy. New York, pp.1-12.

[127] Lewis IR, Edwards H. Handbook of Raman spectroscopy: from the research laboratory to the process line. CRC Press; 2001 Aug 8.

[128] Yang, L.L., 2008. Synthesis and optical properties of ZnO nanostructures.

[129] Willander, M., Nur, O., Zhao, Q.X., Yang, L.L., Lorenz, M., Cao, B.Q., Pérez, J.Z., Czekalla, C., Zimmermann, G., Grundmann, M. and Bakin, A., 2009. Zinc oxide nanorod based photonic devices: recent progress in growth, light emitting diodes and lasers. *Nanotechnology*, *20* (33), p.332001.

[130] Özgür, Ü., Alivov, Y.I., Liu, C., Teke, A., Reshchikov, M., Doğan, S., Avrutin, V.C.S.J., Cho, S.J. and Morkoc, H., 2005. A comprehensive review of ZnO materials and devices. *Journal of applied physics*, *98* (4), p.11.

[131] Qiu, Y., Zhang, H., Hu, L., Yang, D., Wang, L., Wang, B., Ji, J., Liu, G., Liu, X., Lin, J. and Li, F., 2012. Flexible piezoelectric nanogenerators based on ZnO nanorods grown on common paper substrates. *Nanoscale*, *4* (20), pp.6568-6573.

[132] Hasan, M.R., Baek, S.H., Seong, K.S., Kim, J.H. and Park, I.K., 2015. Hierarchical ZnO nanorods on Si micropillar arrays for performance enhancement of piezoelectric nanogenerators. *ACS applied materials & interfaces*, *7* (10), pp.5768-5774.

[133] Zhan, J., Bando, Y., Hu, J. and Golberg, D., 2006. Nanofabrication on ZnO nanowires. *Applied physics letters*, *89* (24), p.243111.

[134] Altuntasoglu, O., Matsuda, Y., Ida, S. and Matsumoto, Y., 2010. Syntheses of zinc oxide and zinc hydroxide single nanosheets. *Chemistry of Materials*, *22*(10), pp.3158-3164.

[135] Briscoe, J., Gallardo, D.E. and Dunn, S., 2009. In situ antimony doping of solution-grown ZnO nanorods. *Chemical Communications*, (10), pp.1273-1275.

[136] Willander, M., Nur, O., Bano, N. and Sultana, K., 2009. Zinc oxide nanorod-based heterostructures on solid and soft substrates for white-light-emitting diode applications. *New Journal of Physics*, *11* (12), p.125020.

[137] Jain, V., Kushto, G.P., Wolak, M. and Mäkinen, A.J., 2013. Electrical contact fabrication on vertically aligned ZnO nanowires investigated by current sensing AFM. *physica status solidi (a)*, *210* (10), pp.2153-2158.

[138] Beinik, I., Kratzer, M., Wachauer, A., Wang, L., Lechner, R.T., Teichert, C., Motz, C., Anwand, W., Brauer, G., Chen, X.Y. and Hsu, X.Y., 2011. Electrical properties of ZnO nanorods studied by conductive atomic force microscopy. *Journal of Applied Physics*, *110* (5), p.052005.

[139] Hussain, I., Soomro, M.Y., Bano, N., Nur, O. and Willander, M., 2013. Systematic study of interface trap and barrier inhomogeneities using IVT characteristics of Au/ZnO nanorods Schottky diode. *Journal of Applied Physics*, *113* (23), p.234509.

[140] Lee, C.Y., Huang, J.S., Hsu, S.H., Su, W.F. and Lin, C.F., 2010. Characteristics of n-type ZnO nanorods on top of p-type poly (3-hexylthiophene) heterojunction by solution-based growth. *Thin Solid Films*, *518* (21), pp.6066-6070.

[141] Bano, N., Hussain, I., Nur, O., Willander, M., Klason, P. and Henry, A., 2009. Study of luminescent centers in ZnO nanorods catalytically grown on 4H-p-SiC. *Semiconductor Science and Technology*, *24* (12), p.125015.

[142] Klason, P., Nur, O. and Willander, M., 2008. Electrical characteristics and stability of gold and palladium Schottky contacts on ZnO nanorods. *Nanotechnology*, *19* (47), p.475202.

[143] Zou, R., He, G., Xu, K., Liu, Q., Zhang, Z. and Hu, J., 2013. ZnO nanorods on reduced graphene sheets with excellent field emission, gas sensor and photocatalytic properties. *Journal of Materials Chemistry A*, *1* (29), pp.8445-8452.

[144] Lupan, O., Pauporte, T., Chow, L., Chai, G., Viana, B., Ursaki, V.V., Monaico, E. and Tiginyanu, I.M., 2012. Comparative study of the ZnO and $Zn_{1-x}Cd_xO$ nanorod emitters hydrothermally synthesized and electrodeposited on p-GaN. *Applied Surface Science*, *259*, pp.399-405.

[145] Yu, M., Wang, A., Wang, Y., Li, C. and Shi, G., 2014. An alumina stabilized ZnO–graphene anode for lithium ion batteries via atomic layer deposition. *Nanoscale*, *6*(19), pp.11419-11424.

[146] He, Q., Wu, S., Gao, S., Cao, X., Yin, Z., Li, H., Chen, P. and Zhang, H., 2011. Transparent, flexible, all-reduced graphene oxide thin film transistors. *ACS nano*, *5* (6), pp.5038-5044.

[147] Su, Y., Kravets, V.G., Wong, S.L., Waters, J., Geim, A.K. and Nair, R.R., 2014. Impermeable barrier films and protective coatings based on reduced graphene oxide. *Nature communications*, *5*.

[148] Kamalakar, M.V., 2011. Synthesis, characterization and investigation of electrical transport in metal nanowires and nanotubes. *arXiv preprint arXiv:1110.5260*.

[149] Byrappa, K. and Yoshimura, M., 2012. *Handbook of hydrothermal technology*. William Andrew.

[150] Yoshimura, M. and Byrappa, K., 2008. Hydrothermal processing of materials: past, present and future. *Journal of Materials Science*, *43* (7), pp.2085-2103.

[151] Sze, S.M. and Ng, K.K., 2006. Metal-semiconductor contacts. *Physics of Semiconductor Devices*, pp.134-196.

[152] Greene, L.E., Law, M., Goldberger, J., Kim, F., Johnson, J.C., Zhang, Y., Saykally, R.J. and Yang, P., 2003. Low-temperature wafer-scale production of ZnO nanowire arrays. *Angewandte Chemie International Edition*, *42* (26), pp.3031-3034.

[153] Hirata, M., Gotou, T., Horiuchi, S., Fujiwara, M. and Ohba, M., 2004. Thin-film particles of graphite oxide 1:: High-yield synthesis and flexibility of the particles. *Carbon*, *42* (14), pp.2929-2937.

[154] Zhang, Y., Ma, H.L., Zhang, Q., Peng, J., Li, J., Zhai, M. and Yu, Z.Z., 2012. Facile synthesis of well-dispersed graphene by γ-ray induced reduction of graphene oxide. *Journal of Materials Chemistry*, *22* (26), pp.13064-13069.

[155] Song, N.J., Chen, C.M., Lu, C., Liu, Z., Kong, Q.Q. and Cai, R., 2014. Thermally reduced graphene oxide films as flexible lateral heat spreaders. *Journal of Materials Chemistry A*, *2* (39), pp.16563-16568.

[156] Liu, X., Pan, L., Zhao, Q., Lv, T., Zhu, G., Chen, T., Lu, T., Sun, Z. and Sun, C., 2012. UV-assisted photocatalytic synthesis of ZnO–reduced graphene oxide composites with enhanced photocatalytic activity in reduction of Cr (VI). *Chemical Engineering Journal*, *183*, pp.238-243.

[157] He, J., Niu, C., Yang, C., Wang, J. and Su, X., 2014. Reduced graphene oxide anchored with zinc oxide nanoparticles with enhanced photocatalytic activity and gas sensing properties. *RSC Advances*, *4* (104), pp.60253-60259.

[158] Yeh, T.F., Cihlář, J., Chang, C.Y., Cheng, C. and Teng, H., 2013. Roles of graphene oxide in photocatalytic water splitting. *Materials Today*, *16* (3), pp.78-84.

[159] Bandopadhyay, K. and Mitra, J., 2015. Zn interstitials and O vacancies responsible for n-type ZnO: what do the emission spectra reveal?. *Rsc Advances*, *5* (30), pp.23540-23547.

[160] Zheng, H., Weismann, A. and Berndt, R., 2014. Tuning the electron transport at single donors in zinc oxide with a scanning tunnelling microscope. *Nature communications*, *5*.

[161] Zheng, H., Kröger, J. and Berndt, R., 2012. Spectroscopy of single donors at ZnO (0001) surfaces. *Physical review letters*, *108* (7), p.076801.

[162] Look, D.C., Hemsky, J.W. and Sizelove, J.R., 1999. Residual native shallow donor in ZnO. *Physical review letters*, *82* (12), p.2552.

[164] Sze, S.M. and Ng, K.K., 2006. *Physics of semiconductor devices*. John wiley & sons.

[165] Beebe, J.M., Kim, B., Gadzuk, J.W., Frisbie, C.D. and Kushmerick, J.G., 2006. Transition from direct tunneling to field emission in metal-molecule-metal junctions. *Physical review letters*, *97* (2), p.026801.

[166] Sarker, B.K. and Khondaker, S.I., 2012. Thermionic emission and tunneling at carbon nanotube–organic semiconductor interface. *ACS nano*, *6* (6), pp.4993-4999.

[167] Ahmed, F., Choi, M.S., Liu, X. and Yoo, W.J., 2015. Carrier transport at the metal–MoS 2 interface. *Nanoscale*, *7* (20), pp.9222-9228.

[168] Reddy, N.K., Ahsanulhaq, Q., Kim, J.H. and Hahn, Y.B., 2007. Well-aligned ZnO nanorods for device applications: Synthesis and characterisation of ZnO nanorods and n-ZnO/p-Si heterojunction diodes. *EPL (Europhysics Letters)*, *81* (3), p.38001.

[169] Fang, Y., Wang, Y., Gu, L., Lu, R. and Sha, J., 2013. Effect of the defect on photoluminescence property of Al-coated ZnO nanostructures. *Optics express*, *21* (3), pp.3492-3500.

[170] Huang, X.H., Zhan, Z.Y., Pramoda, K.P., Zhang, C., Zheng, L.X. and Chua, S.J., 2012. Correlating the enhancement of UV luminescence from solution-grown ZnO nanorods with hydrogen doping. *CrystEngComm*, *14* (16), pp.5163-5165.

[171] Fang, Y.J., Sha, J., Wang, Z.L., Wan, Y.T., Xia, W.W. and Wang, Y.W., 2011. Behind the change of the photoluminescence property of metal-coated ZnO nanowire arrays. *Applied Physics Letters*, *98* (3), p.033103.

[172] Wang, W.Z., Wang, G.H., Wang, X.S., Zhan, Y.J., Liu, Y.K. and Zheng, C.L., 2002. Synthesis and characterization of Cu_2O nanowires by a novel reduction route. *Advanced Materials*, *14* (1), pp.67-69.

[173] Paracchino, A., Brauer, J.C., Moser, J.E., Thimsen, E. and Graetzel, M., 2012. Synthesis and characterization of high-photoactivity electrodeposited Cu_2O solar absorber by photoelectrochemistry and ultrafast spectroscopy. *The Journal of Physical Chemistry C*, *116* (13), pp.7341-7350.

[174] Yue, Y., Chen, M., Ju, Y. and Zhang, L., 2012. Stress-induced growth of well-aligned Cu 2 O nanowire arrays and their photovoltaic effect. *Scripta Materialia*, *66* (2), pp.81-84.

[175] Cheng, Q., Yan, W., Randeniya, L., Zhang, F. and Ostrikov, K., 2014. Plasma-produced phase-pure cuprous oxide nanowires for methane gas sensing. *Journal of Applied Physics*, *115* (12), p.124310.

[176] Chen, J., Wang, K., Hartman, L. and Zhou, W., 2008. H2S detection by vertically aligned CuO nanowire array sensors. *The Journal of Physical Chemistry C*, *112* (41), pp.16017-16021.

[177] Ma, G., Liu, S., Wang, P., Chang, J., Zhang, M. and Li, H., 2014. Synthesis of pod-like Cu_2O nanowire arrays on Cu substrate. *Materials Letters*, *120*, pp.212-215.

[178] Liu, X.M. and Zhou, Y.C., 2005. Electrochemical deposition and characterization of Cu_2O nanowires. *Applied Physics A: Materials Science & Processing*, *81* (4), pp.685-689.

[179] Choi, H. and Park, S.H., 2004. Seedless growth of free-standing copper nanowires by chemical vapor deposition. *Journal of the American Chemical Society*, *126* (20), pp.6248-6249.

[180] Lai, M. and Riley, D.J., 2008. Templated electrosynthesis of nanomaterials and porous structures. *Journal of colloid and interface science*, *323* (2), pp.203-212.

[181] Lee, S., Kim, D., Eom, H., Kim, W.B. and Yoo, B., 2014. Resistive switching characteristics of Au/P-doped NiO/Au segmented nanowires synthesized by electrochemical deposition. *Japanese Journal of Applied Physics*, *53* (2), p.024202.

[182] Chen, X., Duan, H., Zhou, Z., Liang, J. and Gnanaraj, J., 2008. Fabrication of free-standing Cu nanorod arrays on Cu disc by template-assisted electrodeposition. *Nanotechnology*, *19* (36), p.365306.

[183] Ko, E., Choi, J., Okamoto, K., Tak, Y. and Lee, J., 2006. Cu$_2$O nanowires in an alumina template: electrochemical conditions for the synthesis and photoluminescence characteristics. *ChemPhysChem*, *7* (7), pp.1505-1509.

[184] Yoo, S.H. and Park, S., 2007. Platinum-coated, nanoporous gold nanorod arrays: synthesis and characterization. *Advanced Materials*, *19*(12), pp.1612-1615.

[185] Dong, X., Huang, W. and Chen, P., 2011. In situ synthesis of reduced graphene oxide and gold nanocomposites for nanoelectronics and biosensing. *Nanoscale Res Lett*, *6* (1), p.60.

[186] Kondo, J., 1998. Cu$_2$O as a photocatalyst for overall water splitting under visible light irradiation. *Chemical Communications*, (3), pp.357-358.

[187] Zhong, J.H., Li, G.R., Wang, Z.L., Ou, Y.N. and Tong, Y.X., 2010. Facile electrochemical synthesis of hexagonal Cu$_2$O nanotube arrays and their application. *Inorganic chemistry*, *50* (3), pp.757-763.

[188] Lee, Y.I., Goo, Y.S., Chang, C.H., Lee, K.J., Myung, N.V. and Choa, Y.H., 2011. Tunable synthesis of cuprous and cupric oxide nanotubes from electrodeposited copper nanowires. *Journal of nanoscience and nanotechnology*, *11* (2), pp.1455-1458.

[189] Qin, L., Xu, J., Dong, X., Pan, Q., Cheng, Z., Xiang, Q. and Li, F., 2008. The template-free synthesis of square-shaped SnO$_2$ nanowires: the temperature effect and acetone gas sensors. *Nanotechnology*, *19* (18), p.185705.

[190] Pandey, R.K., Chandra, S. and Sahu, S.N., 1996. Handbook of semiconductor electrodeposition. M. Dekker.

[191] Shang, H. and Cao, G., 2007. Template-based synthesis of nanorod or nanowire arrays. In Springer Handbook of Nanotechnology (pp. 161-178). Springer Berlin Heidelberg.

[192] Lai, M. and Riley, D.J., 2008. Templated electrosynthesis of nanomaterials and porous structures. *Journal of colloid and interface science*, *323* (2), pp.203-212.

[193] EC08, A.A.N., 2011. Basic overview of the working principle of a potentiostat/galvanostat (PGSTAT)–Electrochemical cell setup.

[194] Bard, A.J., Faulkner, L.R., Leddy, J. and Zoski, C.G., 1980. *Electrochemical methods: fundamentals and applications* (Vol.2). New York: Wiley.

[195] Fyhn, A.M.A., 2012. Electrodeposition of Metal Oxides for Solar Cell Applications.

[196] Scholz, F., 2010. *Electroanalytical methods* (Vol. 1). Berlin-Heidelberg: Springer.

[197] Maijenburg, A.W., 2014. Templated electrodeposition of functional nanostructures: nanowires, nanotubes and nanocubes. Gildeprint drukkerijen.

[198] Kelly, R.S., 2009. Analytical Electrochemistry: The Basic Concepts. Analytical Sciences Digital Library.

[199] Andrienko, D., 2008. Cyclic Voltammetry. Cyclic Voltammetry.

[200] Ju, H., Lee, J.K., Lee, J. and Lee, J., 2012. Fast and selective Cu_2O nanorod growth into anodic alumina templates via electrodeposition. *Current Applied Physics*, *12* (1), pp.60-64.

[201] Kim, H.K., Han, S.H., Seong, T.Y. and Choi, W.K., 2000. Low-resistance Ti/Au ohmic contacts to Al-doped ZnO layers. *Applied Physics Letters*, *77*(11), pp.1647-1649.

[202] Polyakov, A.Y., Smirnov, N.B., Kozhukhova, E.A., Vdovin, V.I., Ip, K., Heo, Y.W., Norton, D.P. and Pearton, S.J., 2003. Electrical characteristics of Au and Ag Schottky contacts on n-ZnO. *Applied physics letters*, *83* (8), pp.1575-1577.

[203] Hussain, I., Soomro, M.Y., Bano, N., Nur, O. and Willander, M., 2013. Systematic study of interface trap and barrier inhomogeneities using IVT characteristics of Au/ZnO nanorods Schottky diode. *Journal of Applied Physics*, *113* (23), p.234509.

[204] Chiquito, A.J., Amorim, C.A., Berengue, O.M., Araujo, L.S., Bernardo, E.P. and Leite, E.R., 2012. Back-to-back Schottky diodes: the generalization of the diode theory in analysis and extraction of electrical parameters of nanodevices. *Journal of Physics: Condensed Matter*, *24*(22), p.225303.

[205] Zhang, Z., Yao, K., Liu, Y., Jin, C., Liang, X., Chen, Q. and Peng, L.M., 2007. Quantitative analysis of current–voltage characteristics of semiconducting nanowires: decoupling of contact effects. *Advanced functional materials*, *17* (14), pp.2478-2489.

[206] Zhang, Z.Y., Jin, C.H., Liang, X.L., Chen, Q. and Peng, L.M., 2006. Current-voltage characteristics and parameter retrieval of semiconducting nanowires. *Applied physics letters*, *88*(7), p.073102.

[207] Rui, H., Jing, Z. and Rong, Y., 2009. Synthesis and electrical characterization of tungsten oxide nanowires. *Chinese Physics B*, *18* (7), p.3024.

[208] Qi, Y., Wang, Z., Zhang, M., Wang, X., Ji, A. and Yang, F., 2014. Electron transport characteristics of silicon nanowires by metal-assisted chemical etching. *AIP Advances*, *4* (3), p.031307.

[209] Reddy, N.K., Ahsanulhaq, Q., Kim, J.H., Devika, M. and Hahn, Y.B., 2007. Selection of non-alloyed ohmic contacts for ZnO nanostructure based devices. *Nanotechnology*, *18* (44), p.445710.

[210] Scanlon, D.O., Morgan, B.J. and Watson, G.W., 2009. Modeling the polaronic nature of p-type defects in Cu_2O: The failure of GGA and GGA+ U. *The Journal of chemical physics*, *131* (12), p.124703.

[211] Hübert, T., Boon-Brett, L., Black, G. and Banach, U., 2011. Hydrogen sensors–a review. *Sensors and Actuators B: Chemical*, *157* (2), pp.329-352.

[212] Tozzini, V. and Pellegrini, V., 2013. Prospects for hydrogen storage in graphene. *Physical Chemistry Chemical Physics*, *15* (1), pp.80-89.

[213] Jena, P., 2011. Materials for hydrogen storage: past, present, and future. *J. Phys. Chem. Lett*, *2*(3), pp.206-211.

[214] Schlapbach, L. and Züttel, A., 2001. Hydrogen-storage materials for mobile applications. *Nature*, *414* (6861), pp.353-358.

[215] Abideen, Z.U., Kim, H.W. and Kim, S.S., 2015. An ultra-sensitive hydrogen gas sensor using reduced graphene oxide-loaded ZnO nanofibers. *Chemical Communications*, *51* (84), pp.15418-15421.

[216] Pak, Y., Kim, S.M., Jeong, H., Kang, C.G., Park, J.S., Song, H., Lee, R., Myoung, N., Lee, B.H., Seo, S. and Kim, J.T., 2014. Palladium-decorated hydrogen-gas sensors using periodically aligned graphene nanoribbons. *ACS applied materials & interfaces*, *6* (15), pp.13293-13298.

[217] Novoselov, K.S., Geim, A.K., Morozov, S.V., Jiang, D., Zhang, Y., Dubonos, S.V., Grigorieva, I.V. and Firsov, A.A., 2004. Electric field effect in atomically thin carbon films. *science*, *306* (5696), pp.666-669.

[218] Arsat, R., Breedon, M., Shafiei, M., Spizziri, P.G., Gilje, S., Kaner, R.B., Kalantar-zadeh, K. and Wlodarski, W., 2009. Graphene-like nano-sheets for surface acoustic wave gas sensor applications. *Chemical Physics Letters*, *467* (4), pp.344-347.

[219] Wang, J., Kwak, Y., Lee, I.Y., Maeng, S. and Kim, G.H., 2012. Highly responsive hydrogen gas sensing by partially reduced graphite oxide thin films at room temperature. *Carbon*, *50* (11), pp.4061-4067.

[220] Wang, C., Yin, L., Zhang, L., Xiang, D. and Gao, R., 2010. Metal oxide gas sensors: sensitivity and influencing factors. *Sensors*, *10*(3), pp.2088-2106.

[221] Wang, J.X., Sun, X.W., Yang, Y., Huang, H., Lee, Y.C., Tan, O.K. and Vayssieres, L., 2006. Hydrothermally grown oriented ZnO nanorod arrays for gas sensing applications. *Nanotechnology*, *17* (19), p.4995.

[222] Wu, M., Zeng, W. and Li, Y., 2013. Hydrothermal synthesis of novel SnO_2 nanoflowers and their gas-sensing properties. *Materials Letters*, *104*, pp.34-36.

[223] Kozhushner, M.A., Trakhtenberg, L.I., Landerville, A.C. and Oleynik, I.I., 2013. Theory of sensing response of nanostructured Tin-Dioxide thin films to reducing hydrogen gas. *The Journal of Physical Chemistry C*, *117* (22), pp.11562-11568.

[224] Lee, J.H., 2009. Gas sensors using hierarchical and hollow oxide nanostructures: overview. *Sensors and Actuators B: Chemical*, *140* (1), pp.319-336.

[225] Tan, E.T.H., Ho, G.W., Wong, A.S.W., Kawi, S. and Wee, A.T.S., 2008. Gas sensing properties of tin oxide nanostructures synthesized via a solid-state reaction method. *Nanotechnology*, *19* (25), p.255706.

[226] Kolmakov, A., Klenov, D.O., Lilach, Y., Stemmer, S. and Moskovits, M., 2005. Enhanced gas sensing by individual SnO_2 nanowires and nanobelts functionalized with Pd catalyst particles. *Nano Letters*, *5* (4), pp.667-673.

[227] Miller, D.R., Akbar, S.A. and Morris, P.A., 2014. Nanoscale metal oxide-based heterojunctions for gas sensing: a review. *Sensors and Actuators B: Chemical*, *204*, pp.250-272.

[228] Wang, H., Liang, Q., Wang, W., An, Y., Li, J. and Guo, L., 2011. Preparation of flower-like SnO_2 nanostructures and their applications in gas-sensing and lithium storage. *Crystal Growth & Design*, *11* (7), pp.2942-2947.

[229] Wang, J., Rathi, S., Singh, B., Lee, I., Maeng, S., Joh, H.I. and Kim, G.H., 2015. Dielectrophoretic assembly of Pt nanoparticle-reduced graphene oxide nanohybrid for highly-sensitive multiple gas sensor. *Sensors and Actuators B: Chemical*, *220*, pp.755-761.

[230] Pandey, P.A., Wilson, N.R. and Covington, J.A., 2013. Pd-doped reduced graphene oxide sensing films for H_2 detection. *Sensors and Actuators B: Chemical*, *183*, pp.478-487.

[231] Kumar, R., Varandani, D., Mehta, B.R., Singh, V.N., Wen, Z., Feng, X. and Müllen, K., 2011. Fast response and recovery of hydrogen sensing in Pd–Pt nanoparticle–graphene composite layers. *Nanotechnology*, *22* (27), p.275719.

[232] Zhang, H., Feng, J., Fei, T., Liu, S. and Zhang, T., 2014. SnO 2 nanoparticles-reduced graphene oxide nanocomposites for NO_2 sensing at low operating temperature. *Sensors and Actuators B: Chemical*, *190*, pp.472-478.

[233] Hirata, M., Gotou, T., Horiuchi, S., Fujiwara, M. and Ohba, M., 2004. Thin-film particles of graphite oxide 1:: High-yield synthesis and flexibility of the particles. *Carbon*, *42* (14), pp.2929-2937.

[234] Wang, J., Singh, B., Maeng, S., Joh, H.I. and Kim, G.H., 2013. Assembly of thermally reduced graphene oxide nanostructures by alternating current dielectrophoresis as hydrogen-gas sensors. *Applied Physics Letters*, *103*(8), p.083112.

[235] Zhang, D., Liu, A., Chang, H. and Xia, B., 2015. Room-temperature high-performance acetone gas sensor based on hydrothermal synthesized SnO_2-reduced graphene oxide hybrid composite. *RSC Advances*, *5* (4), pp.3016-3022.

[236] Chen, W. and Yan, L., 2010. Preparation of graphene by a low-temperature thermal reduction at atmosphere pressure. *Nanoscale*, *2* (4), pp.559-563.

[237] Mao, S., Cui, S., Lu, G., Yu, K., Wen, Z. and Chen, J., 2012. Tuning gas-sensing properties of reduced graphene oxide using tin oxide nanocrystals. *Journal of Materials Chemistry*, *22* (22), pp.11009-11013.

[238] Yin, L., Chen, D., Cui, X., Ge, L., Yang, J., Yu, L., Zhang, B., Zhang, R. and Shao, G., 2014. Normal-pressure microwave rapid synthesis of hierarchical SnO_2@ rGO nanostructures with superhigh surface areas as high-quality gas-sensing and electrochemical active materials. *Nanoscale*, *6* (22), pp.13690-13700.

[239] Zhang, L.S., Wang, W.D., Liang, X.Q., Chu, W.S., Song, W.G., Wang, W. and Wu, Z.Y., 2011. Characterization of partially reduced graphene oxide as room temperature sensor for H 2. *Nanoscale*, *3* (6), pp.2458-2460.

[240] Zhang, D.F., Sun, L.D., Yin, J.L. and Yan, C.H., 2003. Low-Temperature Fabrication of Highly Crystalline SnO_2 Nanorods. *Advanced Materials*, *15* (12), pp.1022-1025.

[241] Russo, P.A., Donato, N., Leonardi, S.G., Baek, S., Conte, D.E., Neri, G. and Pinna, N., 2012. Room-Temperature Hydrogen Sensing with Heteronanostructures Based on Reduced Graphene Oxide and Tin Oxide. *Angewandte Chemie International Edition*, *51* (44), pp.11053-11057.

[242] Anand, K., Singh, O., Singh, M.P., Kaur, J. and Singh, R.C., 2014. Hydrogen sensor based on graphene/ZnO nanocomposite. *Sensors and Actuators B: Chemical*, *195*, pp.409-415.

[243] Boudiba, A., Roussel, P., Zhang, C., Olivier, M.G., Snyders, R. and Debliquy, M., 2013. Sensing mechanism of hydrogen sensors based on palladium-loaded tungsten oxide (Pd–WO 3). *Sensors and Actuators B: Chemical*, *187*, pp.84-93.

[244] Li, Z., Ding, D., Liu, Q. and Ning, C., 2013. Hydrogen sensing with Ni-doped TiO2 nanotubes. *Sensors*, *13* (7), pp.8393-8402.

[245] Wang, J., Singh, B., Maeng, S., Joh, H.I. and Kim, G.H., 2013. Assembly of thermally reduced graphene oxide nanostructures by alternating current dielectrophoresis as hydrogen-gas sensors. *Applied Physics Letters*, *103* (8), p.083112.

[246] Wang, Z., Li, Z., Jiang, T., Xu, X. and Wang, C., 2013. Ultrasensitive hydrogen sensor based on Pd0-loaded SnO_2 electrospun nanofibers at room temperature. *ACS applied materials & interfaces*, *5*(6), pp.2013-2021.

[247] Rane, S., Arbuj, S., Rane, S. and Gosavi, S., 2015. Hydrogen sensing characteristics of Pt–SnO_2 nano-structured composite thin films. *Journal of Materials Science: Materials in Electronics*, *26*(6), pp.3707-3716.

[248] Hassan, K., Uddin, A.I. and Chung, G.S., 2016. Fast-response hydrogen sensors based on discrete Pt/Pd bimetallic ultra-thin films. *Sensors and Actuators B: Chemical*, *234*, pp.435-445.

[249] Yang, X., Wang, W., Xiong, J., Chen, L. and Ma, Y., 2015. ZnO: Cd nanorods hydrogen sensor with low operating temperature. *International Journal of Hydrogen Energy*, *40*(36), pp.12604-12609.

[250] Dutta, D., Hazra, A., Hazra, S.K., Das, J., Bhattacharyya, S., Sarkar, C.K. and Basu, S., 2015. Performance of a CVD grown graphene-based planar device for a hydrogen gas sensor. *Measurement Science and Technology*, *26*(11), p.115104.

[251] Illyaskutty, N., Kohler, H., Trautmann, T., Schwotzer, M. and Pillai, V.M., 2013. Hydrogen and ethanol sensing properties of molybdenum oxide nanorods based thin films: Effect of electrode metallization and humid ambience. *Sensors and Actuators B: Chemical*, *187*, pp.611-621.

[252] Chapelle, A., Yaacob, M.H., Pasquet, I., Presmanes, L., Barnabé, A., Tailhades, P., Du Plessis, J. and Kalantar-Zadeh, K., 2011. Structural and gas-sensing properties of CuO–Cu x Fe 3− x O 4 nanostructured thin films. *Sensors and Actuators B: Chemical*, *153*(1), pp.117-124.

[253] Shafiei, M., Yu, J., Chen, G., Lai, P.T., Motta, N., Wlodarski, W. and Kalantar-Zadeh, K., 2013. Improving the hydrogen gas sensing performance of Pt/MoO 3 nanoplatelets using a nano thick layer of La_2O_3. *Sensors and Actuators B: Chemical*, *187*, pp.267-273.

[254] Hung, S.T., Chang, C.J., Hsu, C.H., Chu, B.H., Lo, C.F., Hsu, C.C., Pearton, S.J., Holzworth, M.R., Whiting, P.G., Rudawski, N.G. and Jones, K.S., 2012. SnO_2 functionalized AlGaN/GaN high electron mobility transistor for hydrogen sensing applications. *international journal of hydrogen energy*, *37*(18), pp.13783-13788.

[255] Boudiba, A., Zhang, C., Umek, P., Bittencourt, C., Snyders, R., Olivier, M.G. and Debliquy, M., 2013. Sensitive and rapid hydrogen sensors based on Pd–WO_3 thick films with different morphologies. *international journal of hydrogen energy*, *38*(5), pp.2565-2577.

[256] Luo, S., Chu, P.K., Di, Z., Zhang, M., Liu, W., Lin, C., Fan, J. and Wu, X., 2006. Vacuum electron field emission from SnO_2 nanowhiskers annealed in N_2 and O_2 atmospheres. *Applied physics letters*, 88(1), p.013109.

[257] Mishra, R.K., Upadhyay, S.B., Kushwaha, A., Kim, T.H., Murali, G., Verma, R., Srivastava, M., Singh, J., Sahay, P.P. and Lee, S.H., 2015. SnO_2 quantum dots decorated on RGO: a superior sensitive, selective and reproducible performance for a H_2 and LPG sensor. *Nanoscale*, *7*(28), pp.11971-11979.

[258] Hu, Y., Lei, J., Wang, Z., Yang, S., Luo, X., Zhang, G., Chen, W. and Gu, H., 2016. Rapid response hydrogen sensor based on nanoporous Pd thin films. *International Journal of Hydrogen Energy*, *41*(25), pp.10986-10990.

[259] Hassan, J.J., Mahdi, M.A., Chin, C.W., Abu-Hassan, H. and Hassan, Z., 2013. A high-sensitivity room-temperature hydrogen gas sensor based on oblique and vertical ZnO nanorod arrays. *Sensors and Actuators B: Chemical*, *176*, pp.360-367.

[260] Sippel-Oakley, J., Wang, H.T., Kang, B.S., Wu, Z., Ren, F., Rinzler, A.G. and Pearton, S.J., 2005. Carbon nanotube films for room temperature hydrogen sensing. *Nanotechnology*, *16*(10), p.2218.

[261] Russo, P.A., Donato, N., Leonardi, S.G., Baek, S., Conte, D.E., Neri, G. and Pinna, N., 2012. Room-Temperature Hydrogen Sensing with Heteronanostructures Based on Reduced Graphene Oxide and Tin Oxide. *Angewandte Chemie International Edition*, *51*(44), pp.11053-11057.

[262] Li, H., Yin, Z., He, Q., Li, H., Huang, X., Lu, G., Fam, D.W.H., Tok, A.I.Y., Zhang, Q. and Zhang, H., 2012. Fabrication of single-and multilayer MoS_2 film-based field-effect transistors for sensing NO at room temperature. *small*, *8*(1), pp.63-67.

[263] Kannan, P.K., Late, D.J., Morgan, H. and Rout, C.S., 2015. Recent developments in 2D layered inorganic nanomaterials for sensing. *Nanoscale*, *7*(32), pp.13293-13312.

[264] Li, F., Zhang, L., Li, J., Lin, X., Li, X., Fang, Y., Huang, J., Li, W., Tian, M., Jin, J. and Li, R., 2015. Synthesis of Cu–MoS_2/rGO hybrid as non-noble metal electrocatalysts for the hydrogen evolution reaction. *Journal of Power Sources*, *292*, pp.15-22.

[265] Zheng, X., Xu, J., Yan, K., Wang, H., Wang, Z. and Yang, S., 2014. Space-confined growth of MoS_2 nanosheets within graphite: the layered hybrid of MoS_2 and graphene as an active catalyst for hydrogen evolution reaction. *Chemistry of Materials*, *26*(7), pp.2344-2353.

[266] Novoselov, K.S., Geim, A.K., Morozov, S.V., Jiang, D., Zhang, Y., Dubonos, S.V., Grigorieva, I.V. and Firsov, A.A., 2004. Electric field effect in atomically thin carbon films. *Science*, *306*(5696), pp.666-669.

[267] Liu Y, Zhao Y, Jiao L, Chen J. A graphene-like MoS_2/graphene nanocomposite as a highperformance anode for lithium ion batteries. *Journal of Materials Chemistry A*. 2014;2(32):13109-15.

[268] Hu, N., Yang, Z., Wang, Y., Zhang, L., Wang, Y., Huang, X., Wei, H., Wei, L. and Zhang, Y., 2013. Ultrafast and sensitive room temperature NH3 gas sensors based on chemically reduced graphene oxide. *Nanotechnology*, *25*(2), p.025502.

[269] Anand, K., Singh, O., Singh, M.P., Kaur, J. and Singh, R.C., 2014. Hydrogen sensor based on graphene/ZnO nanocomposite. *Sensors and Actuators B: Chemical*, *195*, pp.409-415.

[270] Samerjai, T., Tamaekong, N., Liewhiran, C., Wisitsoraat, A., Tuantranont, A. and Phanichphant, S., 2011. Selectivity towards H 2 gas by flame-made Pt-loaded WO_3 sensing films. *Sensors and Actuators B: Chemical*, *157*(1), pp.290-297.

[271] Zou, Y., Wang, Q., Xiang, C., Tang, C., Chu, H., Qiu, S., Yan, E., Xu, F. and Sun, L., 2016. Doping composite of polyaniline and reduced graphene oxide with palladium nanoparticles for room-temperature hydrogen-gas sensing. *International Journal of Hydrogen Energy*, *41*(11), pp.5396-5404.

[272] Siemons, M. and Simon, U., 2007. Gas sensing properties of volume-doped $CoTiO_3$ synthesized via polyol method. *Sensors and Actuators B: Chemical*, *126*(2), pp.595-603.

[273] Miremadi, B.K., Singh, R.C., Morrison, S.R. and Colbow, K., 1996. A highly sensitive and selective hydrogen gas sensor from thick oriented films of MoS_2. *Applied Physics A: Materials Science & Processing*, *63*(3), pp.271-275.

[274] Kanezashi, M., Yamamoto, A., Yoshioka, T. and Tsuru, T., 2010. Characteristics of ammonia permeation through porous silica membranes. *AIChE journal*, *56*(5), pp.1204-1212.

[275] Kammeyer, C.W. and Whitman, D.R., 1972. Quantum mechanical calculation of molecular radii. I. Hydrides of elements of periodic groups IV through VII. *The Journal of Chemical Physics*, *56*(9), pp.4419-4421.

[276] You, Y., Sahajwalla, V., Yoshimura, M. and Joshi, R.K., 2016. Graphene and graphene oxide for desalination. *Nanoscale*, *8*(1), pp.117-119.

[277] Amadei, C.A. and Vecitis, C.D., 2016. How to Increase the Signal-to-Noise Ratio of Graphene Oxide Membrane Research.

PUBLICATIONS

[1]. **Venkatesan, A.,** Rathi, S., Lee, I.Y., Park, J., Lim, D., Kim, G.H. and Kannan, E.S. Molybdenum disulfide nanoparticles decorated reduced graphene oxide: Highly sensitive and selective hydrogen sensor. *Nanotechnology 28 (2017) 365501*.

[2]. **Venkatesan, A.,** and Kannan, E.S. Highly ordered copper oxide (Cu_2O) nanopillar arrays using Template assisted electrodeposition technique and their temperature dependent electrical characteristics. *Current Applied Physics17 (2017) 806-812.*

[3]. **Venkatesan, A.,** Rathi, S., Lee, I.Y., Park, J., Lim, D., Kim, G.H. and Kannan, E.S., 2016. Low temperature hydrogen sensing using reduced graphene oxide and tin oxide nanoflowers based hybrid structure. *Semiconductor Science and Technology, 31(2016) 25014.*

[4]. **Venkatesan, A.,** Ramesha, C.K. and Kannan, E.S., 2016. In situ reduced graphene oxide interlayer for improving electrode performance in ZnO nanorods. *Journal of Physics D: Applied Physics, 49 (2016) 245301*.

[5]. **Venkatesan, A.,** Patel, R.N. and Kannan, E.S., 2015. Reduced Graphene Oxide for Room Temperature Hydrogen Storage Application. In *Advanced Materials Research (Vol. 1086, pp. 91-95). Trans Tech Publications*.

CONFERENCE/WORKSHOP ATTENDED

[1]. Anuroshini Ramakrishan, **Venkatesan** and E. S. Kannan "Fabrication of p-n junction using ZnO Nanopillars and Cu_2O thin films" in International Conference of Young Researchers on Advanced Materials (IUMRS –ICYRAM 2016), in Indian Institute of Science, Bangalore, India on 08-15 September 2016.

[2]. **A. Venkatesan and** E. S. Kannan "Optimization of Template Removal Technique for Improving the Yield of Vertically Aligned Copper Oxide Nanorods" in Second International Conference on Materials Science and Technology (ICMST-2016), in St. Thomas College, Pala, Kerala on 05-08 June 2016.

[3]. **Venkatesan**, R. Aswini, and E. S. Kannan 'Synthesis and Characterization of One (1-D) Dimensional Tin Oxide Nanorods for Gas Sensing Applications' in Indo-UK International Workshop on Advanced Materials And Their Applications in Nanotechnology (AMAN-2014), BITS Pilani University, Goa on 17th – 19th May, 2014.

[4]. **Venkatesan**, R. Aswini, and E. S. Kannan 'Controlled growth of one-dimensional (1-D) Zinc Oxide (ZnO) Nanorod Arrays by facile Hydrothermal Technique' in National Conference on Nanotechnology and Renewable Energy (NCNRE-2014), Jamia Millia Islamia university, New Delhi on 28th – 29th April, 2014.

[5]. **Venkatesan**, Raj Nanalal Patel, and E. S. Kannan 'Reduced Graphene for room temperature hydrogen storage application' in International Conference on Materials for Energy and Nano Convergence (ICMENC-2013), Hindustan University, Chennai on 4th-6th July, 2013.

[6]. INUP Hands – on Training on 'Nanofabrication Technologies' organized by Centre for Nano Science and Engineering, IISc Bangalore, Bangalore, on 18th-28th June 2013.

[7]. INUP Familiarization Workshop on Nanofabrication Technologies organized by Centre for Nano Science and Engineering, IISC Bangalore, Bangalore, on 16-18 April, 2012.

[8]. International Workshop on Advanced Functional Nanomaterials Organized by Centre for Nanoscience and Technology, Crystal Growth Centre and International Affairs, Anna University, Chennai, on 21st - 24th February, 2011.

[9]. NANOMEET 2011, National Level Technical Meet on Nanoscience and Technology organized by Anna University, Chennai, on 7th – 8th January, 2011.

[10].National Workshop on Solar Energy Materials and Devices, Organized by KIIT University, Bubaneshwar, on 24th – 25th January, 2009.

BIODATA OF CANDIATE

A. VENKATESAN was born on 6th June 1987 at Chennai in India. He received his Bachelor of Science in Physics from Gurunanak College, Chennai in 2007. He obtained his M.Sc in Physics from University of Madras in 2009. Then he joined as a lecturer in Physics in Apollo Polytechnic College, Chennai, India and worked for one year (May 2009 – May 2010). He obtained his M.Phil in Physics in 2011 from University of Madras, Chennai, India. In August 2011, he started his graduate study in Birla Institute of Technology and Science, Pilani – K K Birla Goa Campus with the proposed thesis "Transport and Gas Sensing Properties of One Dimensional Metal Oxide Nanostructures and their Composites".

He received the BITS Pilani PhD research fellowship for five years. He also received a travel and accommodation support from Dr. E. S. Kannan's professional development fund (PDF) to carry out the research work at Sungkyunkwan University in South Korea.

BIODATA OF SUPERVISOR

Dr. E.S. Kannan is currently working as an Assistant Professor at the Department of Physics in BITS Pilani, K K Birla Goa campus. He received his M.Sc in Physics from the Bharathiar University, Coimbatore, India in 2003. He completed his doctorate in experimental condensed matter physics in 2009 from Sungkyunkwan Advanced Institute of Nanotechnology. For his doctoral thesis he studied the transport characteristics of GaAs/AlGaAs heterostructures embedded with InAs quantum dots and investigated the possible application of the heterostructure to develop variable mobility transistors and high density quantum dot based memory devices. Following his Ph.D work, he joined Industrial Electronic Application Center at Sungkyunkwan University, South Korea and investigated electrical and optical properties of nanostructures for single electron and photon based mobile device applications. In 2010, he was awarded CNRS postdoctoral fellowship at Grenoble High Magnetic Field Laboratory to develop Si/SiGe heterostructure based microwave and terahertz detectors and current generators. He joined the Department of Physics at BITS Pilani, K K Birla Goa Campus as a faculty member in the year 2012. His research interests includes 1D metal oxide nanostructures, transport characteristics, Low temperature physics, Gas sensors, Transport Phenomenon in GaAs/AlGaAs and Si/SiGe heterostructures, Graphene and graphene oxide based organic devices, Quantum dot memory devices, Microwave and Terahertz detectors and Single Electron Transistors.

GLOSSARY

A

Anodic Aluminum Oxide or AAO Template

AAO Template is a self organized material with honeycomb like structure formed by high density arrays of uniform and parallel nanopores.

Ag/AgCl

Ag/AgCl is a type of reference electrode commonly used in electrodeposition or electrochemical measurements.

B

Band gap

In solids (semiconductor), the band gap is referred as the energy difference between the top of the valence band and bottom of the conduction band.

C

Current

An electric current is a flow of electric charge.

It is defined as flow of charge carriers (electron or hole) in semiconductors.

In an electrolyte the current is carried by charged species or ions

Chronoamperometry

Chronoamperometry is an electrochemical technique in which the potential of the working electrode is stepped and the resulting current from faradic process at the electrode (working) is monitored as function of time.

Cryostat

A cryostat is a device used to maintain low cryogenic temperatures of sample.

D

Density of States

In solid state physics the density of states of a system is defined as the number of states per interval of energy at each energy level that are available to be occupied.

E

Electrodeposition

A process that exploits the formation of solid materials from electrochemical reaction in plating solution on the substrates

e-beam evaporation/evaporator

It is a physical vapor deposition in which target anode is bombarded with an electron beam produced by charged tungsten filament under high vacuum. The equipment which is being used for evaporation is called as e-beam evaporator.

F

Farayday's Second Law

Faradays second law of electrolysis states that, when electricity is passed through electrolytes, the mass of the substance deposited are proportional to their chemical equivalent weight.

L

Low temperature electrical transport measurement

Current-Voltage measurement of the sample at cryostat temperature.

R

Resistance

The electrical resistance of an electrical conductor is a measure of the difficulty to pass an electric current through a conductor. The resistance is defined as

$$R = V/I$$

S

Selectivity

Selectivity is the ability of the sensor to respond to a particular gas in the presence of other gases.